MICROCOPY RESOLUTION TEST CHART
NATIONAL BUREAU OF STANDARDS 1963-A

④

AFAL-TR-87-059

AD-A194 160

Solar Rocket Plume/Mirror Interactions

Authors:
C. L. Merkle
S-T Yu

Pennsylvania State University
Mechanical Engineering Department
University Park, PA 16802

F04611-84-C-0028

DTIC
ELECTE
S APR 0 8 1988
H
D

Prepared for the: **Air Force
Astronautics
Laboratory**

Air Force Space Technology Center
Space Division, Air Force Systems Command
Edwards Air Force Base,
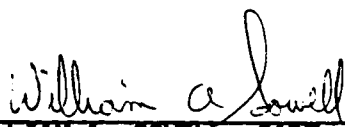California 93523-5000

88 4 8 028

NOTICE

When U.S. Government drawings, specifications, or other data are used for any purpose other than a definitely related Government procurement operation, the fact that the Government may have formulated, furnished, or in any way supplied the said drawings, specifications, or other data, is not to be regarded by implication or otherwise, or in any way licensing the holder or any other person or corporation, or conveying any rights or permission to manufacture, use, or sell any patented invention that may be related thereto.

FOREWORD

This final report documents the Pennsylvania State University solar rocket plume/mirror interaction study for the Air Force Astronautics Laboratory (AFAL), Edwards Air Force Base, CA. The project was performed under contract F04611-84-C-0028. AFAL Project Manager was Jerry Naujokas, succeeded by Chuck Ford.

This report has been reviewed and is approved for release and distribution in accordance with the distribution statement on the cover and on the DD Form 1473.

CHARLES R. FORD
Project Manager

WILLIAM A. SOWELL, CAPT, USAF
Chief, Advanced Propulsion Branch

FOR THE COMMANDER

ROBERT L. GEISLER
Deputy Chief, Astronautical Sciences
    Division

REPORT DOCUMENTATION PAGE

1a. REPORT SECURITY CLASSIFICATION	1b. RESTRICTIVE MARKINGS
Unclassified	

2a. SECURITY CLASSIFICATION AUTHORITY	3. DISTRIBUTION/AVAILABILITY OF REPORT
2b. DECLASSIFICATION/DOWNGRADING SCHEDULE	Approved for public release; distribution is unlimited.

4. PERFORMING ORGANIZATION REPORT NUMBER(S)	5. MONITORING ORGANIZATION REPORT NUMBER(S)
	AFAL-TR-87-059

6a. NAME OF PERFORMING ORGANIZATION	6b. OFFICE SYMBOL (If applicable)	7a. NAME OF MONITORING ORGANIZATION
Pennsylvania State University		Air Force Astronautics Laboratory

6c. ADDRESS (City, State and ZIP Code)	7b. ADDRESS (City, State and ZIP Code)
Mechanical Engineering Department University Park, PA 16802	AFAL/LKCS Edwards AFB, CA 93523-5000

8a. NAME OF FUNDING/SPONSORING ORGANIZATION	8b. OFFICE SYMBOL (If applicable)	9. PROCUREMENT INSTRUMENT IDENTIFICATION NUMBER
		F04611-84-C-0028

8c. ADDRESS (City, State and ZIP Code)	10. SOURCE OF FUNDING NOS.			
	PROGRAM ELEMENT NO.	PROJECT NO.	TASK NO.	WORK UNIT NO.
11. TITLE (Include Security Classification) Solar Rocket Plume/Mirror Interactions (U)	62302F	5730N	00	BR

12. PERSONAL AUTHOR(S)
Merkle, Charles L. and Yu, Sheng-Tao

13a. TYPE OF REPORT	13b. TIME COVERED	14. DATE OF REPORT (Yr., Mo., Day)	15. PAGE COUNT
Final	FROM 85/1/9 TO 87/1/3	88/2	152

16. SUPPLEMENTARY NOTATION

17. COSATI CODES			18. SUBJECT TERMS (Continue on reverse if necessary and identify by block number)
FIELD	GROUP	SUB. GR.	Solar Rocket Propulsion, Plume/Mirror Interactions, Thermal Propulsion Systm
21	09	1	

19. ABSTRACT (Continue on reverse if necessary and identify by block number)

The extent to which the plume from a solar thermal rocket will impinge on the solar collector is studied by flowfield analysis. Such interaction can adversely affect collector performance through fouling, excessive heat loading, or pressure loads that deform the delicate structures. The geometrical shape of the collector is such that only the flow from the nozzle boundary layer can reach it, but the thrust levels of interest lead to very viscous nozzle flows with large, thick boundary layers. Calculations based on continuum theory appear adequate for determining the fraction of the plume that hits the collector, but transitional and rarefied effects are needed to ascertain the details of the distribution along the surface. Results show that both pressure and heat transfer effects are low, but that they increase as the chamber pressure or the thrust size is reduced. Keywords:

20. DISTRIBUTION/AVAILABILITY OF ABSTRACT	21. ABSTRACT SECURITY CLASSIFICATION
UNCLASSIFIED/UNLIMITED ☐ SAME AS RPT. ☒ DTIC USERS ☐	Unclassified

22a. NAME OF RESPONSIBLE INDIVIDUAL	22b. TELEPHONE NUMBER (Include Area Code)	22c. OFFICE SYMBOL
Charles R. Ford	(805) 275-5127	LKCS

DD FORM 1473, 83 APR EDITION OF 1 JAN 73 IS OBSOLETE.

TABLE OF CONTENTS

iii

TABLE OF CONTENTS (Continued)

LIST OF TABLES

LIST OF FIGURES

LIST OF FIGURES (Continued)

INTRODUCTION

THE SOLAR THERMAL PROPULSION CONCEPT

The recent resurgence of interest in space has led to a dramatic increase in the number and types of interorbital transfer missions being contemplated. The propulsive requirements for these missions include a broad spectrum of performance capabilities ranging from the high thrust, low I_{sp} characteristics that are representative of conventional chemical propulsion systems to the high thrust, high I_{sp}'s that characterize electric propulsion. The need for systems that provide intermediate levels of thrust and I_{sp}, however, appears to be particularly strong. A number of alternative concepts whose performance matches this intermediate range have been proposed, including resistojets, thermal arcjets, pulsed electrothermal thrusters, microwave heated devices, laser thermal concepts and solar thermal rockets. The expected relative performance of several of these cycles is compared in Fig. 1. Recent studies[1,2] have indicated that solar thermal propulsion based upon indirect absorption of radiation promises to provide near-term propulsive performance that could effectively fill this intermediate thrust-I_{sp} gap and it is to this topic that the present report is directed.

The concept of solar thermal propulsion is based upon heating a working fluid by concentrated solar energy and expanding it through a standard propulsive nozzle to produce thrust. A primary advantage of solar propulsion is that the energy supply need not be accelerated with the vehicle, but remains remote from the

1
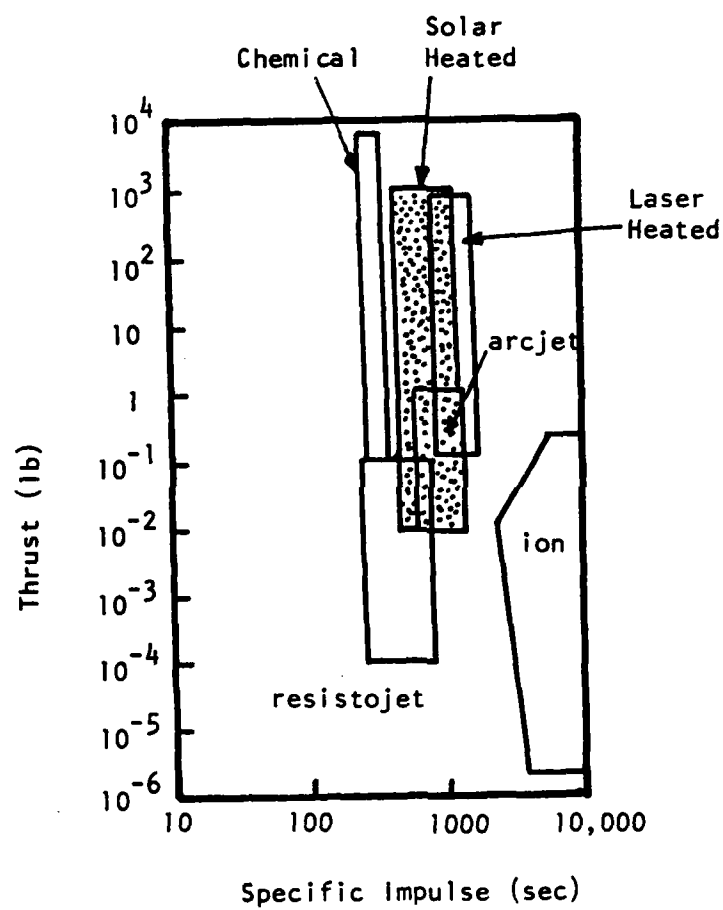
Fig. 1.   Comparison between different propulsion concepts

spacecraft. Unlike other potential beamed energy concepts, the power source for solar propulsion is currently available and the energy is already being beamed to orbital locations of interest (although there is a void inside the earth's shadow). There are no precise pointing and tracking requirements, nor is there uncertainty concerning the development or the characteristics of the source.

The primary challenge of solar thermal propulsion lies in identifying a method for coupling the solar energy into the thermal (kinetic) modes of the working fluid. Both direct and indirect absorption concepts have been considered for this purpose. Direct absorption requires advanced technology and longer development time. Indirect absorption requires current technology and can be implemented today, although it does suffer some performance penalties in comparison with potential direct absorption schemes.

In the direct absorption concept, solar radiation is absorbed directly into the flowing gas. Direct absorption of solar energy is difficult because of the low energy densities of the radiation. Even after concentration, solar intensities remain too low to be absorbed readily in most gases of interest. The combination of a trace amount of seedant gas such as alkali metal vapors with a bulk carrier gas such as hydrogen does, however, offer promise of providing acceptable absorption lengths[3], and studies of direct absorption based on this approach are currently underway[4].

Indirect absorption schemes are those in which the solar energy is incident upon the surface of a heat exchanger. The working fluid is then indirectly heated by passing it over this

3

heated surface. The maximum temperature in such an indirect absorption system is limited by material considerations and in general the full thermodynamic potential of the solar energy cannot be realized. Shoji[1] and Etheridge[2] have shown that through the use of realistic concentrators and high temperature materials, an indirectly heated solar propulsion system can provide specific impulses of some 870 seconds. This performance level is sufficient to provide a 45% increase in payload[2] as compared with conventional chemical propulsion systems for a one-way LEO to GEO mission. Construction of an indirectly heated solar thermal demonstration engine based upon these studies is currently underway at the Rocket Propulsion Laboratory[5]. The results of the present study are in support of this technology.

The particular aspect of solar propulsion which is addressed in the present study has to do with the severity of the interaction between the rocket exhaust plume and the solar concentrator. Appropriate geometries can be developed[2] which will ensure that the concentrator will remain outside the direct line of sight of the thrust vector for all orientations with respect to the sun, but the expansion of the exhaust plume away from this direct line of sight and the backflow of small fractions of the plume into the upstream quadrants will lead to plume/mirror impingement. The purpose of the present study is to assess the pressure and heat transfer loads that will be imposed on the mirror by this impingement. The discussion of the analytical methods used for making these estimates and the predicted loads themselves form the bulk of the present report.

GEOMETRIC AND THERMODYNAMIC CONFIGURATION OF THE SOLAR PROPULSION SYSTEM

Before delving into the details of the analytical method, an overview of the geometric characteristics of the solar propulsion system is warranted. The complete propulsion system consists of a collector that collects and focuses the solar energy and a rocket engine in which the working fluid is heated and expanded through a converging-diverging nozzle.

The size of the collector is dictated by the energy requirements of the engine. These, in turn, are determined by the thrust size of the engine and the peak temperature to which the fluid is heated. The peak temperature is set by thermodynamic and material constraints as outlined below while the thrust size is set by mission requirements. The net effect of these size considerations is a collector that is much larger than the engine. A representative sketch[2] of the combined system is given on Fig. 2. As can be seen, the rocket engine is little more than a dot in comparison to the collector size. This again is a result of the low energy densities of solar radiation. The picture also gives an indication of the degree of plume expansion which can be tolerated before the plume begins to impinge on the mirror surface. More specific details on this are given later.

The peak temperature of the working fluid determines the specific impulse of the rocket. From second law considerations, the maximum temperature must fall below the effective temperature of the sun's surface, 10,370 R (5760 K). The indirect absorption
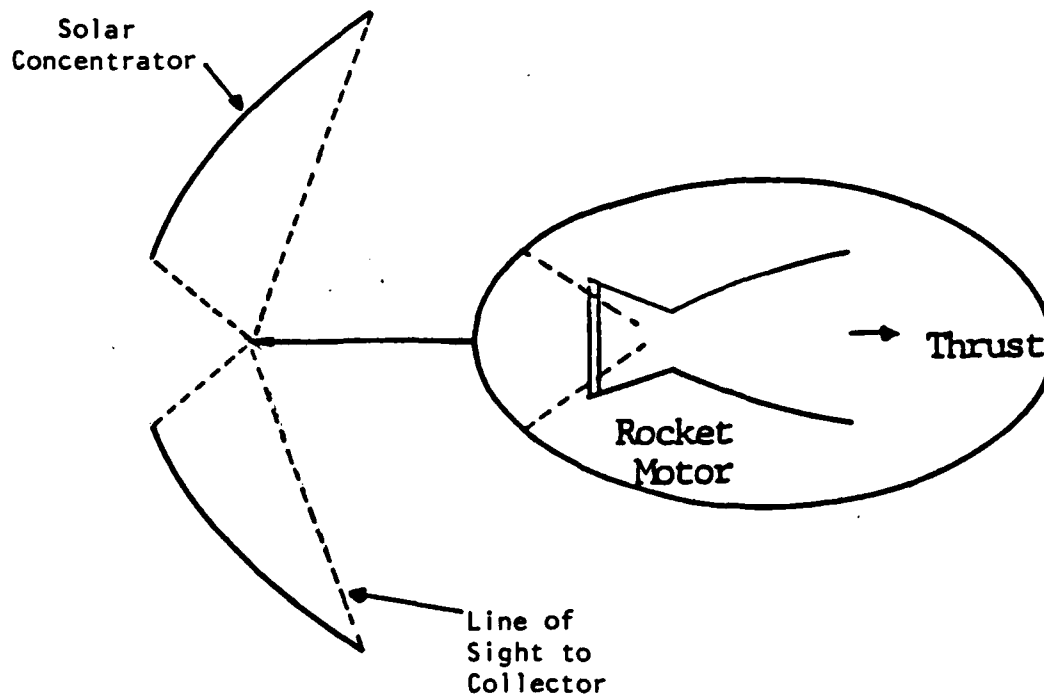
Fig. 2. Configuration of a Solar Rocket

system, however, is also restricted by material considerations. The present contamination estimates are based upon a technology that uses rhenium coils for the heat transfer surface[5]. Rhenium allows peak temperatures of about 5000 R (2780 K) corresponding to realizable I_{sp}'s of 800 to 1000 seconds[1,6], and this peak temperature is the one used for all the present calculations.

Once the working fluid temperature has been set, the engine size is determined by the thrust level. To provide generality, the thrust size was treated as a parameter. Thrust levels ranging from 1 to 500 lb_f were considered. Because of the importance of the nozzle wall boundary layer on the degree of impingement, the contamination effects cannot be scaled geometrically but must be recomputed for each thrust level. The engine size also depends upon the chamber pressure. Two chamber pressures, 50 and 100 psia, were considered.

The working fluid for an indirect absorption solar engine can be chosen almost entirely upon the basis of its molecular weight. In this regard, hydrogen appears to be the best choice and the properties of pure hydrogen were used for the present calculations.

The collector proposed in Refs. 1 and 2 was composed of a pair of inflated structures which are segments of a paraboloid. The axis of the paraboloid coincides with the thrust axis while the latus rectum of the parabola passes through the engine. The collector system can rotate about both the vehicle axis and an axis perpendicular to it so as to be able to track the sun irrespective of the direction of vehicle travel. As suggested above, the width of the parabola scales with the thrust level of the solar rocket.

The collector geometry used for the present contamination estimates is based upon a derivative of the geometry described in Ref. 1. The collector is still assumed to be composed of two segments of a paraboloid, but the axial extent of the paraboloid is somewhat shorter than that in Ref. 1. For our calculations, the axial extent of the collector is defined by straight lines emerging from the nozzle centerline at the exit plane at an angle of 72.5° with respect to the thrust axis (see Fig. 3). Only those streamlines that turn through angles larger than this will impinge on the collector. Finally, the pressure and heat transfer loadings on the front surface of the inflated surface (not the reflector surface itself) are reported. (The front surface is transparent while the back is reflective.) These geometric details are also given in Fig. 3.

SUMMARY AND OBJECTIVES OF THE RESEARCH

As indicated above, a solar concentrator design that remains outboard of the primary thrust direction for all thruster orientations with respect to the sun has been developed[1]. This prevents direct plume impingement on the collector surface, but there remain concerns about interactions between the outer fringes of the plume and the collector surface. This is because, in the vacuum of space, plume expansion causes portions of the exhaust gases, particularly those originating in the nozzle wall boundary layer, to escape into the forward hemisphere. The potential concern for any such interaction is heightened by the delicate nature of the concentrator which is envisioned as an

8
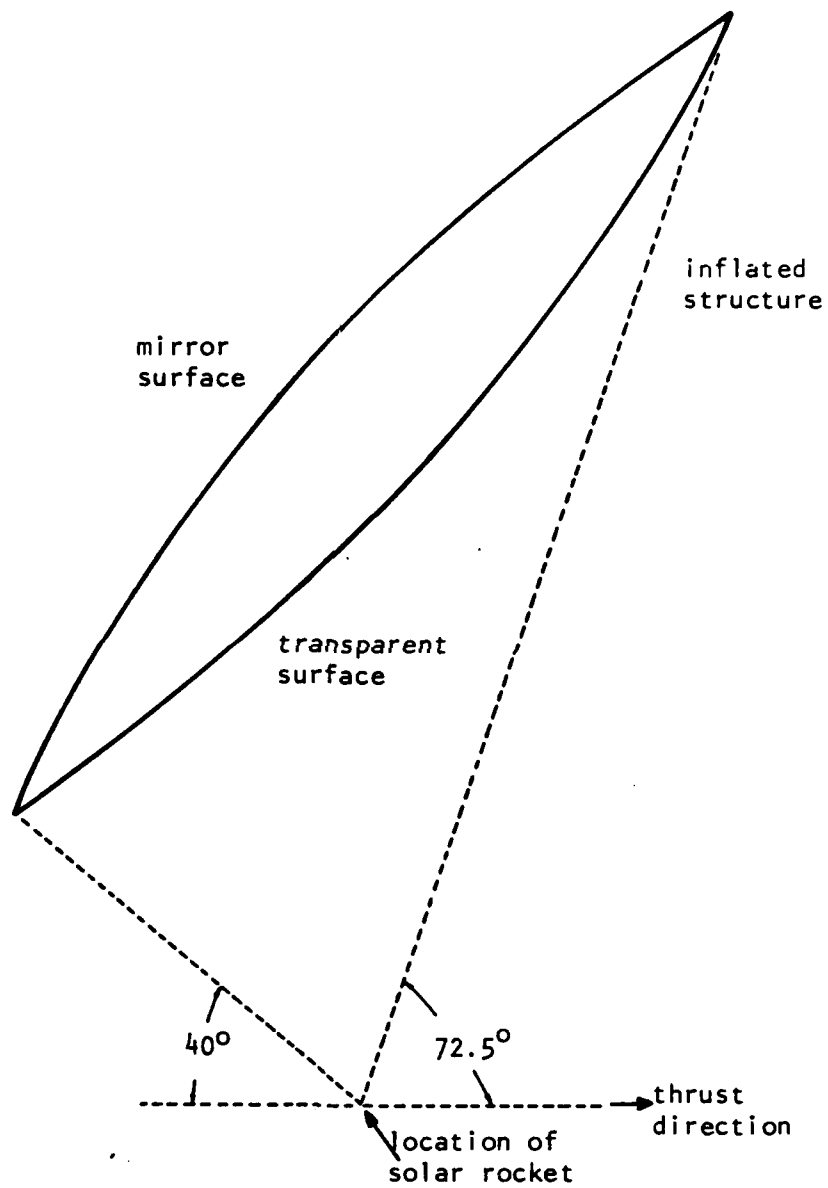
Fig. 3. Configuration of a Solar Concentrator

ultra-lightweight, inflated structure. The very low inflation pressures that are required to minimize hoop stresses in the extremely large sizes also imply that very low impingement pressures can deform the mirror surface and reduce the collector efficiency. In addition to the pressure forces, adverse effects of heat transfer from the plume to the collector can also cause damage and are likewise of interest.

To predict the plume impingement characteristics, calculations of the plume flowfield at distances of many radii from the nozzle exit plane are required. This plume calculation must be continued into the forward hemisphere. The data obtained from these calculations will lay the foundation for future analyses of concentrator deformation and its effect on thruster performance along with possible strategies for defeating the plume interaction. The approach taken here is to apply existing computational tools[7-9] to the solar rocket plume/mirror interaction to assess the order of magnitude of this interaction. Additional detailed studies at a later date will be required to verify some of the assumptions dictated by the present computational procedures. The problem described not only represents an important technological problem in the development of solar propulsion, but it also represents a challenging fundamental problem in fluid physics.

The specific objectives of the study are then to understand the physics of the interactions between the plume and the solar collector and to predict their magnitude. Of particular interest are the plume-induced pressure and heat transfer on the solar concentrator for various engine sizes and operating conditions.

This objective requires that the structure of both the nozzle and plume flowfields be known. Although our original intent was to use existing computational codes[7-9] to obtain this flowfield information, it became apparent during the effort that the existing procedures were not adequate for the low Reynolds number conditions in solar rockets. Consequently, it was necessary to develop a new procedure for low Reynolds number nozzle flows. The parabolized Navier-Stokes procedure that was developed is described in the present report along with the predictions of the plume/mirror interactions.

PHYSICAL DESCRIPTION OF THE FLOWFIELD

In order to estimate the level of the plume/mirror interactions, the flowfield from inside the nozzle all the way to the farfield plume must be calculated. Before getting into the task of simulating the flowfield, we first identify its basic structure and characteristics. We then use these basic physics to identify appropriate methods for dealing with each segment of the flowfield. The special features of the flowfield include the inviscid flow inside the nozzle, the boundary layer along the nozzle wall, the nearfield plume, the farfield plume and non-continuum regions near the nozzle lip and on the outer fringes of the plume. These basic regions are identified and characterized below.

BASIC STRUCTURE OF REAL EXHAUST JETS

The characteristic structure of inviscid supersonic jets exhausting from a nozzle is well known. For the near-vacuum conditions of space, the inviscid jet undergoes a Prandtl-Meyer expansion to the ambient pressure. This expansion causes the flow to turn through a finite angle, whose extent is strictly limited by thermodynamic considerations to a rigid upper maximum, even when the external environment is a hard vacuum. For a sonic jet with a ratio of specific heats of 1.4, this maximum turning angle is nominally 135°. The value of this maximum turning, however, decreases as the exit Mach number is increased. At the high supersonic speeds that are representative of conditions at the exit

plane of a typical high expansion ratio rocket nozzle, the turning angle is considerably less than 90°. For example, for an expansion nozzle with an area ratio of 100, the ideal exit Mach number is around 7, and the maximum turning angle, as obtained from the Prandtl-Meyer function, is only 35°. Thus, even with flow angularity present at the exit plane, an inviscid jet would remain confined to the aft quadrants.

This simple description, however, is valid only for ideal jets. A real exhaust jet will differ from this picture in two very important ways that have a major bearing on potential plume/mirror interactions. First, a real exhaust jet will always include a low velocity boundary layer on its outer periphery. The rotational flow in this boundary layer can in first approximation be treated as inviscid, but it contains a continuous range of Mach numbers from the high supersonic value of the inviscid core through the sonic value and all the way to zero at the wall. The exit flow near the sonic line can turn through approximately 135° (as modified by rotationality effects) and will most likely impinge on the collector. In addition, the subsonic portion of the boundary layer has no obvious turning limit imposed upon it and can presumably turn through even larger angles, again impinging on the collector. The relative turning of inviscid and inviscid-plus-boundary-layer jets is shown on Fig. 4.

The second reason that a real exhaust jet differs from the ideal, inviscid picture presented above is because of the rarefied effects that are incurred as the plume expands into a vacuum. These rarefied effects will also cause some molecules to deviate
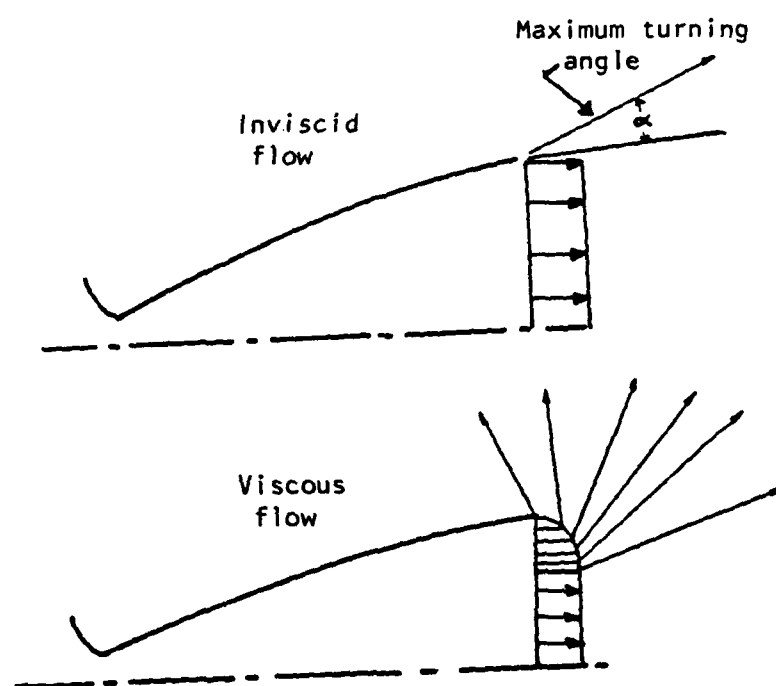
Fig. 4. <u>The relative turning of inviscid and inviscid-plus-boundary-layer jets</u>

from their inviscid course and will contribute to plume/mirror impingement even in the absence of a boundary layer.

The relative importance of boundary layer and rarefied effects upon plume/mirror interactions depends upon the nozzle Reynolds number. (The Knudsen number is of lesser significance because Knudsen numbers at the exit are generally still low enough that transition effects are determined by external conditions.) For solar rocket conditions, the nozzle Reynolds number is relatively low resulting in very thick boundary layers. These thick boundary layers dominate the plume/mirror interactions. Almost all of the mass that hits the collector originates in the boundary layer. The presence of rarefied flow effects only modifies the manner in which this mass flux is distributed over the mirror surface. Because this redistribution is a lower order effect, the present analysis concentrates on a continuum description of the contamination problem.

NOZZLE BOUNDARY LAYER CHARACTERISTICS

The dominant effect of the boundary layer flow upon the collector impingement problem implies that its development and character must be addressed in detail. The first issue to be discussed is the state of the boundary layer, that is, whether it is laminar or turbulent. The high Mach numbers, wall cooling and strong accelerations that characterize rocket nozzle boundary layers cause them to have considerably different transition characteristics than those observed in typical, incompressible, flat plate boundary layer experiments. The few experimental

15

studies of actual or simulated nozzle boundary layers that have
been conducted suggest that transition characteristics can be quite
complex[10-12]. In addition to undergoing transition from laminar to
turbulent flow, relaminarization from turbulent to laminar flow can
also take place. In a typical high Reynolds number nozzle, the
initial transition from a laminar to a turbulent boundary layer
occurs in the converging section upstream of the throat. The
strong accelerations downstream of the throat can, and frequently
do, cause this turbulent boundary layer to relaminarize once again
in the supersonic section. In high area ratio nozzles the length
could be sufficient to allow this relaminarized boundary layer to
undergo transition to turbulence a second time. Finally, in small,
low Reynolds number nozzles such as those of interest for solar
propulsion, the boundary layer could remain laminar all the way
from the subsonic region to the exit plane. The experimental data
available in no way exhaust the myriad of variables controlling
transition and relaminarization in nozzle boundary layers, but a
review of what information is available at least gives us some
guidance as to expected trends.

Back and co-workers[10-12] conducted experiments in a
converging-diverging nozzle and observed relaminarization in the
diverging section. Their measurements of relaminarization were
correlated on the basis of the throat Reynolds number. For throat
Reynolds numbers less than 2×10^6, relaminarization occurred,
whereas for Reynolds numbers above this value, the boundary layer
remained turbulent. Relaminarization appeared to be the result of
the suppression of turbulence production by the strong

accelerations. Their results also indicated that the heat transfer coefficient dropped dramatically when the turbulence intensity decreased.

An alternative correlation for the effects of acceleration on the turbulence in incompressible boundary layers was proposed by Moretti and Kays[13] who used as their criterion a Reynolds number based upon the characteristic distance over which the acceleration took place. They found that turbulence generation appeared to be completely inhibited when the parameter, K, defined as,

$$K = \frac{\nu}{u_e^2} \frac{dU_e}{dx}$$

exceeded 3.5×10^{-6}. (Note that K is the reciprocal of the Reynolds number based upon the acceleration distance.) Once turbulence generation ceased, the residual turbulence decayed and the boundary layer became effectively laminar in character.

These experimental results give some guidance for determining whether the boundary layer will be laminar or turbulent over most of its length, but they clearly do not define its state unequivocally. Wall cooling has a dramatic effect on boundary layer growth in supersonic flows and will most certainly affect whether or not relaminarization takes place. The increased length of the high area ratio nozzles of interest in solar thermal propulsion could also allow re-transition back to turbulence if relaminarization occurred. Most importantly, the Reynolds numbers for these smaller thrust engines is so low that transition may never take place and the entire boundary layer may remain laminar.

17

In the present calculations, the eddy viscosity computed with a two-layer model never exceeded the laminar value by more than a factor of fifteen even for the largest nozzles, and the implications are that fully turbulent boundary layers are never encountered.

THE INVISCID CORE INSIDE THE NOZZLE

The nozzle boundary layer describes the flow adjacent to the wall inside the nozzle. In addition to this viscous flow, the nozzle flow includes the inviscid core flow. In the diverging section, this core flow is completely supersonic and is governed by the familiar dynamics of inviscid supersonic flows. Consequently, little detail concerning its characteristics need be given. Suffice it to say that for the temperatures of interest (stagnation temperatures of 5000 R), the effects of dissociation and recombination in pure hydrogen are relatively minor and have been ignored in the present description. We also note that the interaction between the inviscid flow and the boundary layer is quite strong because the boundary layers of interest are so thick. Discussion of this effect is, however, delayed until Computational Procedures where the computational techniques are described.

NEAR AND FARFIELD PLUME CHARACTERISTICS

The rocket plume can be divided into a nearfield region and a farfield region depending upon the local physics of the plume. The nearfield region is characterized by strong accelerations and curving streamlines. The farfield is characterized by a more or

less geometric expansion and straight streamlines. In the farfield, the nozzle resembles a point source and the flowfield is essentially radial. For conditions representative of solar rocket plumes, the line of demarcation between these two regimes is some 150 nozzle throat radii from the exit plane.

The nearfield plume is dominated by the Prandtl-Meyer expansion that originates at the nozzle lip as depicted in Fig. 5. This expansion propagates through the rotational flow in the boundary layer and then on through the inviscid core where it reflects from the axis in traditional fashion. Even though the rotationality in the boundary layer is the result of viscous processes (and turbulence) the fluid dynamic effects that control this portion of the fluid after it leaves the nozzle are predominantly inviscid in nature and it is appropriate to speak of a Prandtl-Meyer expansion. The presence of the entropy gradient in the fluid originating in the boundary layer does cause some local distortions in the flowfield that are not present in the Prandtl-Meyer expansion of an isentropic fluid. Specifically, the total pressure gradient near the wall causes a lobe in the Mach number contours that would not be present if the flow were irrotational. The strong streamline curvature in the near plume that was noted earlier arises because of the flow turning that is induced by this Prandtl-Meyer expansion.

The farfield plume resembles the spherical expansion from a distributed source. Each individual element of fluid can be viewed as undergoing an isentropic expansion along a straight path from a fictitious source point at some location. Both the direction of

Nozzle Wall

Streamlines

Mach Lines
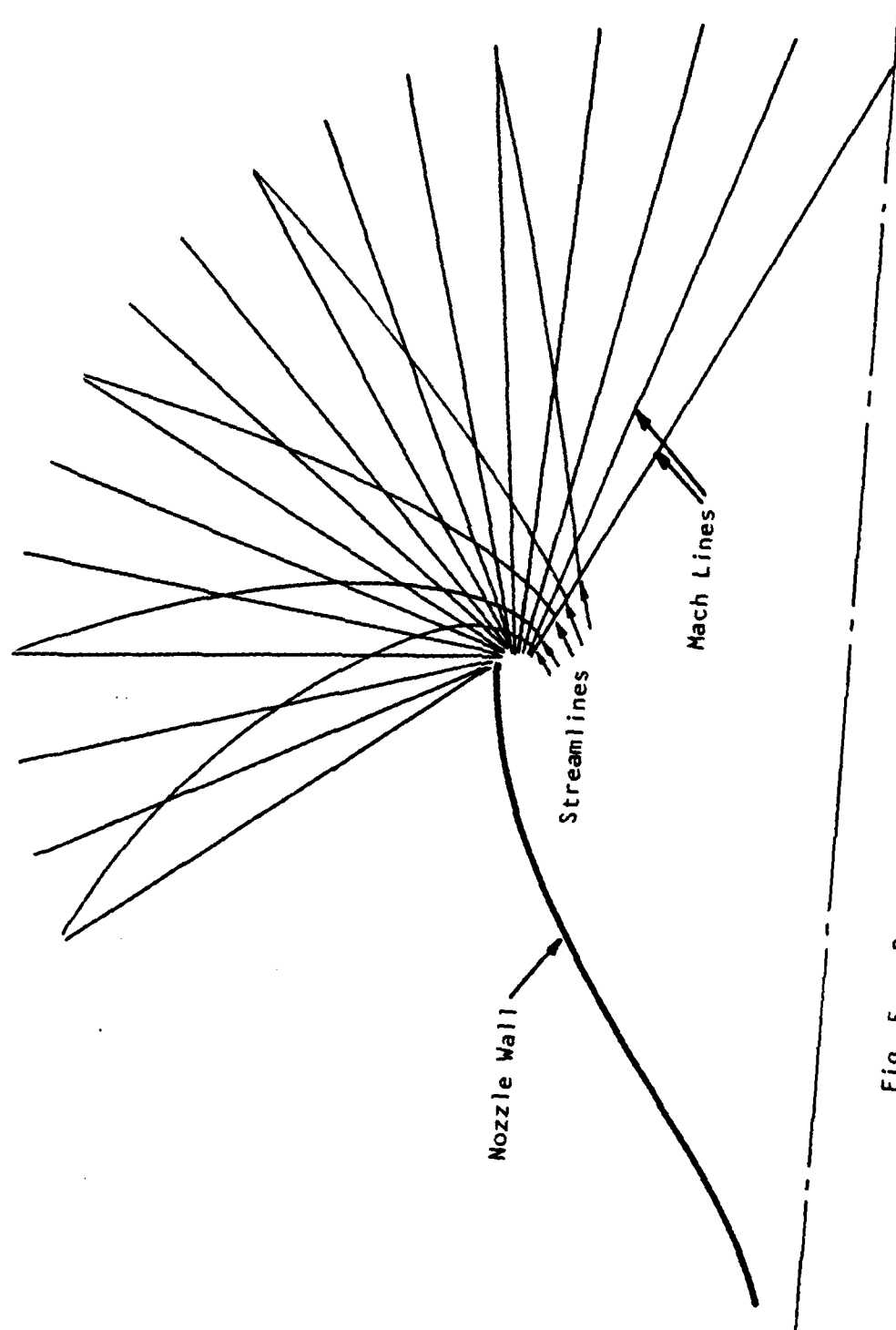
Fig. 5. Prandtl-Meyer expansion at nozzle lip

the straight path and the source location are determined by the nearfield plume physics. As this point-source expansion continues into the farfield, one-dimensional (spherical) theory indicates .that the Mach number increases indefinitely while the temperature of the particle approaches absolute zero. The expansion causes almost no change in the velocity of the particle. This nearly constant velocity trajectory is an excellent approximation to a collisionless rarefied flow. Similarly, the presence of very low absolute temperatures implies the random motion of the molecules is nearly depleted as they near the farfield regime and, hence, the directions of the continuum streamlines are also good approximations to those of molecules in non-continuum theory. Thus, whether the farfield is treated in a continuum manner or a non-continuum manner, the resulting characteristics are essentially analogous. More detailed discussion of non-continuum effects are given in the next Section.

NON-CONTINUUM EFFECTS

As an axisymmetric jet expands into a vacuum, its density becomes lower and lower until eventually the entire flow is governed by non-continuum conditions. For the exhaust jets considered here, the transitional effects begin on the outer edge of the jet as soon as it emerges from the nozzle lip, and spreads into its main body as it propagates away from the exit plane. Bird[14] has shown that the initial non-continuum effects that occur at the nozzle lip are local in nature and do not affect the continuum expansion of the jet. The non-continuum effects near the

21

lip do, however, have a substantial impact upon the amount of mass that expands into the upstream quadrants. The global characteristics of these local non-continuum effects are described here.

The details of the manner in which transitional effects modify an exhaust jet have been studied by Bird[14,15,16] using direct simulation Monte Carlo procedures. His analyses showed that the non-continuum aspects of the expansion of a real axisymmetric jet (a jet with a boundary layer) can be characterized by the density gradients along the streamlines. On the basis of Monte Carlo solutions for one-dimensional flows, Bird[14] defined an empirical breakdown criterion for determining when non-equilibrium effects become significant. He later applied this criterion to Prandtl-Meyer expansions[15] and rocket nozzle flows[16]. The criterion quantifies non-continuum effects as beginning when the non-dimensional parameter, P, defined as,

$$P = \frac{\pi}{4} \frac{\nu q}{p} \left| \frac{d\rho}{ds} \right|$$

exceeds 0.05. Here, q is the magnitude of the flow velocity, ν is the kinematic viscosity, p is the pressure, and $d\rho/ds$ is the density gradient along the streamlines. Regions of the jet where P is less than 0.05 are accurately predicted by continuum theory, while regions where P is more than 0.05 include non-equilibrium effects.

Representative exhaust plumes computed by Bird[16] for two different thrust levels are given in Fig. 6. These plots show Mach

22
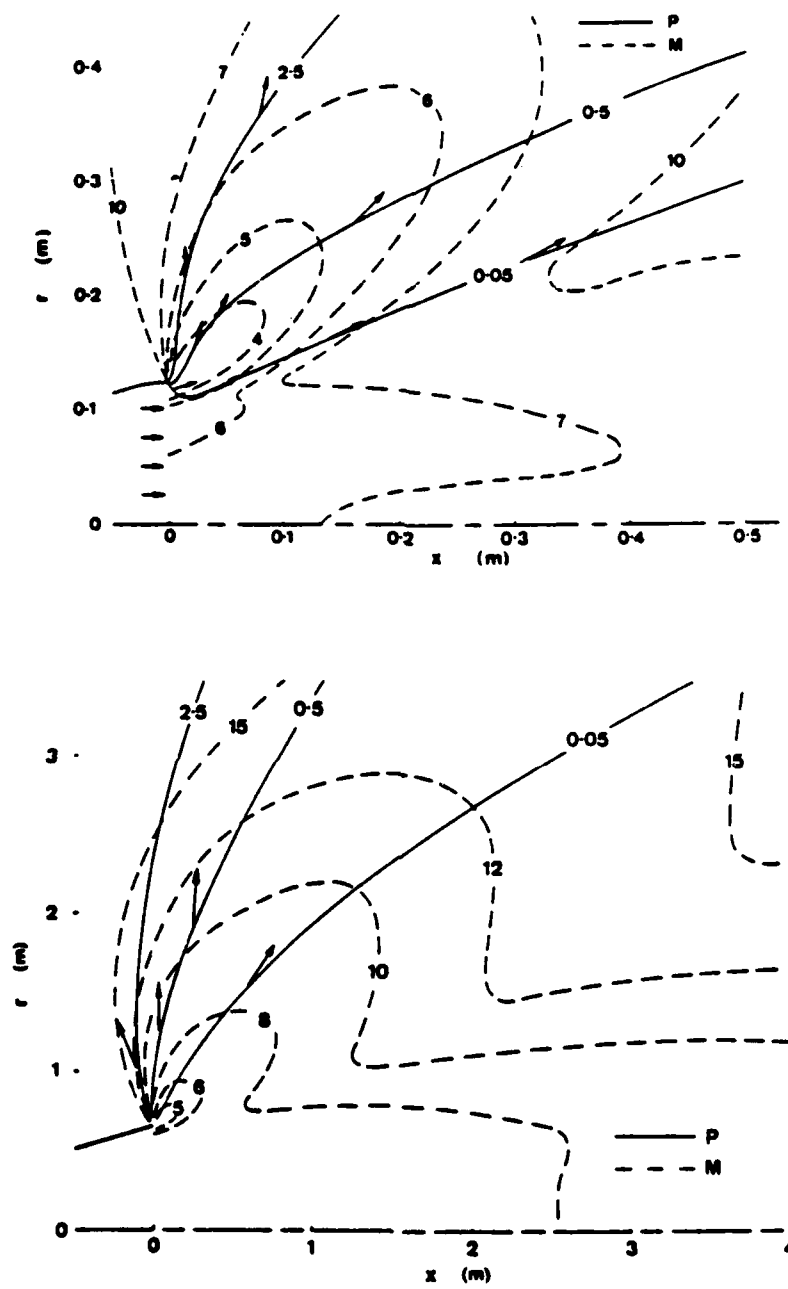
Fig. 6. Continuum expansion calculations of axisymmetric
exhaust jets for two different thrust sizes showing
criterion for transition to rarefied flow

number contours obtained from continuum MOC calculations along with contours of the transition criterion, P. Flow regions that lie outside the P = 0.05 contour are regions that have some non-continuum characteristics. In both cases, these non-continuum effects are restricted to the "lobe" region of the Mach number contours. As discussed earlier, this lobe region arises because of the effect of the rotational flow in the boundary layer on the Prandtl-Meyer expansion at the nozzle lip. These results suggest that near-field non-continuum effects become important for substantial fractions of the flow originating in the boundary layer for thrust levels like those of interest in the solar propulsion problem. The results also suggest that although most of the mass that eventually hits the solar mirror will have undergone non-equilibrium effects, the amount of mass hitting the mirror can be reasonably predicted by continuum theory. Non-equilibrium effects will have a more significant impact on how the plume contamination effects are dispersed across the mirror than on the fraction of the plume that hits the mirror.

SUMMARY OF VARIOUS FLOW REGIONS

The various flow regimes are presented schematically in Fig. 7 for nozzle flow conditions analogous to those expected for the solar thermal rocket. Inside the nozzle, the core flow is inviscid and irrotational, and the boundary layer grows along the nozzle wall. As the flow leaves the nozzle, the boundary layer occupies a substantial fraction of the nozzle radius. The irrotational, inviscid flow in the center of the nozzle undergoes a small turn as

24

it leaves the nozzle, but does not reach the 72° line of sight that would cause impingement on the collector. The rotational flow from the boundary layer spreads over a wide angular region and some of it enters the forward hemisphere. Thus, it is the boundary layer flow that is of primary interest for collector impingement. The computation of this boundary layer and its trajectory in the plume, however, requires that the irrotational core flow in the nozzle and in the plume be determined also.

The location of the P = 0.05 curve for nominal solar rocket plume conditions is also given in Fig. 7. This curve lies well inside the rotational flow originating in the boundary layer, but as noted above, most of the molecules impinging on the collector will exhibit non-continuum effects. Nevertheless, the dividing streamline that determines how much of the jet impinges on the collector can be determined by continuum theories. Non-continuum effects will only alter the spatial distribution of molecules on the surface of the collector. Accordingly, the present calculations are based on continuum approaches.
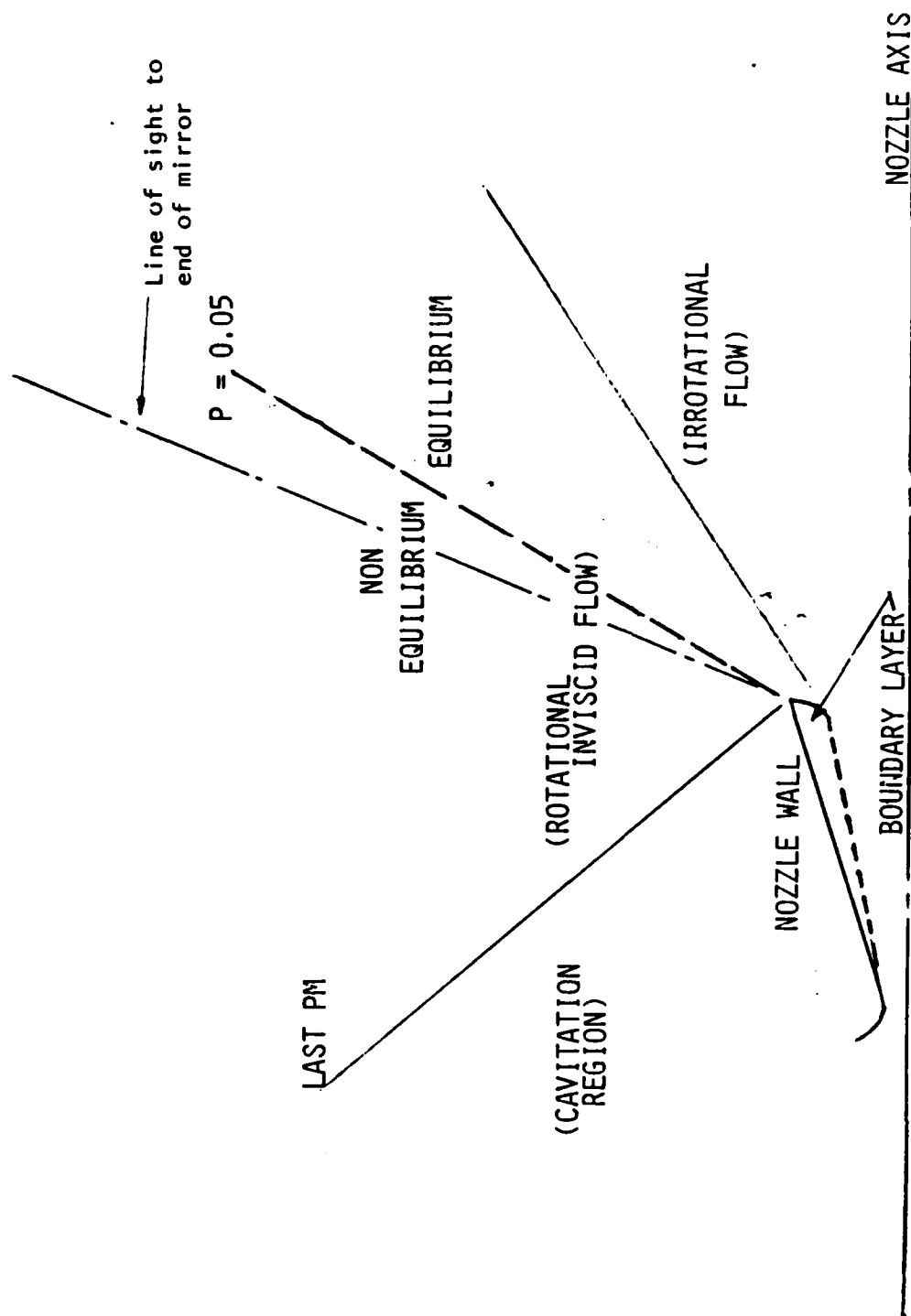
Fig. 7. Summary of different flow regions with different characteristics

COMPUTATIONAL PROCEDURES

The prediction of pressure and heat transfer effects in the plume at some distance from the nozzle exit plane requires that both the flowfield inside the nozzle and that in the plume be known. In order to calculate this information, the flowfield was split into several segments, each of which was calculated separately. The resulting flowfield was then obtained by patching these individual regions together.

Our original plan was to subdivide the flowfield into four segments, an inviscid and a boundary layer region in the nozzle, and a nearfield and farfield representation in the plume. Early results, however, showed that the Reynolds numbers were too low to allow uncoupled treatment of the viscous and inviscid effects in the nozzle, and these two segments had to be combined and computed simultaneously. The characterization of the four regions is still retained in the present section to document the nature of the flowfield and the reasons for switching to a unified treatment of the nozzle flow. The four regions of the flowfield are indicated on Fig. 8.

NOZZLE FLOWFIELD MODELING BY BOUNDARY-LAYER/INVISCID PATCHING

Flowfield modeling within the nozzle must take into account the inviscid supersonic character of the main flow, but it must also include the viscous effects near the wall because it is this boundary layer flow that will eventually make its way to the collector. There are several techniques available for computing

27

Collector

Farfield Plume
(Point Source)

Nearfield Plume
(MOC)

B.L.
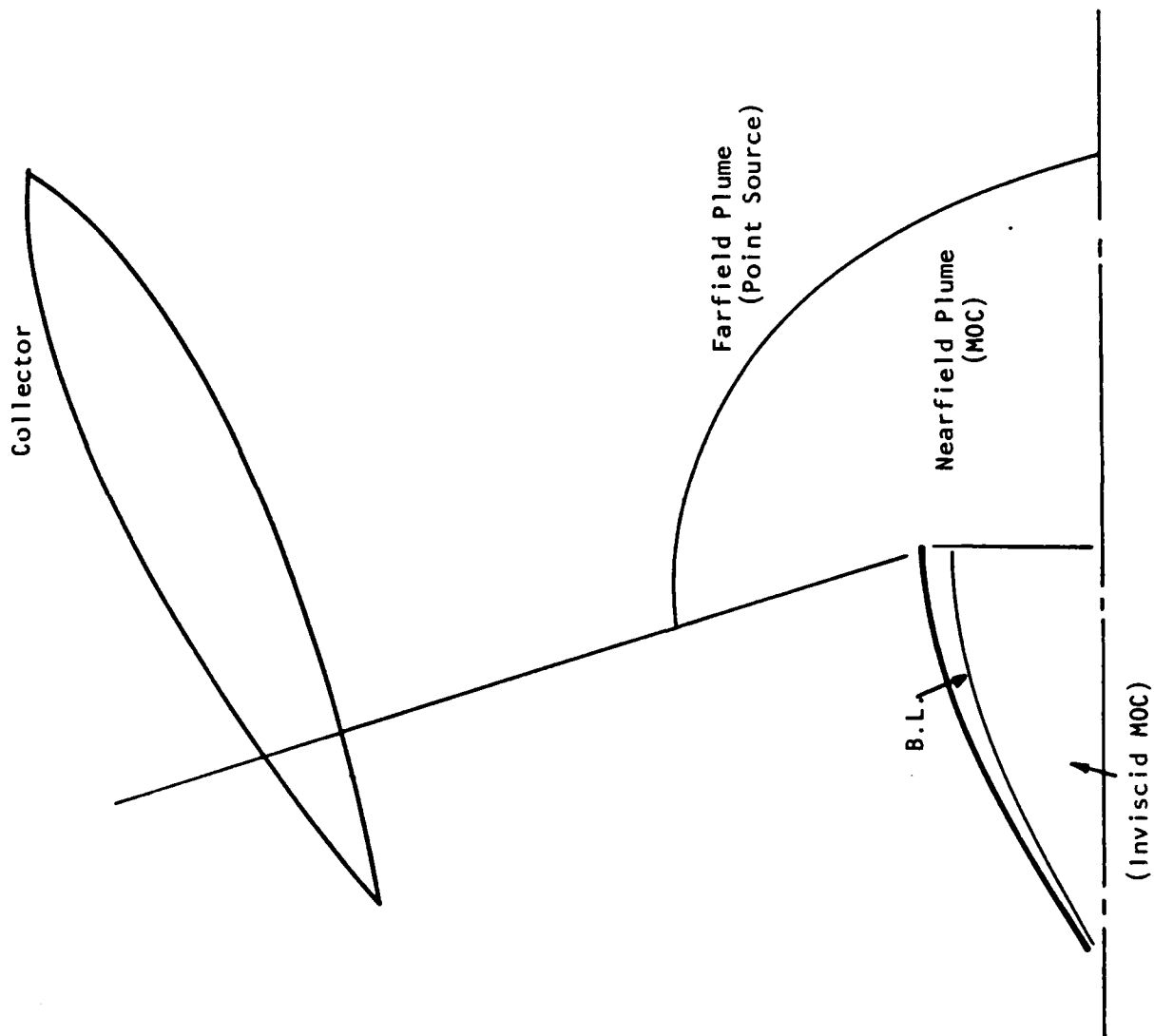
(Inviscid MOC)

Fig. 8. Division of flowfield into subregions for modeling purposes.
Final calculations combined the inviscid and boundary layer
regions inside the nozzle into a single region.

28

nozzle flowfields ranging from patched inviscid/boundary layer analyses to full Navier-Stokes solutions. We begin by estimating the boundary layer characteristics by a patching method and, because the Reynolds numbers of these low thrust nozzles are small, later use a parabolized Navier-Stokes procedure for our final nozzle flowfield predictions. Both of these procedures and their results are described herein.

Method of Characteristics Procedure

The patching procedure used for the initial estimates of the nozzle flowfield characteristics was based upon a combination of an inviscid Method of Characteristics (MOC) procedure[7], and a differential boundary layer solution procedure[17]. The MOC procedure chosen was the one contained in the CONTAM code[7]. The inviscid core flow calculations were started from a supersonic starting line downstream of the sonic line at the nozzle throat. This start line was taken from an approximate analysis of the transonic flow in the throat region. The pressure distribution obtained from the MOC procedure was then input to a boundary layer analysis to obtain the boundary layer and displacement thickness characteristics.

The MOC procedure in CONTAM considers an inviscid, perfect gas with variable specific heats and includes capability for rotational flow and axisymmetric geometries. The governing equations are listed in Table 1 and the resulting characteristic relations and compatibility conditions are given in Table 2. The same MOC procedure was also used for the plume analysis.

29

TABLE 1. GOVERNING EQUATIONS OF METHOD OF CHARACTERISTICS

$$\nabla(\rho\vec{V}) = 0$$

$$\rho\frac{D\vec{V}}{Dt} + \nabla p = 0$$

$$\frac{DP}{Dt} - a^2\frac{D\rho}{Dt} = 0$$

$$p = \rho RT$$

$$h = \int_{T_0}^{T} CpdT + h_0$$

TABLE 2. CHARACTERISTIC AND COMPATIBILITY EQUATIONS FROM METHOD OF CHARACTERISTICS

Characteristic Equations

$$\frac{dy}{dx}_0 = \lambda_0 = \frac{v}{u} \qquad \text{(streamlines)}$$

$$\frac{dy}{dx}_\pm = \lambda_\pm = \tan(\theta \pm \alpha) \qquad \text{(Mach lines)}$$

Compatibility Equations

$$\begin{aligned} \rho u du + \rho v dv + dp &= 0 \\ dp - a^2 d\rho &= 0 \end{aligned} \qquad \text{(along streamline)}$$

$$\rho v du_\pm - \rho u dv_\pm + [\lambda_\pm - \frac{u(u\lambda_\pm - v)}{a^2}] \, dP_\pm$$

$$-(u\lambda_\pm - v) \, \frac{\rho v}{y} \, dx_\pm = 0 \quad \text{(along Mach lines)}$$

Boundary Layer Solution Procedure

The boundary layer solution procedure that was used for the patched MOC/boundary layer calculations is a differential procedure that solves the complete partial differential form of the boundary layer equations[17]. This code is derivative of a code originally developed at NASA/Langley for external hypersonic boundary layers[18]. The equations are solved in a transformed Levy-Lees coordinate system using three-point implicit differencing in the streamwise

direction. Turbulence is treated by either a two-layer eddy-viscosity model or a mixing length formulation. Laminar to turbulent transition is handled by introducing an "intermittency" function that gradually "turns on" the turbulence at a specified location. Although the code was developed for supersonic boundary layers, the turbulence models are more representative of turbulence in conventional low speed boundary layers than in rocket nozzle boundary layers, and as such can be assumed to give only a representative description of such boundary layers. The code incorporates capability for specifying either the wall temperature or heat transfer, and representative values were used for all calculations reported here. The equations are solved in axisymmetric form with transverse curvature effects neglected.

It should be noted that CONTAM was also designed to handle the viscous portion of the flow inside a rocket nozzle as well as the inviscid portion. The boundary layer module in our version of CONTAM was, however, severely restricted in capabilities and did not appear appropriate for the present calculations. For example, the boundary layer module in CONTAM used an integral solution procedure that was restricted to fully turbulent boundary layers with the wall temperature equal to the freestream stagnation temperature. The restriction to turbulent boundary layers was particularly inappropriate for the very low Reynolds numbers that are representative of solar rocket nozzles. It appears that the boundary layers in these nozzles are predominantly laminar, not fully turbulent. The restriction on wall temperature caused the boundary layer thickness to be underestimated by nearly a factor of

31

two as compared with more realistic cooled boundary layers. Finally, the integral formulation assumes a power law profile, and this also appears inappropriate for a strongly accelerated, high Mach number boundary layer with significant wall cooling. In view of the significance of the boundary layer on mirror impingement a more accurate boundary layer procedure seemed appropriate. Therefore, as indicated above an alternative boundary layer procedure was chosen.

The specific reasons for choosing the particular boundary layer code were largely because of its availability and less importantly because of its familiarity to us. The interaction between the boundary layer module and the MOC code for the nozzle flow (TD2) was performed external to the CONTAM code. The appropriate output files from the MOC solution (TD2) were written to a file and stored. This file was then modified to give the format needed for input to the boundary layer code. Additional modifications to the plume MOC code (TD2P) were also required to enable it to accept the rotational flow start line from the differential boundary layer solution.

Details of the boundary layer formulation and the turbulence model are given in the Appendix.

Survey of Boundary Layer Thickness

The MOC-boundary layer procedure has been used to estimate the characteristics of the boundary layers in the 80% bell-shaped nozzle for five nozzle sizes corresponding to thrust levels of 1, 10, 50, 100 and 500 lb$_f$. Because the present analysis is for an

advanced propulsion system, a precise estimate of the nozzle wall temperature is not yet available. To circumvent this, boundary layer calculations were computed for four different wall temperatures (550, 1100, 1650, and 2200 R). The results are given in Table 3 which gives the boundary layer thickness at the nozzle exit as a percentage of the nozzle radius at the exit plane, δ/R_e; the displacement thickness at the exit as a fraction of nozzle radius, δ^*/R_e; and the momentum thickness Reynolds number at the exit, Re_θ. The columns at the far right give the nozzle exit radius in millimeters and indicates whether the calculations are based on laminar or turbulent flow. Note that calculations for the 10 lb_f nozzle were performed for both laminar and turbulent boundary layers.

The most striking feature of the Table is the very viscous nature of the nozzle flow. The boundary layer thickness, δ, generally reaches halfway to the axis. The displacement thicknesses range from 10 to 40%, and the Re_θ's range from below 100 to only 700 for the largest nozzle. Increased wall cooling reduces both the displacement thickness and the boundary layer thickness, but even at the lowest wall temperature (which is below expected wall operating temperatures), the boundary layers remain very thick. Although these calculations are useful for determining the general characteristics of the nozzle flows, it is clear that the patching between the inviscid and the boundary layer solutions is only satisfactory for the largest nozzle sizes and the coldest wall temperatures and it may be questionable there. A fully

coupled procedure that includes the viscous and inviscid effects
simultaneously is required.

TABLE 3. BOUNDARY LAYER CHARACTERISTICS FOR VARIOUS THRUST SIZES

80% Bell-Shaped Nozzle; Area Ratio, 100;
T° = 2760K; P° = 50 psia

T_w (R)/ Thrust(lb_f)	Para-meter	550	1100	1650	2200	R^* (mm)	BL State
1	δ/Re	.41	.47	.51	.56		
	δ^*/R_e	.20	.28	.34	.41	1.5	L
	Re	46	41	37	33		
10	δ/Re	.24	.28	.31	.34		
	δ^*/R_e	.12	.17	.21	.25	4.8	L
	Re	81	73	65	58		
10	δ/Re	.40	.48	.57	.65		
	δ^*/R_e	.17	.27	.38	.47	4.8	T
	Re	130	138	138	133		
50	δ/Re	.33	.41	.49	.57		
	δ^*/R_e	.14	.23	.32	.42	10.8	T
	Re	231	254	263	259		
100	δ/Re	.30	.39	.47	.55		
	δ^*/R_e	.13	.21	.31	.40	15.3	T
	Re	299	334	350	349		
500	δ/Re	.26	.32	.43	.51		
	δ^*/R_e	.11	.19	.28	.37	34.3	T
	Re	599	650	703	717		

NOZZLE FLOWFIELD MODELING BY PARABOLIZED NAVIER-STOKES ANALYSIS

The above estimates of boundary layer thicknesses show that a
patched viscous/inviscid solution procedure is not acceptable. The
very viscous conditions dictate that the boundary layer and
inviscid flows be solved in coupled fashion. Accordingly, a
parabolized scheme that is valid in both viscous and inviscid
portions of the flowfield has been selected. Previous results[19]
have shown that the parabolized Navier-Stokes (PNS) equations are

effective for predicting such supersonic, viscous flowfields.
Because they can be solved in a marching fashion, the computational
effort required to solve the PNS equations is not much greater than
that required to solve the Method-of-Characteristics/boundary-layer
combination.

The parabolized equations used for this purpose are developed
in this section along with the solution procedure used for solving
them. Although the parabolized equations are generally solved by a
space marching procedure, a different approach was taken here. To
minimize code development time, the parabolized equations were
solved by an iterative time-marching procedure that was obtained by
modifying a full Navier-Stokes code. This marching procedure is
several times slower per x-step than a space-marching procedure,
but accuracy advantages of the time-marching scheme partially
offset this so that, overall, the procedure is within a factor of
two of more traditional schemes. Space-marching schemes are to be
preferred over the present procedure, but the differences are
slight.

In areas where the present procedure is different from more
conventional parabolized schemes, the reasons for the differences
and their impact on the solutions and solution procedures is
clearly indicated.

Development of the Parabolized Navier-Stokes Equations

The unsteady Navier-Stokes equations for an axisymmetric flow
without body forces or external heat addition can be written in
conservative form in cylindrical coordinates as,

$$\frac{\partial Q}{\partial t} + \frac{\partial E}{\partial x} + \frac{\partial F}{\partial y} = \frac{\partial E_v}{\partial x} + \frac{\partial F_v}{\partial y} + H \tag{1}$$

where x represents the streamwise direction and r represents the radial direction. The vector of primary dependent variables is,

$$Q = \begin{bmatrix} \rho y \\ \rho u y \\ \rho v y \\ e y \end{bmatrix} \tag{2}$$

The vectors representing the inviscid and viscous flux vectors and the source term are,

$$E = \begin{bmatrix} \rho u y \\ \rho u^2 y + p y \\ \rho u v y \\ u(e+p)y \end{bmatrix} \tag{3}$$

$$F = \begin{bmatrix} \rho v y \\ \rho u v y \\ \rho v^2 y + p y \\ v(e+p)y \end{bmatrix} \tag{4}$$

$$E_v = \begin{bmatrix} 0 \\ y\sigma_{xx} \\ y\sigma_{xy} \\ ky\frac{\partial T}{\partial x} + vy\,\sigma_{xy} + uy\,\sigma_{xx} \end{bmatrix} \tag{5}$$

$$F_v = \begin{bmatrix} 0 \\ y\sigma_{xy} \\ y\sigma_{yy} \\ ky\frac{\partial T}{\partial y} + vy\,\sigma_{yy} + uy\,\sigma_{xy} \end{bmatrix} \tag{6}$$

$$H = \begin{bmatrix} 0 \\ 0 \\ p - 2\mu \dfrac{v}{y} + \dfrac{2}{3} \mu \, \nabla \cdot \vec{u} \\ 0 \end{bmatrix} \tag{7}$$

The total energy and shear stress terms are,

$$e = \frac{\rho}{2} (u^2 + v^2) + \rho v T$$

$$\sigma_{xx} = 2\mu \frac{\partial u}{\partial x} - \frac{2}{3} \mu \nabla \cdot \vec{v}$$

$$\sigma_{xy} = \mu \left(\frac{\partial v}{\partial x} + \frac{\partial u}{\partial y} \right)$$

$$\sigma_{yy} = 2\mu \frac{\partial v}{\partial y} - \frac{2}{3} \mu \nabla \cdot \vec{v} \tag{8}$$

In order to close the system of equations, the perfect gas equation of state is used:

$$p = \rho R T \tag{9}$$

and the viscosity, μ, is determined from Sutherland's equation,

$$T^{3/2} = \frac{1 + c}{T + c} \tag{10}$$

where $c = 270$ for hydrogen. The conductivity, k, is determined from the Prandtl number which is specified as a constant, $Pr = 0.7$.

A transformation of the form,

$$\xi = \xi(x, y)$$

$$\eta = \eta(x, y) \tag{11}$$

is used to transform the governing equations into a generalized, non-orthogonal coordinate system. When this transformation is

37

applied to the differential operators in Eqn. 1, the equations become:

$$\frac{\partial \hat{Q}}{\partial t} + \frac{\partial \hat{E}}{\partial \xi} + \frac{\partial \hat{F}}{\partial \eta} = \frac{\partial \hat{E}_v}{\partial \xi} + \frac{\partial \hat{F}_v}{\partial \eta} + \hat{H} \tag{12}$$

where,

$$\hat{Q} = \frac{Q}{J}$$

$$\hat{H} = \frac{H}{J}$$

$$\hat{E} = \frac{1}{J} (E\xi_x + F\xi_y)$$

$$\hat{F} = \frac{1}{J} (E\eta_x + F\eta_y)$$

$$\hat{E}_v = \frac{1}{J} (E_v\xi_x + F_v\xi_y)$$

$$\hat{F}_v = \frac{1}{J} (E_v\eta_x + F_v\eta_y) \tag{13}$$

Here, J is the Jacobian of the transformation and is evaluated as,

$$J = \xi_x\eta_y - \eta_x\xi_y \tag{14}$$

The parabolized Navier-Stokes equations are derived from the complete Navier-Stokes equations given as Eqn. 12 by neglecting streamwise diffusion and retaining only cross-stream diffusion. In this procedure, it is inherently assumed that the transformed coordinate lies "nearly" along the streamlines. Consequently, all diffusion terms that include derivatives in the ξ-direction are dropped. Upon doing this, Eqn 12 reduces to,

$$\frac{\partial \hat{Q}}{\partial t} + \frac{\partial \hat{E}}{\partial \xi} + \frac{\partial \hat{F}}{\partial \eta} = \frac{\partial \hat{F}_v}{\partial \eta} + \hat{H} \tag{15}$$

where the vectors $\hat{F}_v$ and $\hat{H}$ are redefined such that all partial derivatives with respect to ξ are omitted.

38

The final definition of the flux vectors in the parabolized Navier-Stokes equations (Eqn. 15) is:

$$\hat{Q} = \frac{y}{J} \begin{bmatrix} \rho \\ \rho u \\ \rho v \\ e \end{bmatrix} \tag{16}$$

$$\hat{E} = \frac{y}{J} \begin{bmatrix} \rho U \\ \rho U u + p\xi_x \\ \rho U v + p\xi_y \\ (e+p)U \end{bmatrix} \qquad \hat{F} = \frac{y}{J} \begin{bmatrix} \rho V \\ \rho u V + p\eta_x \\ \rho v V + p\eta_y \\ (e+p)V \end{bmatrix} \tag{17}$$

$$\hat{H} = \frac{1}{J} \begin{bmatrix} 0 \\ -\frac{2}{3}\eta_x \frac{\partial uv}{\partial \eta} \\ p - \frac{4}{3}\mu\frac{v}{y} + \frac{2}{3}\mu\eta_x\frac{\partial u}{\partial \eta} - \frac{2}{3}v\eta_y\frac{\partial \mu}{\partial \eta} \\ -\frac{2}{3}\eta_x\frac{\partial}{\partial \eta}(\mu uv) - \frac{2}{3}\eta_y\frac{\partial}{\partial \eta}(\mu v^2) \end{bmatrix} \tag{18}$$

$$\hat{F}_v = \frac{y}{J} \begin{bmatrix} 0 \\ \mu(\frac{4}{3}\eta_x^2 + \eta_y^2)\frac{\partial u}{\partial \eta} + \frac{1}{3}\mu\,\eta_x\eta_y\frac{\partial v}{\partial \eta} \\ \mu(\eta_x^2 + \frac{4}{3}\eta_y^2)\frac{\partial v}{\partial \eta} + \frac{1}{3}\mu\,\eta_x\eta_y\frac{\partial u}{\partial \eta} \\ k(\eta_x^2 + \eta_y^2)\frac{\partial T}{\partial \eta} + \mu[\frac{1}{3}\eta_x\eta_y\frac{\partial}{\partial \eta}uv + \\ (\frac{2}{3}\eta_x^2 + \frac{1}{2}\eta_y^2)\frac{\partial}{\partial \eta}u^2 + (\frac{1}{2}\eta_x^2 + \frac{2}{3}\eta_y^2)\frac{\partial v^2}{\partial \eta}] \end{bmatrix} \tag{19}$$

where the contravariant velocities U and V are,

$$U = u\xi_x + v\xi_y$$
$$V = u\eta_x + u\eta_y \tag{20}$$

Note, in particular, the viscous dissipation terms must be retained for this supersonic flow problem.

Treatment of the Pressure Gradient Term

The form of the parabolized Navier-Stokes equations given as Eqn. 15 allows marching in the ξ-direction when the flow is supersonic and the streamwise velocity component is positive. In regions where the flow is subsonic, the streamwise pressure gradient, $\partial p/\partial \xi$, allows information to be propagated in the upstream direction and the marching procedure breaks down. In rocket nozzle flowfields, the flow is supersonic throughout most of the divergent section, but the presence of the no-slip condition on the wall ensures that there will always be at least a thin subsonic zone in the boundary layer. This small subsonic region prevents a straightforward marching solution of Eqn. 15. Some type of correction procedure must be used to circumvent this problem.

Potential techniques for dealing with this subsonic region can vary from using a full iterative method to solve Eqn. 15, to the simple expedient of dropping the offending pressure gradient term anytime the Mach number drops below unity. The former choice implies an order of magnitude increase in computation time, while the latter introduces unacceptable error. Because of this, a number of intermediate approaches have been suggested. Lubard and Helliwell[19] employed a backward difference formula for $dp/d\xi$ in the subsonic layer and were able to obtain marching solutions, but their procedure proved to be unstable if the streamwise step was made too small. Rubin and Lin[20] proposed a sublayer approximation in which the pressure gradient in the subsonic region is evaluated at an adjacent supersonic point. This approximation is based on

the reasonable assumption that $dp/d\eta$ is negligible in the subsonic viscous layer. The sublayer approximation was also used by Schiff and Steger[21] who, in addition, removed the streamwise pressure gradient from the energy equation in the sublayer region. Nevertheless, they still encountered departure solutions, and had to employ a global iteration instead of a single sweep marching procedure.

The most effective technique for handling the pressure gradient term is the one proposed by Vigneron[22] et al. In this approach, a fraction of the pressure gradient term $\omega(\partial p/\partial \xi)$ is retained in the subsonic viscous region and the remainder $(1-\omega)$ $dp/d\xi$ is separated out and either evaluated outside the subsonic region as with the sublayer approximation, or is totally dropped. Vigneron's technique is the one adopted for our PNS calculations of nozzle flows. The method for estimating the magnitude of ω and the justification that this technique will allow streamwise marching can both be demonstrated by a stability analysis of the equations of motion[23]. The details of this analysis are not given. We only note here that the value used for ω is given by,

$$\omega \leq \frac{\gamma M_\xi^2}{1+(\gamma-1)M_\xi^2} \qquad (21)$$

where M_ξ is the component of the Mach number in the ξ-direction.

With the Vigneron treatment of the pressure term, the parabolized Navier-Stokes equations retain the same form as Eqn. 15 except that the flux vector, $\hat{E}$, is split into two parts as,

$$\hat{E} = \hat{E}_1 + \hat{E}_2 \qquad (22)$$

where,

$$\hat{E}_1 = \frac{y}{J} \begin{bmatrix} \rho U \\ \rho u U + \omega p \xi_x \\ \rho v U + \omega p \xi_y \\ (e+p)U \end{bmatrix} \qquad \hat{E}_2 = \frac{y}{J} \begin{bmatrix} 0 \\ (1-\omega)\, p \xi_x \\ (1-\omega)\, p \xi_y \\ 0 \end{bmatrix} \qquad (23)$$

The parameter, ω, has the value unity when M_ξ is supersonic and is given by Eqn. 21 when M_ξ is subsonic. This implies that $\hat{E}_2$ vanishes identically in supersonic regions so that Eqn. 23 is identical to Eqn. 15 when $M_\xi > 1$. The only change in the formulation is in the narrow subsonic layer near the wall. Using this notation, the parabolized Navier-Stokes equations become,

$$\frac{\partial \hat{Q}}{\partial t} + \frac{\partial \hat{E}_1}{\partial \xi} + \frac{\partial \hat{E}_2}{\partial \xi} + \frac{\partial \hat{F}}{\partial \eta} = \frac{\partial \hat{F}_v}{\partial \eta} + \hat{H} \qquad (24)$$

In applying Eqn. 24, two additional modifications have generally been used. The first is that the vector $\hat{E}_2$ is generally treated in some approximate manner and is frequently neglected. In all of our calculations, $\partial \hat{E}_2 / \partial \xi$ has been ignored. The second modification is that the value of ω as determined by Eqn. 21 is generally multiplied by a safety factor to insure stability. Thus, the quantity ω, in Eqn 23 is replaced by $\omega' = \sigma \omega$ where σ is less than one. Setting σ near or equal to one generally leads to instabilities in space-marching solutions. The rule of thumb is that $\sigma \leq 0.85$. In our time-marching PNS solutions, the use of a safety factor was not necessary. In fact, calculations with $\sigma = 0.85$ proved to be inferior to ones with $\sigma = 1.0$, so all results shown are for $\sigma = 1.0$. This increased stability is one of the

advantages gained by using the time dependent version of the equations.

Numerical Solution of the Parabolized Equations

In the present Section, we describe the solution method for the time-marching procedure and compare it with the more commonly used space-marching procedure. In our discussions, the vector $\hat{E}_2$ (see Eqn. 24) is neglected.

As a first step in solving the parabolized equations, we express the flux vectors $\hat{E}_1$, $\hat{F}$, and $\hat{H}$ in Eqn. 3.24 as functions of the dependent variable $\hat{Q}$. We also re-write the viscous vector, $\hat{F}_v$, in a more convenient form. The former step is accomplished by introducing the Jacobians,

$$A_1 = \frac{\partial \hat{E}_1}{\partial \hat{Q}} \qquad B = \frac{\partial \hat{F}}{\partial \hat{Q}} \qquad D = \frac{\partial \hat{H}}{\partial \hat{Q}} \tag{25}$$

Performing the differentiations indicated in Eqn. 25 gives:

$$
A_1 = \begin{bmatrix}
0 & \xi_x & \xi_y & 0 \\[2ex]
-u\bar{U} + \xi_x \omega \frac{\gamma-1}{2}(u^2+v^2) & \bar{V} + (1-\omega(\gamma-1))\xi_x u & u\xi_y - \omega\xi_x(\gamma-1)v & \omega\xi_x(\gamma-1) \\[2ex]
-v\bar{U} + \xi_y \omega \frac{\gamma-1}{2}(u^2+v^2) & v\xi_x - (\gamma-1)\xi_y \omega u & \bar{U} + (1-\omega(\gamma-1))v\xi_x & \omega\xi_y(\gamma-1) \\[2ex]
\left[\frac{\gamma-2}{2}(u^2+v^2) - \frac{c^2}{\gamma-1}\right]\bar{U} & -(\gamma-1)u\bar{U} + \left[\frac{c^2}{\gamma-1}+\frac{u^2+v^2}{2}\right]\xi_x & -(\gamma-1)v\bar{U} + \left[\frac{c^2}{\gamma-1}+\frac{u^2+v^2}{2}\right]\xi_x & \gamma U
\end{bmatrix} \tag{26}
$$

43

$$B = \begin{bmatrix} 0 & \eta_x & \eta_y & 0 \\[2ex] -u\bar{V} + \eta_x\frac{(\gamma-1)}{2}(u^2+v^2) & \bar{V} - (\gamma-2)\eta_x u & \eta_y u - (\gamma-1)\eta_x v & (\gamma-1)\eta_x \\[2ex] -v\bar{V} + \eta_y\frac{(\gamma-1)}{2}(u^2+v^2) & -(\gamma-1)\eta_y u + \eta_x v & \bar{V} - (\gamma-2)\eta_y v & (\gamma-1)\eta_y \\[2ex] \left[\frac{\gamma-2}{2}(u^2+v^2) - \frac{c^2}{\gamma-1}\right]\bar{V} & -(\gamma-1)u\bar{V} + \left[\frac{c^2}{\gamma-1}+\frac{u^2+v^2}{2}\right]\eta_x & -(\gamma-1)v\bar{V} + \left[\frac{c^2}{\gamma-1}+\frac{u^2+v^2}{2}\right]\eta_y & \gamma\bar{V} \end{bmatrix} \quad (27)$$

$$D = \begin{bmatrix} 0 & 0 & 0 & 0 \\[2ex] \frac{2}{3}\frac{\eta_x}{J}\frac{\partial}{\partial\eta}(\mu\frac{v}{\rho}) & 0 & -\frac{2}{3}\frac{\eta_x}{J}\frac{\partial}{\partial\eta}(\frac{\mu}{\rho}) & 0 \\[2ex] -\frac{\gamma-1}{2J}(u^2+v^2) + \frac{4}{3}\frac{\mu}{yJ}\frac{v}{\rho} - \frac{2}{3}\frac{\mu\eta_x}{J}\frac{\partial}{\partial\eta}(\frac{u}{\rho}) & -\frac{\gamma-1}{J}u + \frac{2}{3}\mu\frac{\eta_x}{J}\frac{\partial}{\partial\eta}(\frac{1}{\rho}) & -\frac{\gamma}{J}\rho v - \frac{4}{3}\frac{\mu}{yJ}\frac{1}{\rho} & \frac{\gamma-1}{J} \\[2ex] \frac{4}{3}\frac{\eta_x}{J}\frac{\partial}{\partial\eta}(\mu\frac{uv}{\rho}) + \frac{4}{3}\frac{\eta_y}{J}\frac{\partial}{\partial\eta}(\mu\frac{v^2}{\rho}) & -\frac{2}{3}\frac{\eta_x}{J}\frac{\partial}{\partial\eta}(\mu\frac{v}{\rho}) & -\frac{2}{3}\frac{\eta_x}{J}\frac{\partial}{\partial\eta}(\mu\frac{u}{\rho}) - \frac{4}{3}\frac{\eta_y}{J}\frac{\partial}{\partial\eta}(\mu\frac{v}{\rho}) & 0 \end{bmatrix} \quad (28)$$

The viscous vector, F_v, is expressed as the product of a matrix and a vector,

$$\hat{F}_v = R_v \frac{\partial Q_v}{\partial \eta} \quad (29)$$

44

where Q_V contains the unknowns that appear in the viscous derivatives,

$$Q_V = (\rho, u, v, T)^T \qquad (30)$$

and R_V contains primarily the viscosity and thermal conductivity and the metric coefficients,

$$R_V = \begin{bmatrix} 0 & 0 & 0 & 0 \\ 0 & (\frac{4}{3}\eta_x^2 + \eta_y^2)\mu & \frac{1}{3}\eta_x\eta_y\mu & 0 \\ 0 & \frac{1}{3}\eta_x\eta_y\mu & (\eta_x^2 + \frac{4}{3}\eta_y^2)\mu & 0 \\ 0 & \mu[\frac{1}{3}\eta_x\eta_y v + (\frac{4}{3}\eta_x^2 + \eta_y^2)u] & \mu[\frac{1}{3}\eta_x\eta_y u + (\eta_x^2 + \frac{4}{3}\eta_y^2)v] & k(\eta_x^2 + \eta_y^2) \end{bmatrix} \qquad (31)$$

We also interpret Q_V as a function of Q and take its Jacobian,

$$B_V = \partial Q_V / \partial Q \qquad (32)$$

where,

$$B_V = \begin{bmatrix} 1 & 0 & 0 & 0 \\ -u/\rho & 1/\rho & 0 & 0 \\ -v/\rho & 0 & 1/\rho & 0 \\ -\frac{T}{\rho} + \frac{\gamma-1}{2\rho R}(u^2+v^2) & -\frac{(\gamma-1)u}{\rho R} & -\frac{(\gamma-1)v}{\rho R} & \frac{\gamma-1}{\rho R} \end{bmatrix} \qquad (33)$$

With these definitions, and noting that E, F, and H are homogeneous, such that,

$$\hat{E}_1 = A_1\hat{Q}, \quad \hat{F} = B\hat{Q}, \quad \hat{H} = D\hat{Q} \qquad (34)$$

we can write Eqn. 24 as,

$$\frac{\partial \hat{Q}}{\partial t} + \frac{\partial}{\partial \xi}A_1\hat{Q} + \frac{\partial}{\partial \eta}B\hat{Q} = \frac{\partial}{\partial \eta}A_V\frac{\partial Q_V}{\partial \eta} - D\hat{Q} \qquad (35)$$

Upon discretizing in time using Euler implicit differencing, this becomes,

$$\hat{Q}^{n+1} - \hat{Q}^n + \Delta t(-D + \frac{\partial}{\partial \xi}A_1 + \frac{\partial}{\partial \eta}B - \frac{\partial}{\partial \eta}R_v \frac{\partial}{\partial \eta}B_v)\hat{Q}^{n+1} = 0 \qquad (36)$$

where superscripts refer to the time step, and the quantity in parenthesis is to be interpreted as an operator operating on $\hat{Q}^{n+1}$. Expressing this in delta form gives,

$$(I - D\Delta t + \Delta t \frac{\partial}{\partial \xi} A_1 + \Delta t \frac{\partial}{\partial \eta} B - \Delta t \frac{\partial}{\partial \eta} R_v \frac{\partial}{\partial \eta} B_v) \Delta Q$$

$$= -\Delta t(\frac{\partial E_1}{\partial \xi} + \frac{\partial F}{\partial \eta} - H - \frac{\partial F_v}{\partial \eta}) \qquad (37)$$

where $\Delta Q = \hat{Q}^{n+1} - \hat{Q}^n$. In the limit as time goes to infinity and ΔQ goes to zero, Eqn. 37 approaches the parabolized, steady solution we wish to obtain.

The spatial discretization of Eqn. 37 is chosen as centered in η and upwind in ξ. This choice is in keeping with traditional space-marching procedures. For the calculations reported in the present report, the ξ-differencing was taken as first-order accurate. Extensions to second-order accurate can be made with no difficulty.

The use of the time-dependent terms causes the discretized form of the ξ-derivatives to be slightly different than that used in typical space-marching PNS codes. Consequently, we specify the ξ discretization explicitly here. The central differencing in η is identical to that used in most PNS procedures and is only indicated. Using the subscript i for the new ξ-location and i-1 for the old location, and writing all ΔQ quantities evaluated at the new

46

location on the left-hand side and all other quantities on the right-hand side, we obtain:

$$(I - D\Delta t + \frac{\Delta t}{\Delta \xi}A_{1i} + \Delta t\frac{\partial}{\partial \eta}B_i - \Delta t\frac{\partial}{\partial \eta}R_{vi}\frac{\partial}{\partial \eta}B_{vi})\Delta Q_i$$

$$= -\frac{\Delta t}{\Delta \xi}(\hat{F}_i^n - \hat{F}_{i-1}^{n+1}) - \Delta t(\frac{\partial \hat{E}_1}{\partial \xi} - \hat{H} - \frac{\partial}{\partial \eta}\hat{F}_v)_i^n \qquad (38)$$

This equation is iterated in time at each ξ station until convergence is reached before going on the next ξ-location.

The difference between the ξ-discretization in the time-marching PNS procedure as compared to the space-marching procedure can now be pointed out. In the space-marching procedure, iterations are not performed at each station. Therefore, in the discretization of $\partial F_1/\partial \xi$, the Jacobian A must be evaluated at the previous ξ-location,

$$\frac{\partial \hat{F}}{\partial \xi} = \frac{\partial}{\partial \xi} A\hat{Q} = \frac{1}{\Delta \xi} A_{i-1}(\hat{Q}_i - \hat{Q}_{i-1}) \qquad (38a)$$

Because the time-marching procedure includes (requires) iteration, this term can more appropriately be differenced as,

$$\frac{\partial \hat{F}_v}{\partial \xi} = \frac{1}{\Delta \xi}(A_i\hat{Q}_i - A_{i-1}\hat{Q}_{i-1}) \qquad (39)$$

The primary limitation on the previous expression is that it does not conserve mass when $\Delta \xi$ is a variable. The form in Eqn. 39 is conservative and allows the $\Delta \xi$ step size to be increased as the solution proceeds through the nozzle.

Upon discretizing in η, Eqn. 38 forms a block tridiagonal matrix for ΔQ_i. This matrix is easily solved by standard

47

techniques. For the solutions presented here, the time iteration
was continued until ΔQ reached machine accuracy, and then the
procedure was advanced to the next ξ-location. This very tight
tolerance required about 40 iterations per ξ-location. Sufficient
accuracy was generally obtained after 10 iterations ($\Delta Q = 10^{-5}$) but
this tighter tolerance was used to be conservative.

COMPUTED RESULTS

The present chapter presents the predicted pressure and heat transfer loadings on the solar collector. The Section is divided up into parts detailing the geometry and flowfield conditions of interest, nozzle flowfield predictions, nearfield and farfield plume predictions and mirror loadings.

GEOMETRIC AND THERMODYNAMIC CONDITIONS AND CASE IDENTIFICATION

The mirror geometry used for the present calculations is shown in non-dimensional form in Fig. 9. Here, the mirror size is normalized by the nozzle throat radius indicating that the physical size of the mirror scales linearly with the geometric size of the nozzle. When the level of pressure in the chamber is changed, however, the nozzle throat size changes accordingly. Thus, although the physical size of the collector for a given thrust size is independent of the chamber pressure, its non-dimensional size is different (because r^* changes). For this reason, two non-dimensional mirror sizes are shown. Figure 9a shows the mirror for a 50 psia chamber pressure, while Fig. 9b is for a 100 psia chamber pressure.

In order to estimate the severity of plume-mirror interaction over a range of conditions, a multi-dimensional test matrix composed of five different nozzle thrust sizes, three different expansion area ratios, and two different absorption chamber stagnation pressures was used. Calculations of plume-mirror interactions were made for each element in the matrix for an 80%
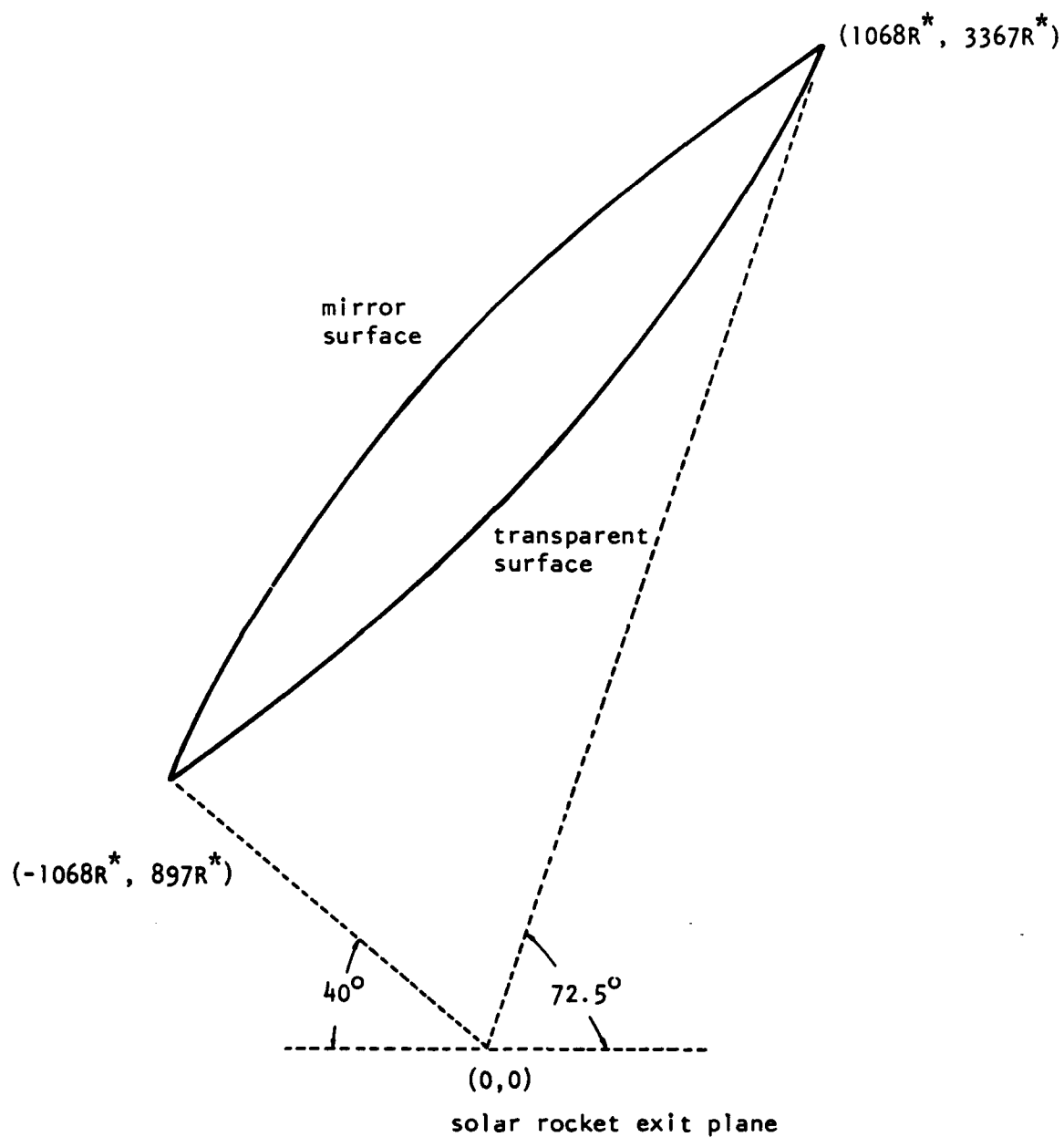
49

$(1068R^*, 3367R^*)$

mirror
surface

transparent
surface

$(-1068R^*, 897R^*)$

40°

72.5^o

$(0,0)$

solar rocket exit plane

Fig. 9a.   Configuration of solar concentrator for solar
rockets with P_o = 50 psia, T_o = 5000R, dimensions
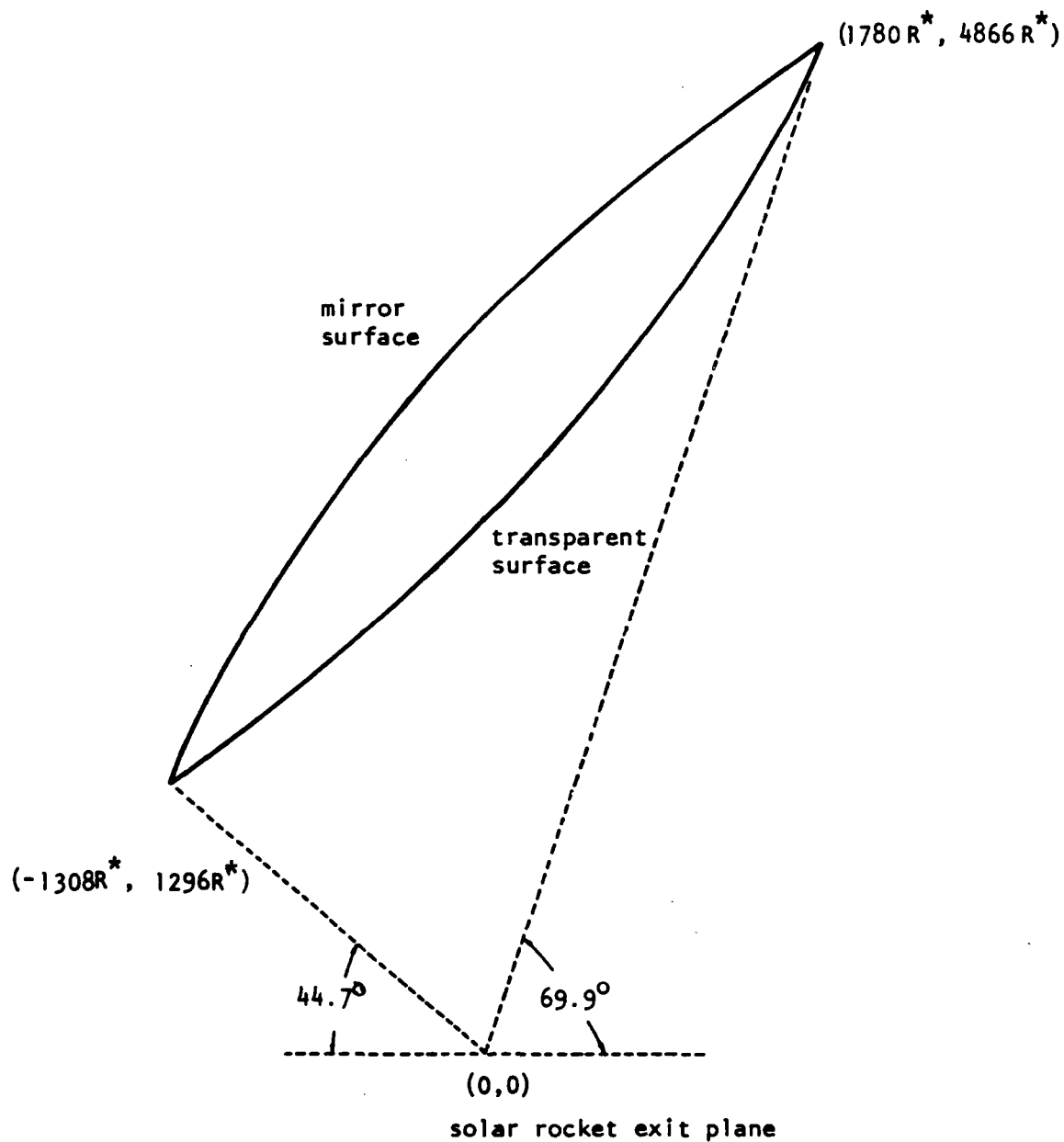are normalized by throat radius R^*

Fig. 9b. Configuration of solar concentrator for solar rockets with P_o = 100 psia, T_o = 5000R, dimensions are normalized by throat radius R^*

bell-shaped nozzle and for the corner elements in the matrix for a straight-walled conical nozzle. The thrust sizes considered were 1, 10, 50, 100 and 500 lb$_f$. The three expansion ratios were 100:1, 200:1, and 500:1. Stagnation pressure levels of 50 and 100 psia were considered. For all calculations a chamber stagnation temperature of 5000R was assumed and a "reasonable" wall temperature of 1600R was used. The effect of changes in wall temperature can be estimated from the results in Computational Procedures. Although dissociation begins to become important in hydrogen at temperatures slightly below 5000R, all calculations are based upon the assumptions of constant specific heats with a specific heat ratio, γ, of 1.4.

For ease in referring to the various cases in the test matrix, we have introduced the notation given in Tables 4 and 5. In these Tables, all cases are identified by three alphanumeric characters. The first of the three characters will be a "B" or "C" corresponding to bell-shaped and conical nozzles, respectively. The second character indicates both the area ratio and the chamber pressure. The digits 1, 2 and 3 correspond to area ratios of 100, 200 and 500 for the 50 psia case, while 4, 5 and 6 correspond to the same area ratios at the 100 psia case. The third digit signifies the thrust level with a one signifying the largest (500 lb$_f$) nozzle and a five signifying the smallest (1 lb$_f$) nozzle. The case identification for each bell-shaped nozzle is given in Table 4. The eight cases run for the conical nozzle are given in Table 5.

TABLE 4. TEST MATRIX AND CASE IDENTIFICATION FOR BELL-SHAPED NOZZLES

Case Identification	Chamber Pressure (psia)					
	50			100		
Thrust	Area Ratio					
Level (lb$_f$)	100:1	200:1	500:1	100:1	200:1	500:1
500	B11	B21	B31	B41	B51	B61
100	B12	B22	B32	B42	B52	B62
50	B13	B23	B33	B43	B53	B63
10	B14	B24	B34	B44	B54	B64
1	B15	B25	B35	B45	B55	B65
Case Group	B1	B2	B3	B4	B5	B6

Chamber Temperature = 5000 R
Bell-Shaped Nozzle (B)

TABLE 5. TEST MATRIX AND CASE IDENTIFICATION FOR CONICAL NOZZLES

Case Identification Thrust Level (lb$_f$)	Chamber Pressure (psia)					
	50			100		
	Area Ratio					
	100:1	200:1	500:1	100:1	200:1	500:1
500	C11	---	C31	C41	---	C61
100	---	---	---	---	---	---
50	---	---	---	---	---	---
10	---	---	---	---	---	---
1	C15	---	C35	C45	---	C65
Case Group	C1	---	C3	C4	---	C6

Chamber Temperature = 5000 R
Conical-Shaped Nozzle (C)

Once the thrust sizes, pressure levels, area ratios and nozzle shapes have been defined, it remains to determine the physical dimensions of the nozzles. For the present series of calculations, the nozzle throat radii were determined from the above thermodynamic and geometric data on the basis of an ideal one-dimensional calculation of the stream thrust for expansion into a vacuum. A simple computer code was written to take these input geometric quantities and compute a corresponding nozzle throat radius for each condition of interest. The results of these one-dimensional calculations are shown in Table 6. This Table lists the specific impulse, the nozzle mass flow rate and the

nozzle throat radius (as determined from one-dimensional approximations) for each thrust size and stagnation pressure. Because the one-dimensional results are independent of nozzle geometry, the throat radius for the bell-shaped and conical nozzles are the same. Therefore, the case identification (see Table 5) contains only the two numerical digits. All calculations are for a stagnation temperature of 5000R.

TABLE 6. ONE-DIMENSIONAL ESTIMATES OF
NOZZLE FLOWS
For both Bell-Shaped and Conical Nozzles
T_o = 5000 R

Case	P_o (psia)	Thrust (lb_f)	Specific Impulse (sec)	Mass Flow Rate (lbm/s)	Throat Radius (inches)
11		500		.56681	1.3487
12		100		.11346	0.6032
13	50	50	882.13	.05668	.4265
14		10		.01134	.1907
15		1		.00113	.0603
21		500		.56188	1.3429
22		100		.11238	0.6005
23	50	50	889.87	.05619	.4246
24		10		.01124	.1899
25		1		.00112	.0601
31		500		.55730	1.3374
32		100		.11146	0.5981
33	50	50	897.18	.05573	.4229
34		10		.01146	.1891
35		1		.00115	.0598
41		500		0.56681	0.9537
42		100		.11336	.4265
43	100	50	882.13	.05668	.3016
44		10		.01134	.1349
45		1		.00113	.0427
51		500		0.56188	0.9495
52		100		.11238	.4246
53	100	50	889.87	.05619	.3003
54		10		.01124	.1343
55		1		.00112	.0425
61		500		0.55730	0.9457
62		100		.11146	.4229
63	100	50	897.18	.05573	.2990
64		10		.01115	.1337
65		1		.00111	.0423

NOZZLE FLOWFIELD CALCULATIONS

Details of the Computations

The two basic nozzle geometries are shown on Figs. 10 and 11 along with the grid used for the PNS solutions. Figure 10 is for the bell-shaped nozzle while Fig. 11 is for the conical nozzle. Note in both cases that the grid is more closely refined near the wall to resolve the steep gradients in the boundary layer. There is also a weak stretching in the axial direction to give slightly better resolution near the throat. Both nozzles are for the 200:1 area ratio, and both have grids that are 150 (axial) x 80 (radial). A few of the calculations were done on a 120 x 60 grid but this should not affect the numerical results. The philosophy used in picking the 150 x 80 grid was to obtain a grid that was sufficiently well refined that all thrust sizes (all nozzle Reynolds numbers) could be computed on the same grid without necessitating grid changes.

A very important consideration in any numerical calculation is the degree to which global mass conservation is enforced. During the calculations, this easily verifiable conservation law was checked periodically to ensure that adequate conservation was realized. Figure 12 shows the results of a typical check. Specific conditions for this calculation are given in the Figure. The results on Fig. 12 show the net mass flux crossing each plane of the nozzle from the throat to the exit plane. As can be seen, the mass flow is not strictly constant, but shows a slight increase from the throat to the nozzle exit. Overall, the net mass gain is
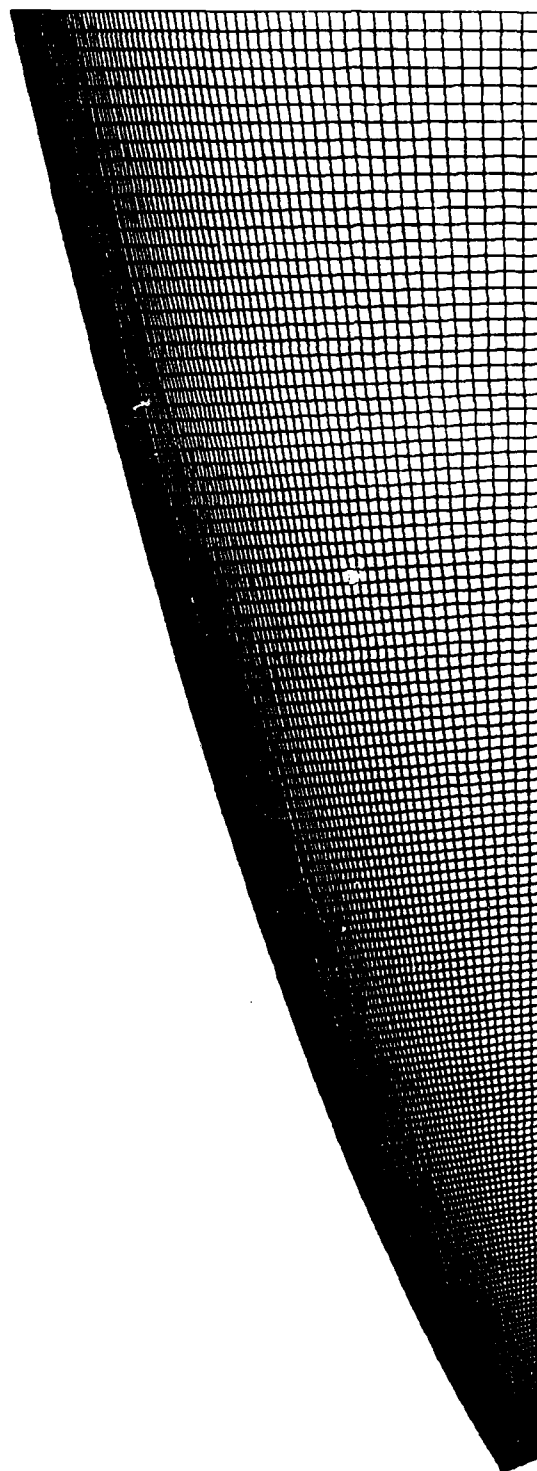
Fig. 10. Geometric shape and nominal grid used for bell-shaped calculations, grid size 150 x 80.
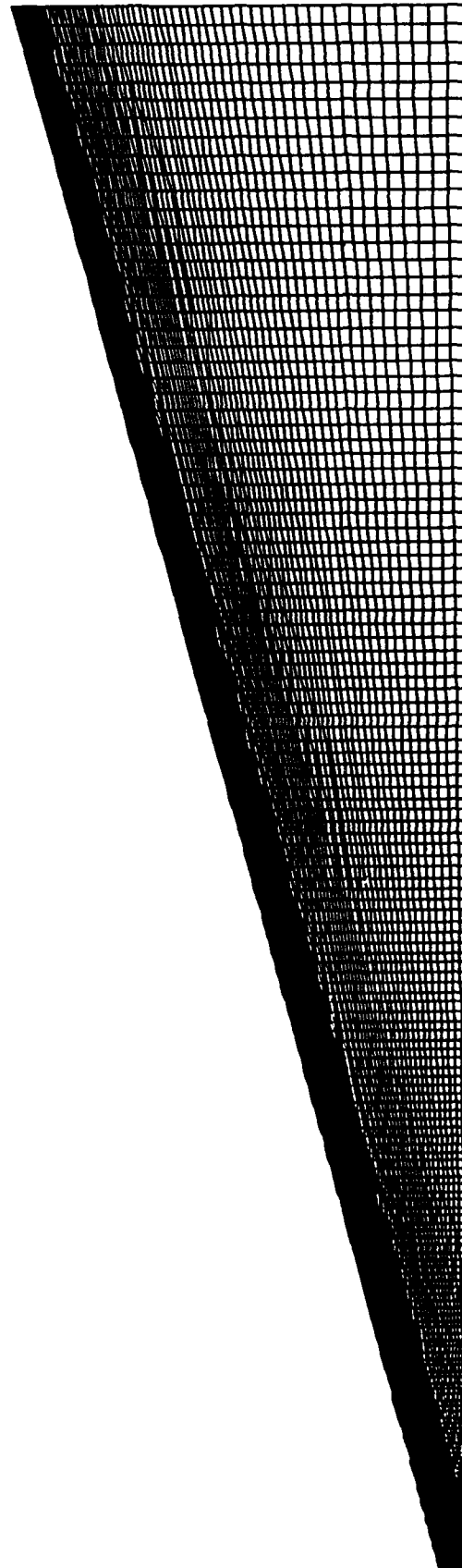
Fig. 11. Geometric shape and nominal grid used for Conical Nozzle calculations, grid size 150 x 80
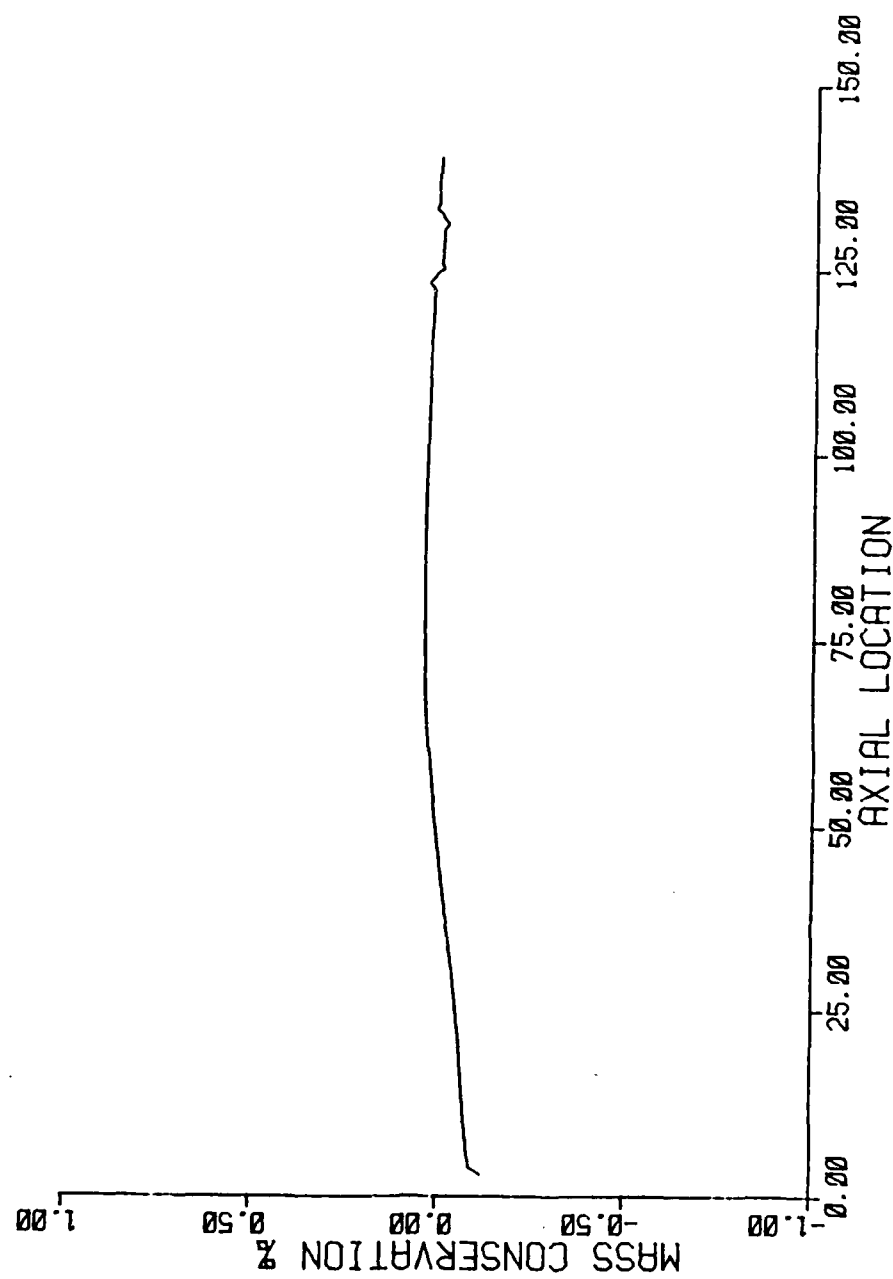
Fig. 12. Typical mass conservation along the nozzle axis of PNS solution. (Bell-shaped nozzle, area ratio = 100:1, P_0=50 psia, T_0=5000 R, thrust = 500 lbf)

less than 0.1%. This is considered to be very good. Recall that typical boundary layer-displacement thickness calculations violate mass flow by the amount of mass entrainment into the boundary layer even when the inviscid calculation conserves mass identically. Thus, the present mass error is no worse than that in a nozzle whose exit boundary layer displacement thickness is 0.05% of the exit radius. Also, our experience with TD2 in CONTAM showed that this MOC code generates larger mass flow errors than the PNS code.

Also of interest in the PNS procedure is the number of iterations required at each axial location. An indication of this is given on Fig. 13. Here we show the L_2-norm values of $\Delta Q/Q$ for seven different locations. Two aspects should be noted. First, all calculations took about 40 iterations to converge. This was typical of all nozzles and all x-locations. This convergence was obtained with CFL's of from 50 to 80 as shown in the Figure. Second, the iterations were carried to very tight tolerances corresponding to machine accuracy in double-precision (64 bit). This accuracy is not necessary. Convergence down to about 10^{-6} (instead of 10^{-14}) would have given nominally the same results and have reduced the iterations from 40 to 10. Nevertheless, extensive experience shows that there is always a little improvement in the solutions when they are converged very tightly, and as in the grid choice we opted for a "safe", although slightly more, CPU-intensive approach.

As the last two diagnostic results before delving into the solutions, we show some characteristics of the turbulence in the nozzle in Figs. 14 and 15. Figure 14 shows the ratio of turbulent

$$CFL = \frac{\Delta t}{\Delta n} \ max \ (\nabla + \sqrt{{n_x}^2 + {n_y}^2} \ c)$$

$$CFL = 50 \sim 80$$
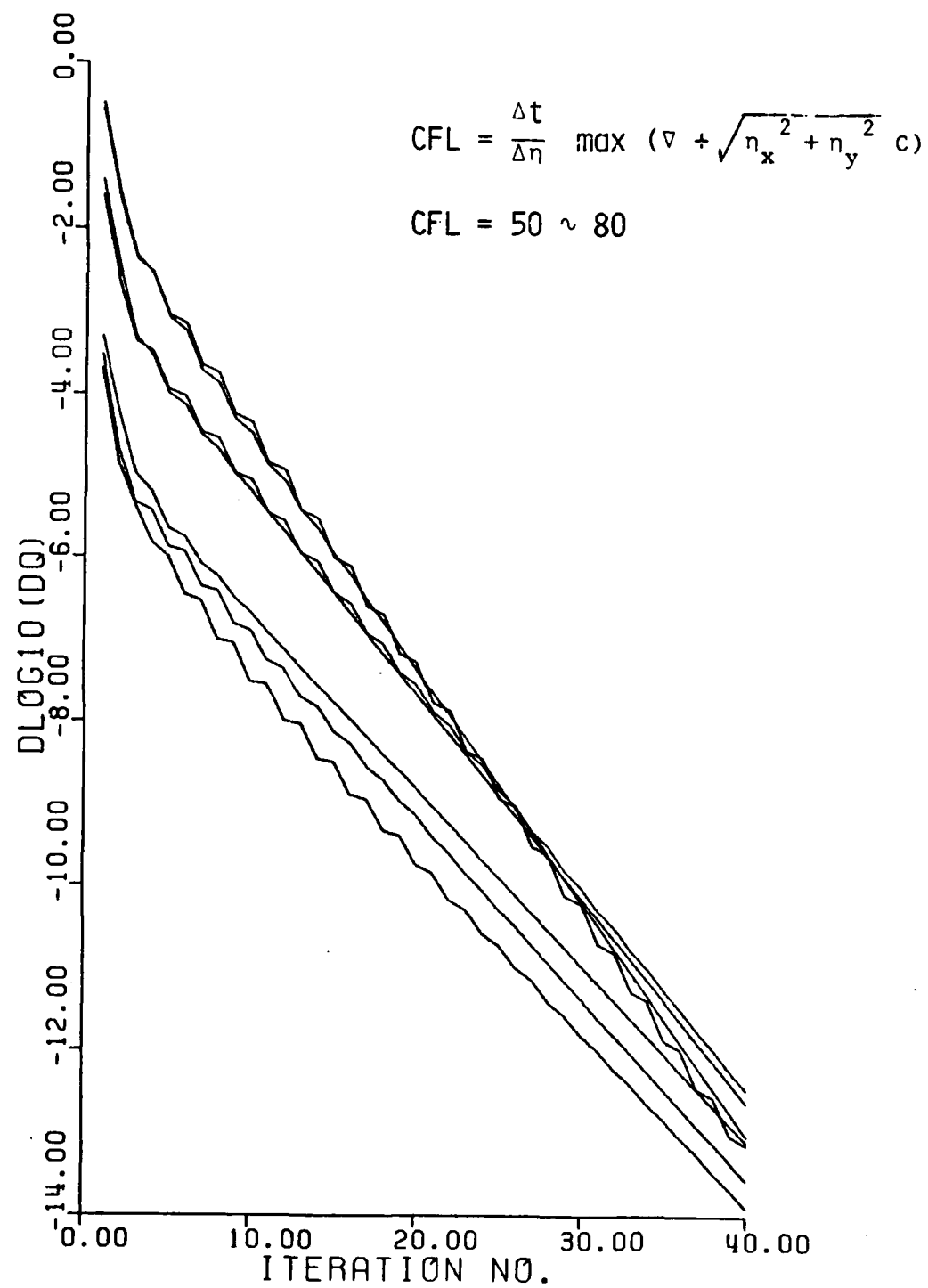
Fig. 13. Representative convergence rates of PNS code at seven specific locations.

61

BELL-SHAPED NOZZLE, 500 lb_f

P_0 = 50 psia, T_0 = 5000 R

X = 25R*

max $(\frac{\mu_t}{\mu}) \leq 14$, LAMINAR

Y+ *10^1

TUR U/LAMINAR U
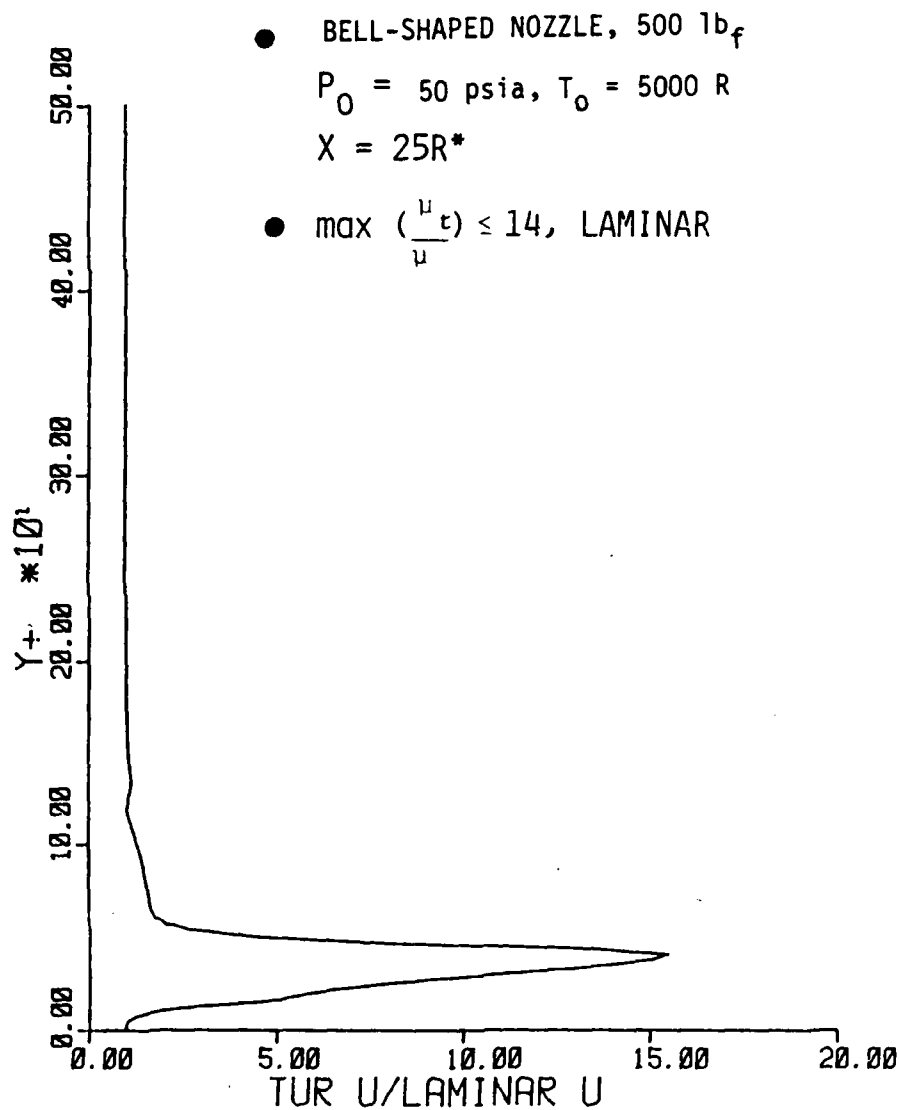
Fig. 14. Ratio of eddy viscosity to molecular viscosity as a function of distance from the wall (measured in y+ units). Baldwin-Lomax algebraic turbulence model.
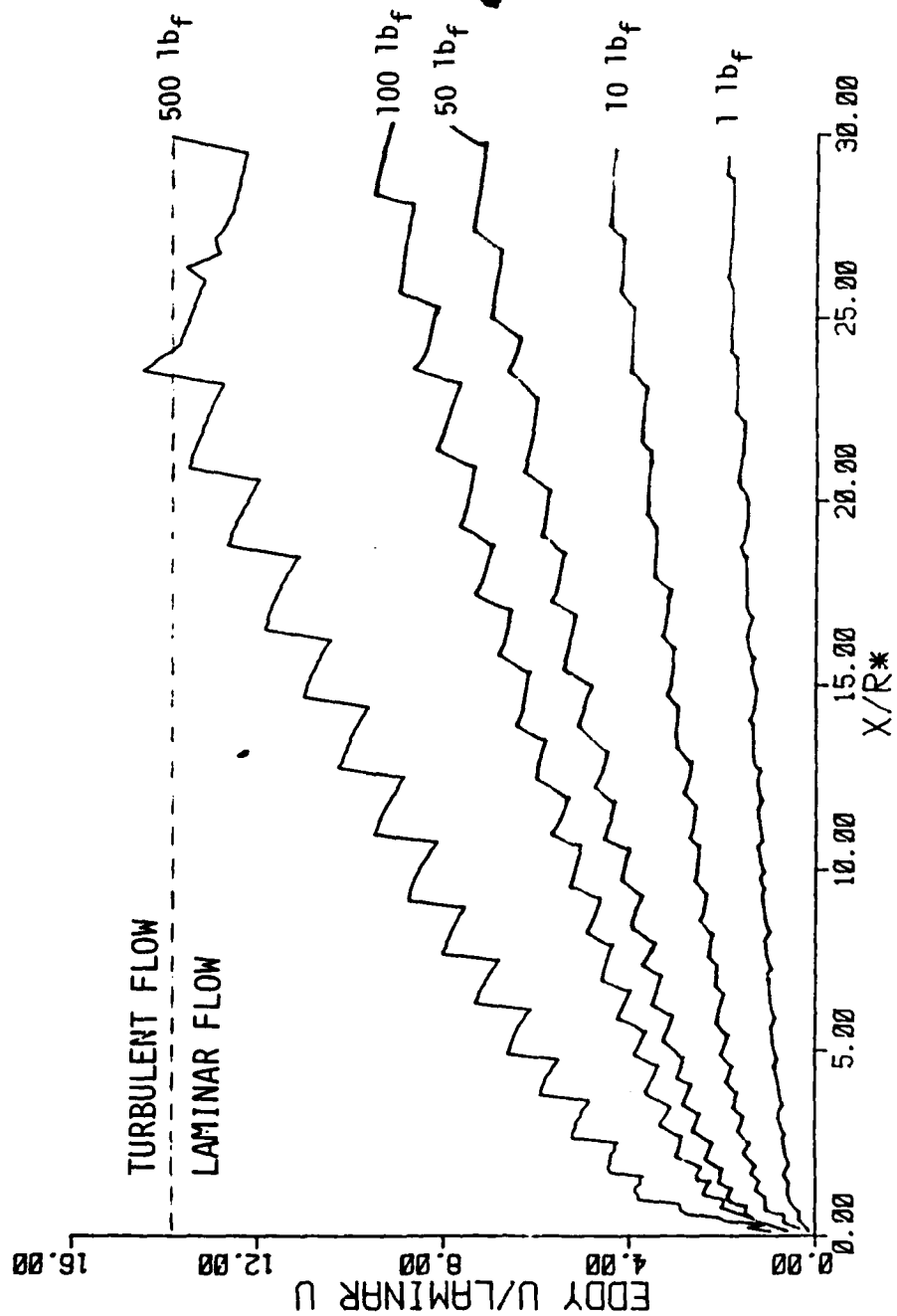
Fig. 15. Maximum eddy viscosity in boundary layer as a function of distance along the nozzle axis. Case Group 1 (bell-shaped, area ratio 100:1, $P_o = 50$ psia, $T_o = 5000$ R)

63

diffusivity to laminar diffusivity across the boundary layer. As can be seen, the curve shows the characteristic peak near the wall followed by a decrease to unity outside the shear layer. What is not characteristic of a traditional boundary layer is the maximum value of about 15 for μ_t/μ. This extremely low value of μ_t/μ was representative of all calculations. The strong favorable pressure gradient and the relatively low Reynolds numbers made it impossible to reach higher μ_t/μ values. A more general picture of $(\mu_t/\mu)_{max}$ is given on Fig. 15 for all five thrust levels and at all x-locations. Note that throughout most of the test matrix, the value of μ_t/μ is less than 15.

Even though the Baldwin-Lomax model suggests the boundary layer Reynolds numbers are too low to support turbulence, the turbulence model was left "on" in all calculations. The philosophy was that even this small amount of "turbulence" would increase the boundary layer growth somewhat and would lead to a more conservative estimate of plume/mirror impingement (i.e., overpredict impingement). Of course, it must be remembered that the Baldwin-Lomax model is not expected to be able to predict the onset of transition in a rocket nozzle very reliably, but it is probably as good as any other turbulence model available. All other indications (such as Re_θ) also suggested laminar or near-laminar boundary layers, but it is possible that fully turbulent layers might be present.

Nozzle Solutions for Bell-Shaped Nozzle

The first nozzle flowfield results we show are the Mach number and pressure contours inside the bell-shaped nozzles. Figures 16a and b show the Mach number and pressure contours, respectively, for the five thrust sizes of the bell-shaped nozzle with a 100 to one area ratio and a chamber pressure of 50 psia. Looking first at Fig. 16a, we can clearly see the thickening of the boundary layer as the thrust size is decreased from 500 lb_f at the top to 1 lb_f at the bottom. This increase in the relative effect of the boundary layer is to be expected because of the small sizes and, hence, lower Reynolds numbers in the low thrust nozzles. Although the effects of the boundary layer are considerable here, the coupled boundary layer is somewhat thinner than in the uncoupled cases (boundary layer plus inviscid) discussed in Physical Description of the Flowfield.

The pressure contours for this same area ratio nozzle are given in Fig. 16b. Note that the total expansion obtained in the nozzle decreases slowly as the thrust size is decreased and the boundary layer grows thicker. Analogous conclusions can also be seen from the Mach number contours in Fig. 16a. Also note the pressure contours suggest the pressure gradient normal to the wall is zero. This is in agreement with boundary layer theory.

Corresponding Mach number and pressure contours for the 200:1 area ratio bell-shaped nozzle are shown in Figs. 17a and b, while those for the 500:1 area ratio are given in Figs. 18a and b. The variations with thrust size for these two larger area ratios are analogous to those observed for the lower area ratio case in Fig.
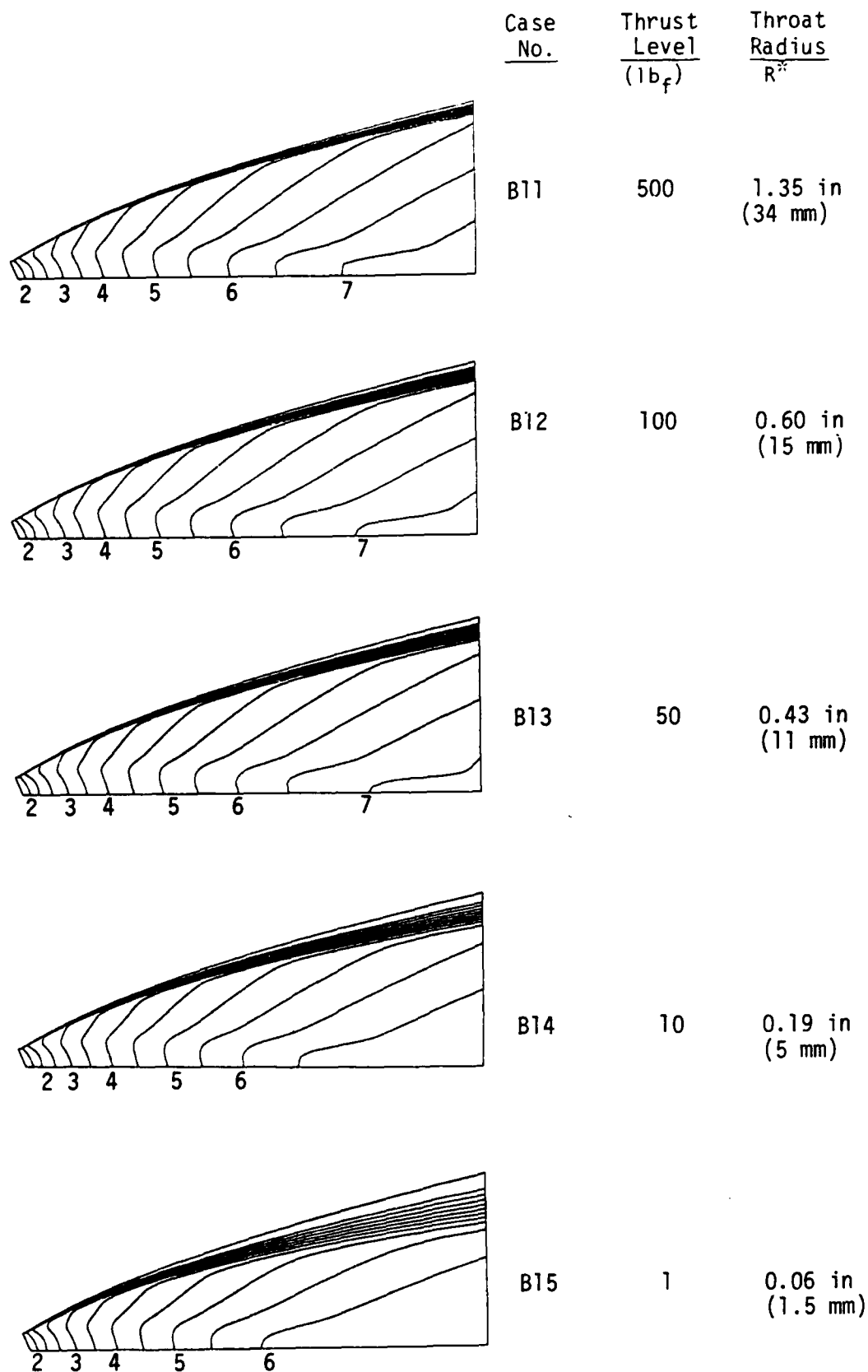
Case No.	Thrust Level (lb_f)	Throat Radius R^*
B11	500	1.35 in (34 mm)
B12	100	0.60 in (15 mm)
B13	50	0.43 in (11 mm)
B14	10	0.19 in (5 mm)
B15	1	0.06 in (1.5 mm)

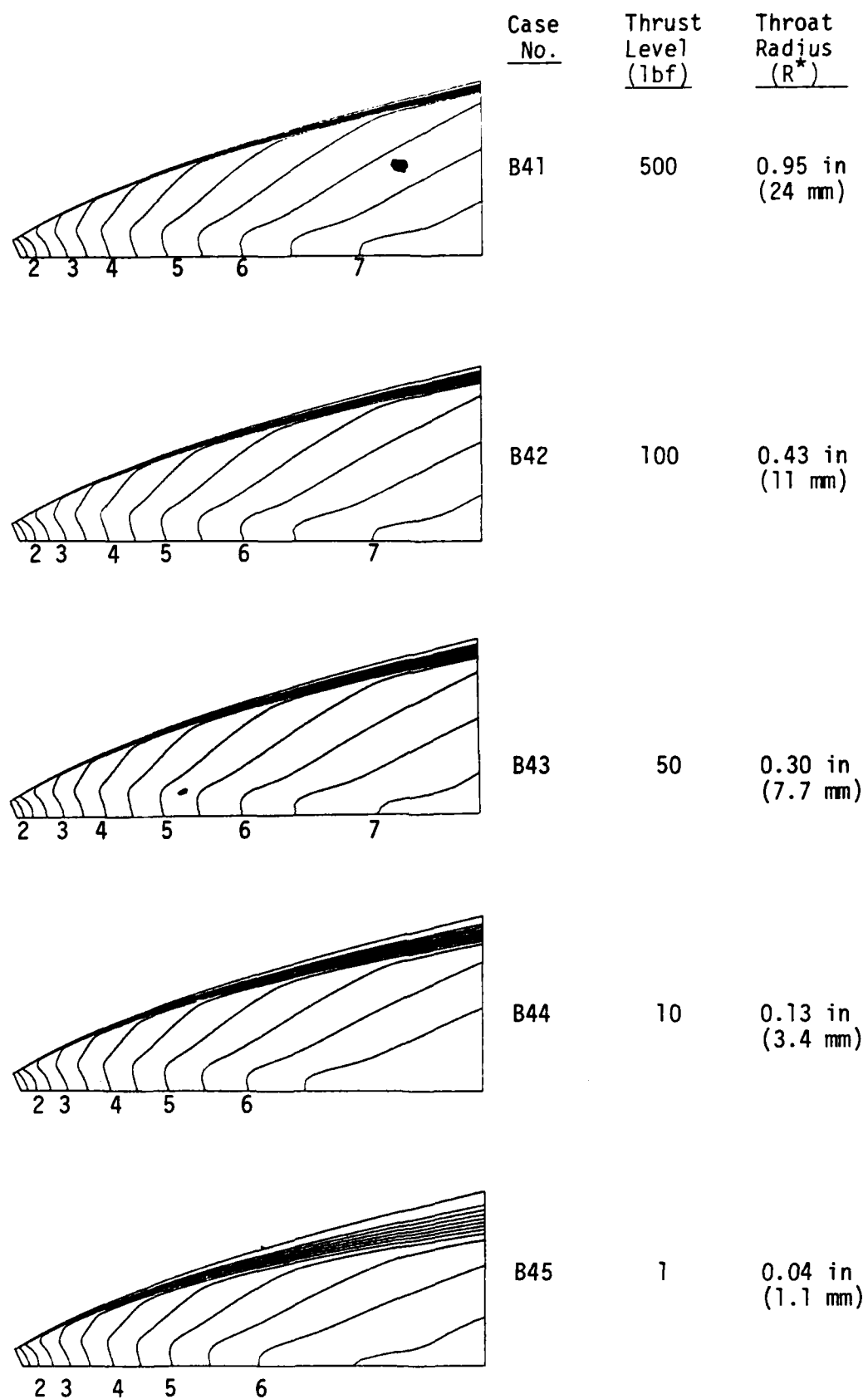Fig. 16a. Mach number contours for various thrust sizes in Case Group B1 (bell-shaped nozzle, area ratio 100:1, P_o=50 psia, T_o=5000 R)

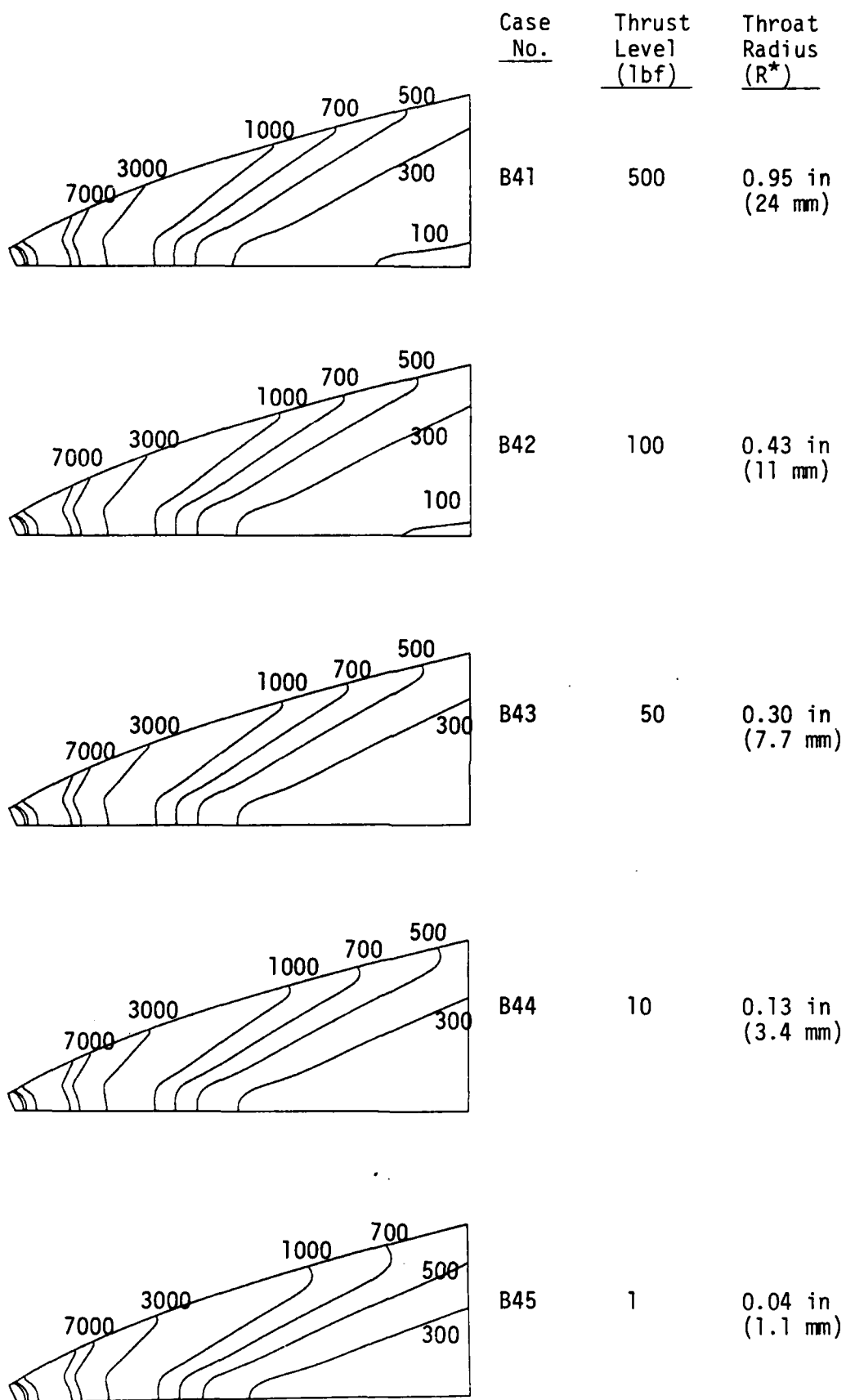| Case No.	Thrust Level (lbf)	Throat Radius (R^*)
B11	500	1.5 in (34 mm)
B12	100	0.60 in (15 mm)
B13	50	0.43 in (11 mm)
B14	10	0.19 in (5 mm)
B15	1	0.06 in (1.5 mm)

Fig. 16b. Pressure contours for various thrust sizes in Case Group B1 (bell-shaped nozzle, area ratio 100:1, P_o=50 psia, T_o=5000 R)

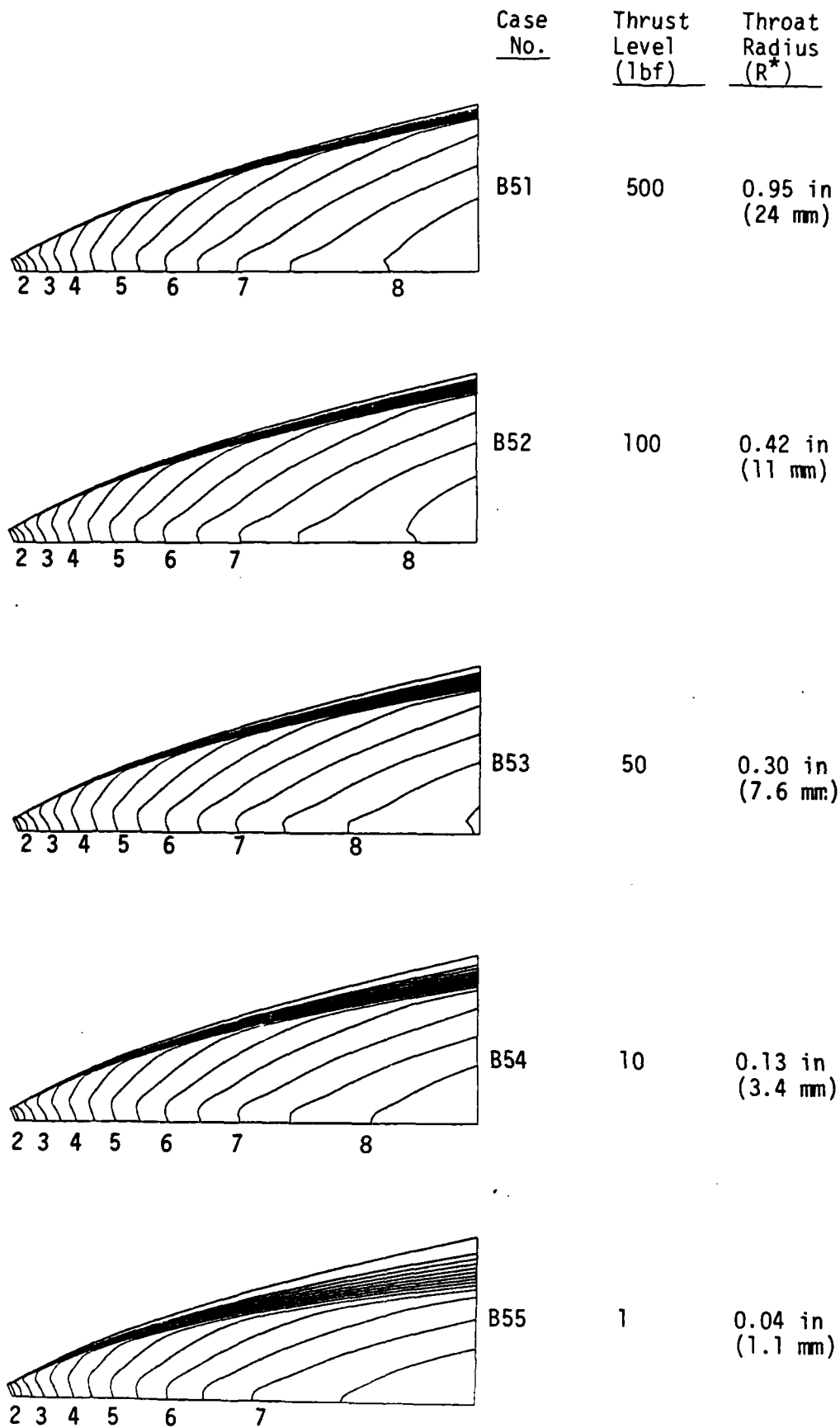| Case No.	Thrust Level (lbf)	Throat Radius (R*)
B21	500	1.34 in (34 mm)
B22	100	0.6 in (15 mm)
B23	50	0.42 in (10 mm)
B24	10	0.19 in (4.8 mm)
B25	1	0.06 in (1.5 mm)

Fig. 17a. Mach number contours for various thrust sizes in Case Group B2 (bell-shaped nozzle, area ratio 200:1, P_0=50 psia, T_0=5000 R)
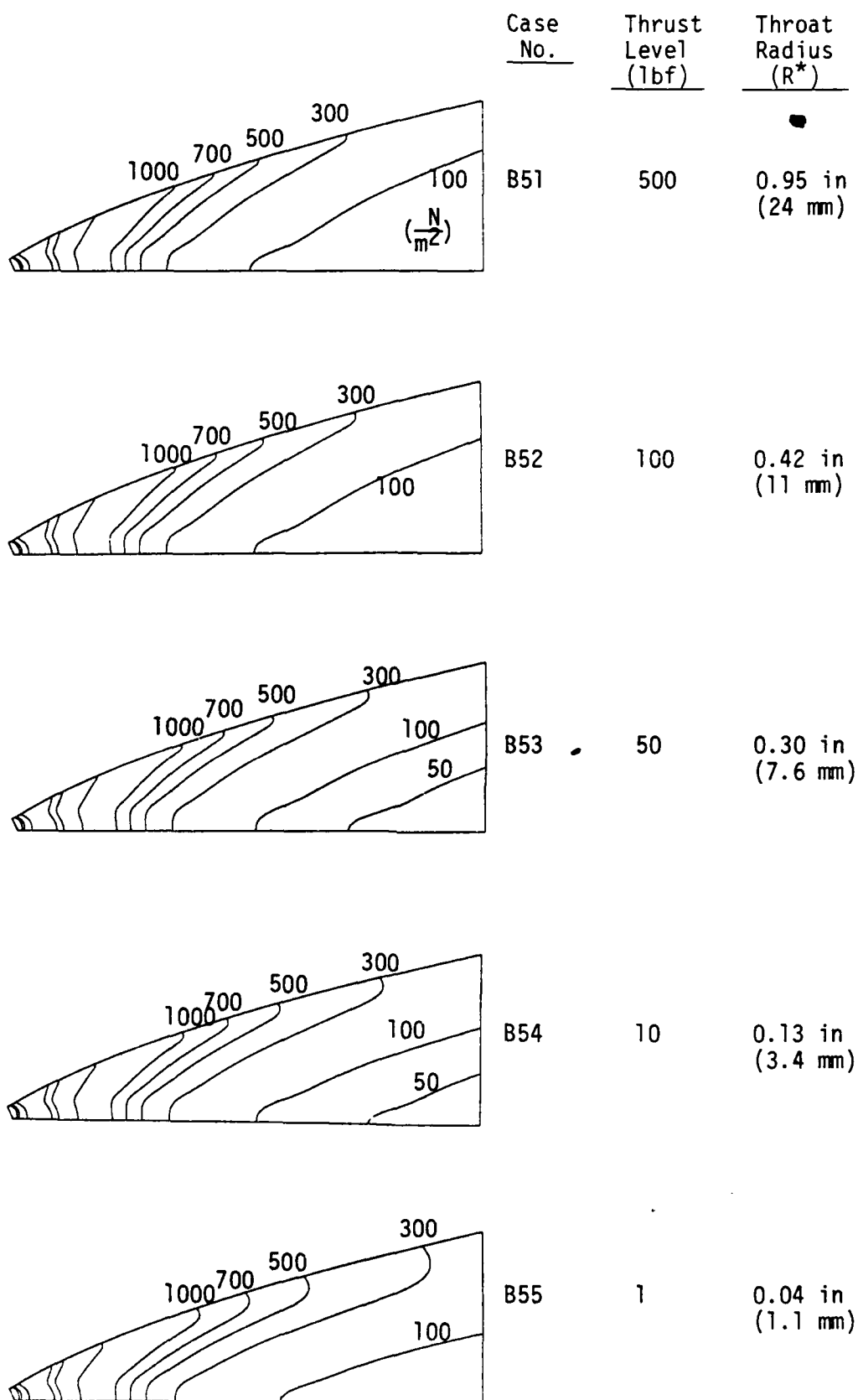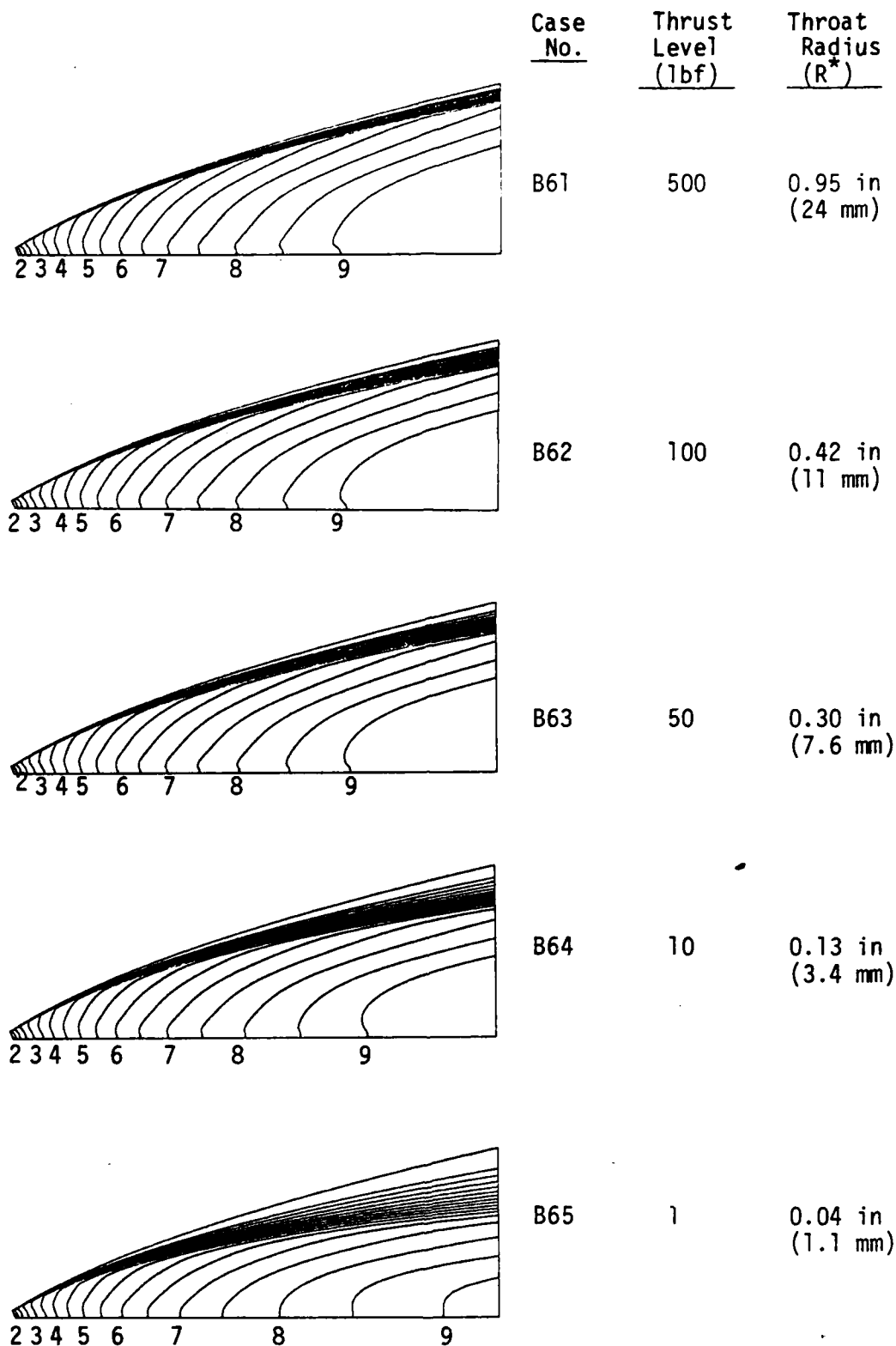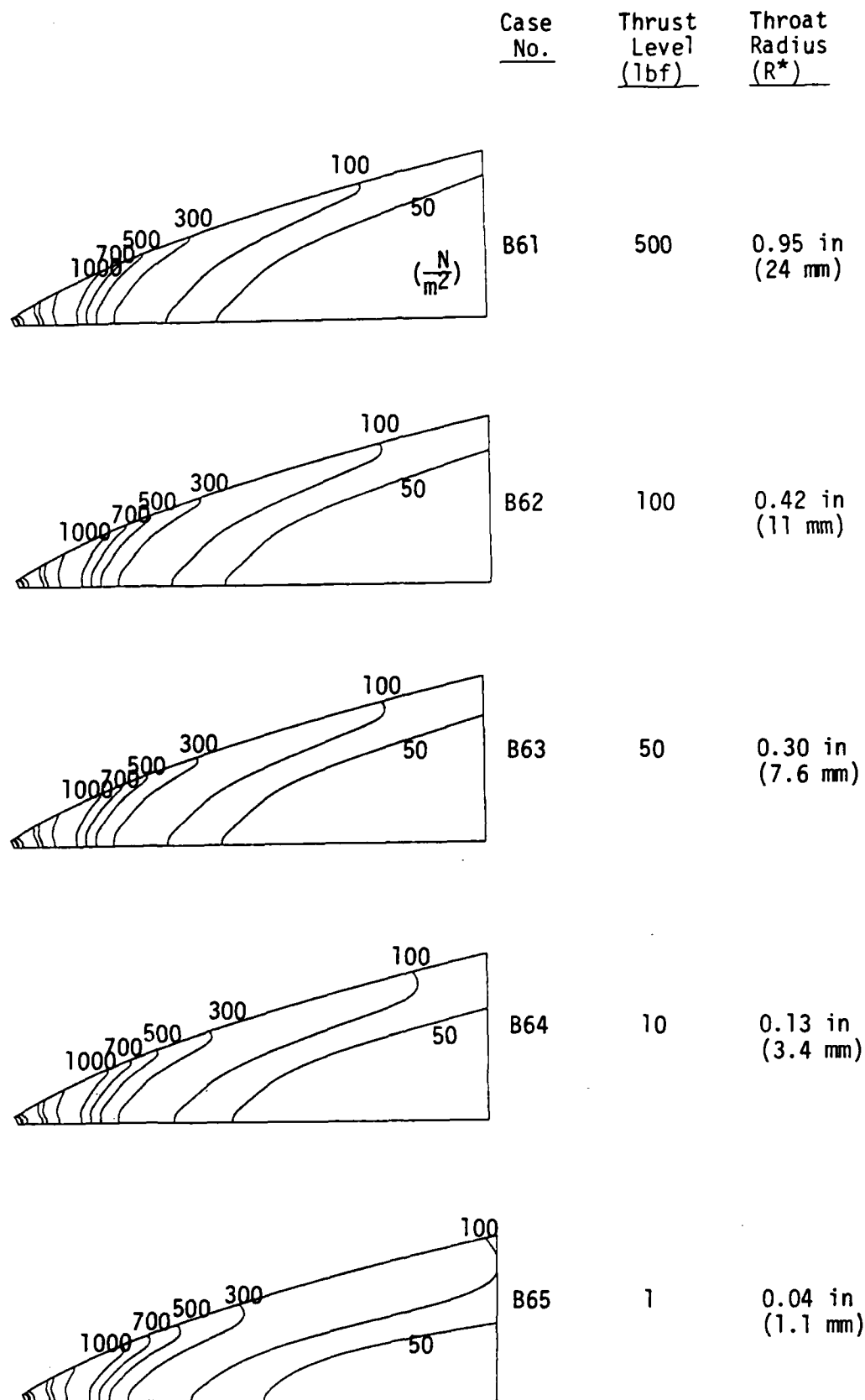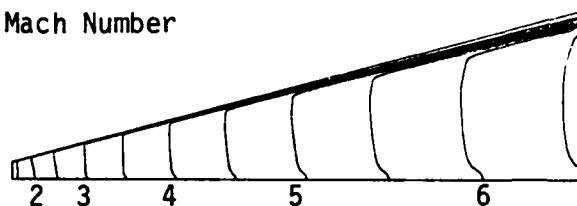
	Case No.	Thrust Level (lbf)	Throat Radius (R*)
	B21	500	1.34 in (34 mm)
	B22	100	0.6 in (15 mm)
	B23	50	0.42 in (10 mm)
	B24	10	0.19 in (4.8 mm)
	B25	1	0.06 in (1.5 mm)

Fig. 17b. <u>Pressure contours for various thrust sizes in Case Group B2</u> <u>(bell-shaped nozzle, area ratio 200:1, P_o=50 psia,</u> <u>T_o=5000 R)</u>

Case No.	Thrust Level (lbf)	Throat Radius (R*)
B31	500	1.34 in (34 mm)
B32	100	0.6 in (15 mm)
B33	50	0.42 in (11 mm)
B34	10	0.19 in (4.8 mm)
B35	1	0.06 in (1.5 mm)
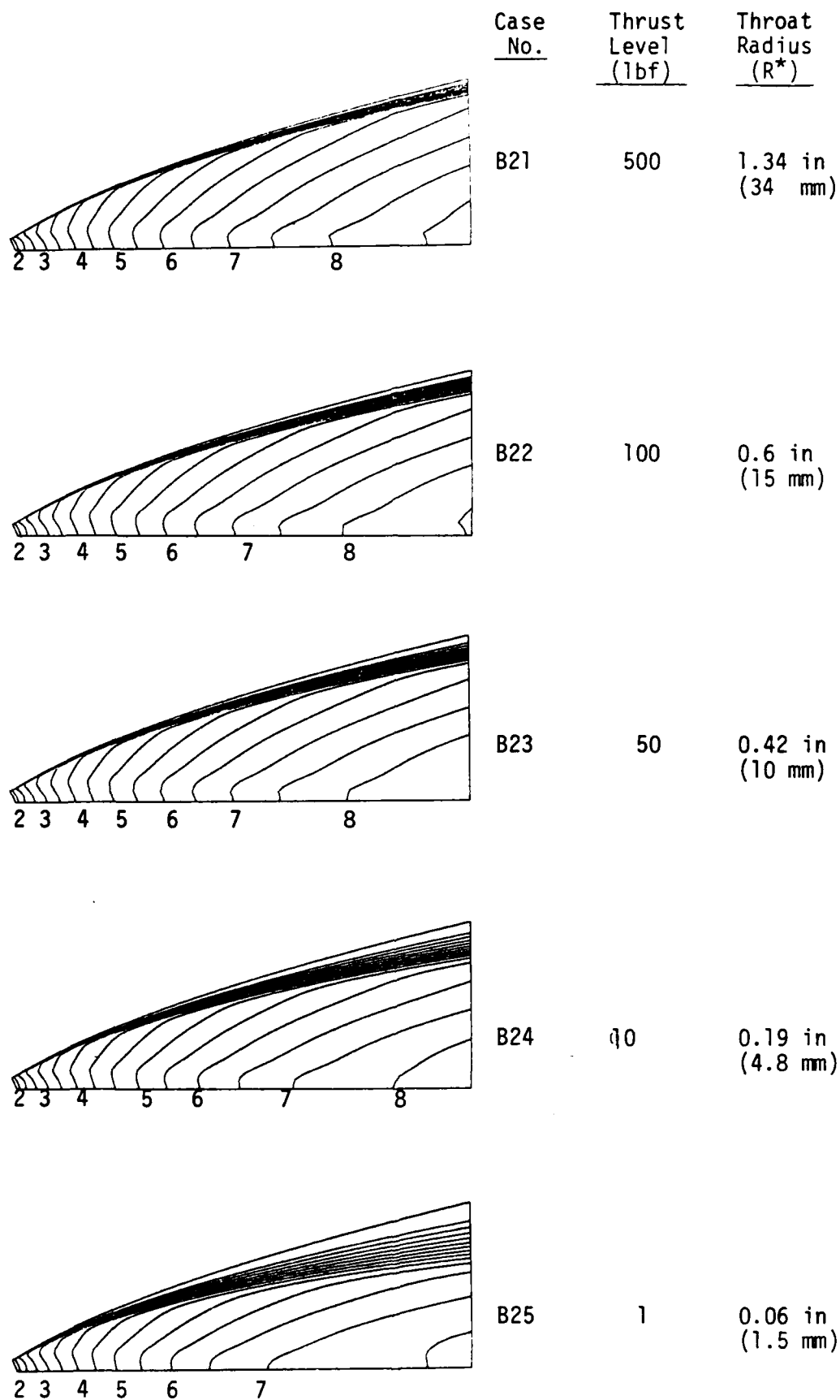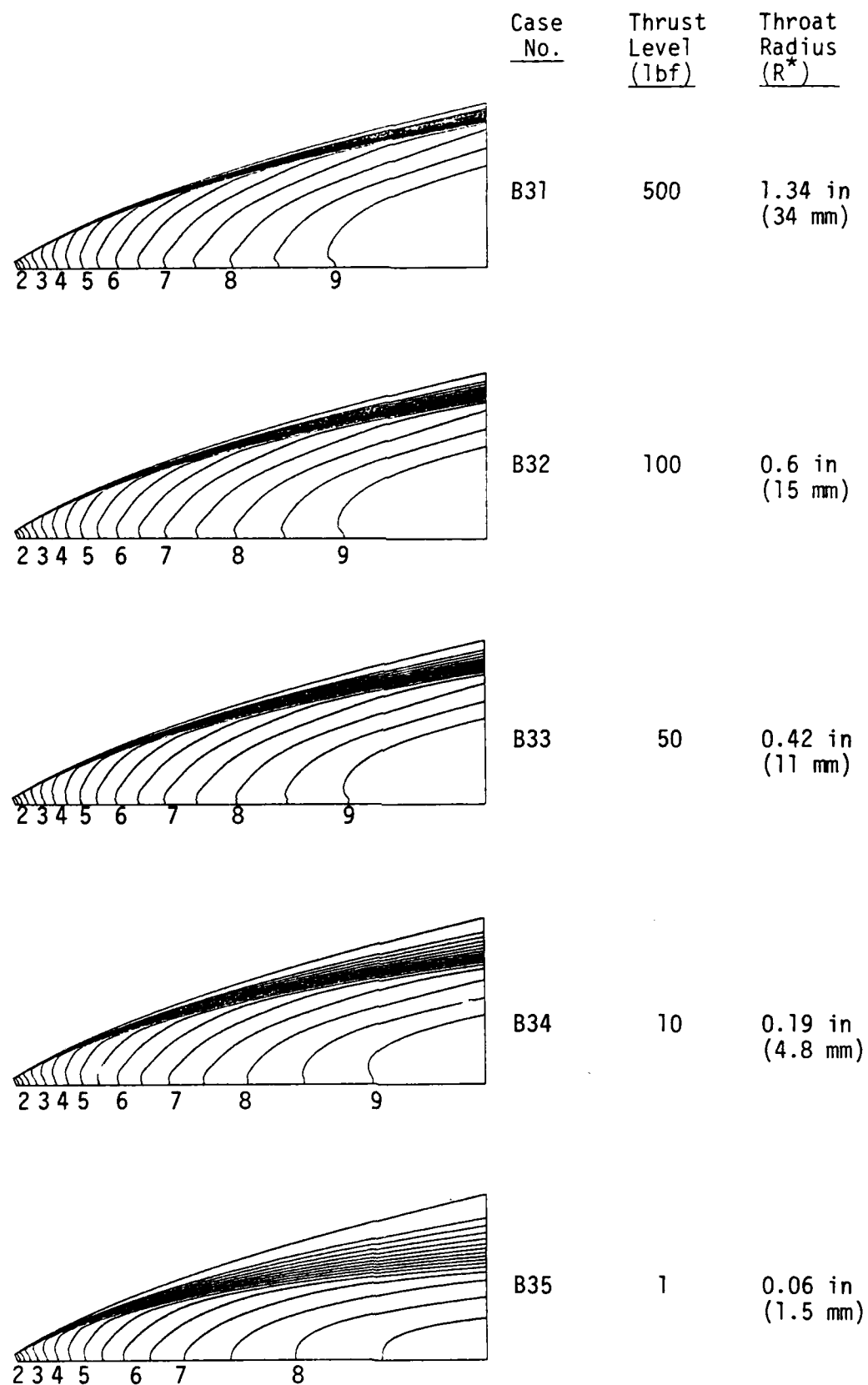
Fig. 18a. Mach number contours for thrust sizes in Case Group B3 (bell-shaped nozzle, area ratio 500:1, P_o = 50 psia, T_o = 5000 R)

| Case No.	Thrust Level (lbf)	Throat Radius (R*)
B31	500	1.34 in (34 mm)
B32	100	0.6 in (15 mm)
B33	50	0.42 in (11 mm)
B34	10	0.19 in (4.8 mm)
B35	1	0.06 in (1.5 mm)
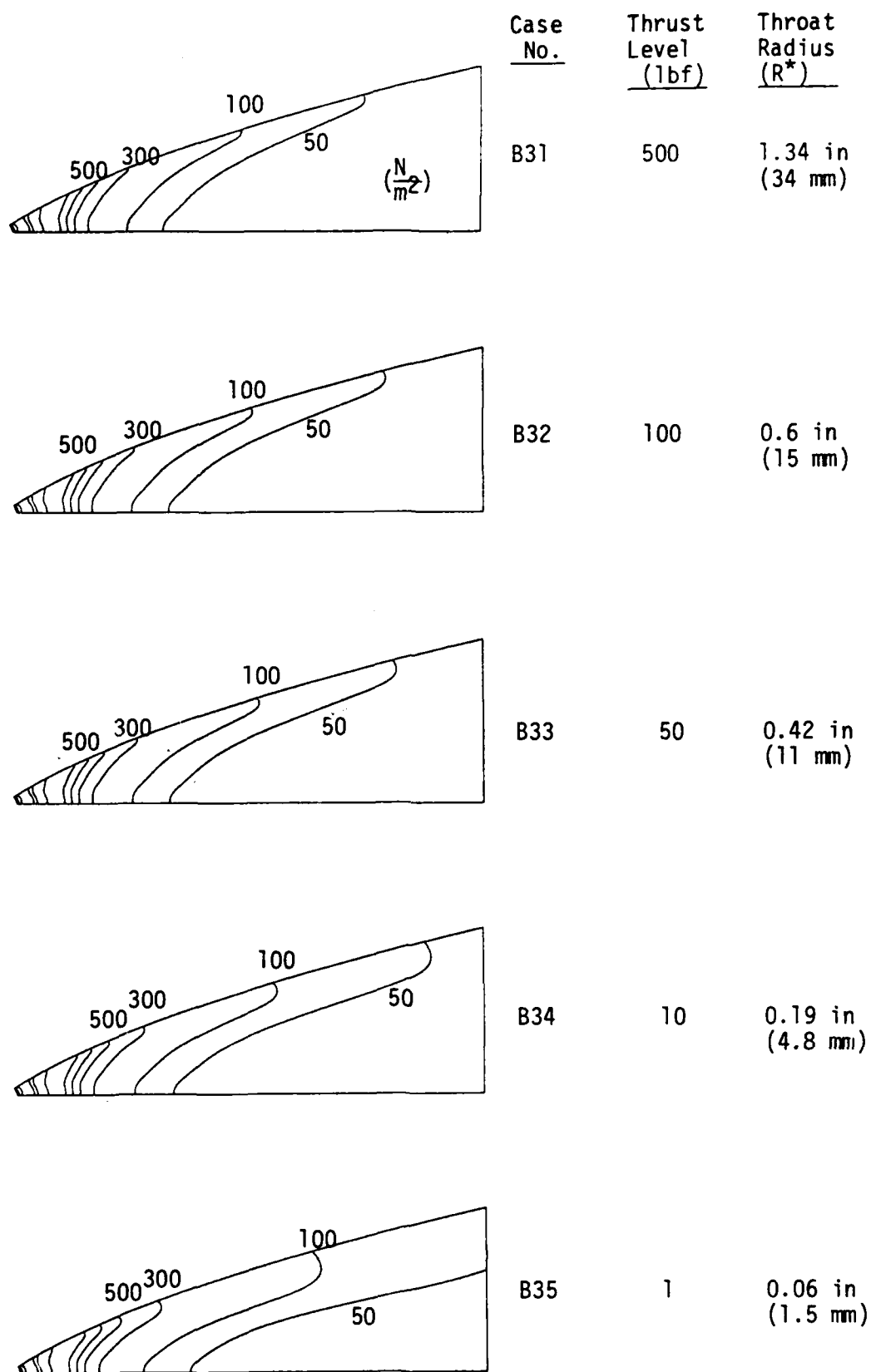
Fig. 18b. Pressure contours for thrust sizes in Case Group B3 (bell-shaped nozzle, area ratio 500:1, P_o=50 psia, T_o=5000 R)

16. Comparison of similar thrust size nozzles in Figs. 16, 17 and 18 shows a decided increase in boundary layer thickness for the larger area ratio nozzles. Thus, we would expect the larger nozzles to exhibit increased mass impingement on the mirrors as compared with the low area ratio nozzles. It is of interest to note that the 500:1 nozzle is about a factor of two longer than the 100:1 nozzle. For reference, the three bell-shaped nozzles are shown to scale for one thrust level in Fig. 19.

Corresponding results for a chamber pressure of 100 psia are given in Figs. 20 to 22. Figure 20a and b give the Mach number and pressure contours for a nozzle of area ratio 100:1. Figures 21a and b show similar results at an area ratio of 200:1 while Figs. 22a and b are for a 500:1 area ratio. The relative comparisons between these sets of results are analogous to those for the 50 psia case. Comparisons between the 100 psia calculations and the 50 psia calculations show the Mach number contours are nearly the same. The factor of two increase in Reynolds number is not large enough to affect the flow expansion significantly. The pressure contours, of course, show a change in level with the exit pressure in the 100 psia case being higher than in the 50 psia case. This pressure increase will continue all the way to the collector, but its effect is more than offset by the increased non-dimensional distance to the mirror in the higher chamber pressure case (compare Figs. 9a and 9b).

The final set of nozzle flowfield results are for the conical nozzles. These results are given on Figs. 23 to 26. Figure 23 is for an area ratio of 100:1 and 50 psia for the large (500 lbf) and
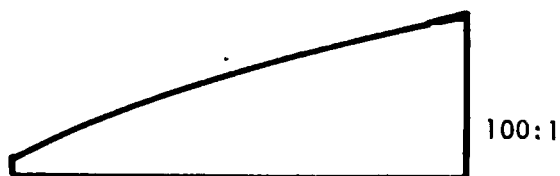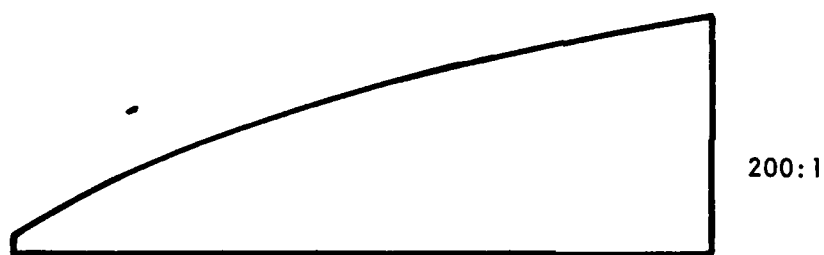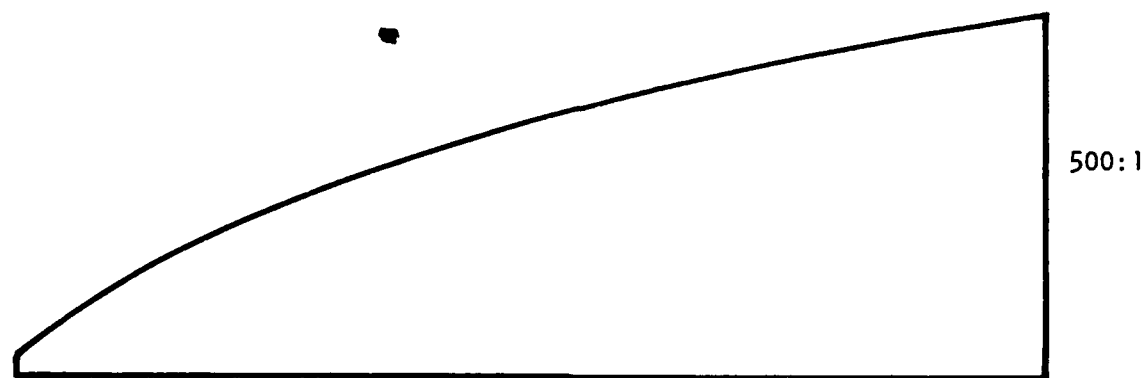
Fig. 19. Three bell-shaped nozzles with area ratios, 500:1, 200:1, and 100:1; for one thrust level

73

	Case No.	Thrust Level (lbf)	Throat Radius (R*)
	B41	500	0.95 in (24 mm)
	B42	100	0.43 in (11 mm)
	B43	50	0.30 in (7.7 mm)
	B44	10	0.13 in (3.4 mm)
	B45	1	0.04 in (1.1 mm)

Fig. 20a. Mach number contours for various thrust sizes in Case Group B4 (bell-shaped nozzle, area ratio 100:1, P_0=100 psia, T_0=5000 R) .

	Case No.	Thrust Level (lbf)	Throat Radius (R*)
	B41	500	0.95 in (24 mm)
	B42	100	0.43 in (11 mm)
	B43	50	0.30 in (7.7 mm)
	B44	10	0.13 in (3.4 mm)
	B45	1	0.04 in (1.1 mm)

Fig. 20b. Pressure contours for various thrust sizes in Case Group B4 (bell-shaped nozzle, area ratio 100:1, P_0=100 psia, T_0=5000 R)

75

Case No.	Thrust Level (lbf)	Throat Radius (R*)

B51   500   0.95 in (24 mm)

B52   100   0.42 in (11 mm)

B53   50   0.30 in (7.6 mm)

B54   10   0.13 in (3.4 mm)

B55   1   0.04 in (1.1 mm)

Fig. 21a. Mach number contours for various thrust sizes in Case Group B5 (bell-shaped nozzle, area ratio 200:1, P_0=100 psia, T_0=5000 R)

76

	Case No.	Thrust Level (1bf)	Throat Radius (R^*)
B51	B51	500	0.95 in (24 mm)
B52	B52	100	0.42 in (11 mm)
B53	B53	50	0.30 in (7.6 mm)
B54	B54	10	0.13 in (3.4 mm)
B55	B55	1	0.04 in (1.1 mm)

Fig. 21b.   Pressure contours for various thrust sizes in Case Group B5 (bell-shaped nozzle, area ratio 200:1, $P_0=$ 100 psia, $T_0=5000$ R)

Case No.	Thrust Level (lbf)	Throat Radius (R*)
B61	500	0.95 in (24 mm)
B62	100	0.42 in (11 mm)
B63	50	0.30 in (7.6 mm)
B64	10	0.13 in (3.4 mm)
B65	1	0.04 in (1.1 mm)

Fig. 22a. Mach number contours for various thrust sizes in Case Group B6 (bell-shaped nozzle, area ratio 500:1, P_O=100 Psia, T_O=5000 R)

Case No.	Thrust Level (lbf)	Throat Radius (R*)

B61   500   0.95 in (24 mm)

B62   100   0.42 in (11 mm)

B63   50   0.30 in (7.6 mm)

B64   10   0.13 in (3.4 mm)

B65   1   0.04 in (1.1 mm)

Fig. 22b.   Pressure contours for various thrust sizes in Case Group B6 (bell-shaped nozzle, area ratio 500:1, P_o=100 psia, T_o=5000 R)

Mach Number

Case No.	Thrust Level (lbf)	Throat Radius (R*)
C11	500	1.34 in (34 mm)

Pressure

3000 1000 700 500 300 $(\frac{N}{m^2})$
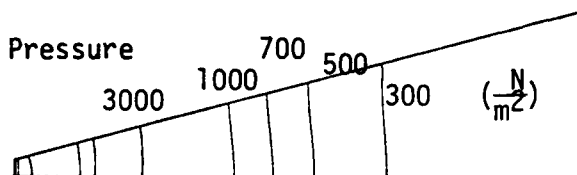
| C11 | 500 | 1.34 in (34 mm) |

Mach Number
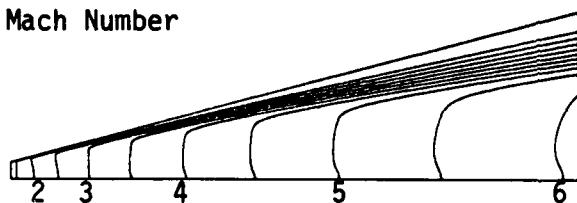
| C15 | 1 | 0.06 in (1.5 mm) |

Pressure

3000 1000 700 500 300 $(\frac{N}{m^2})$
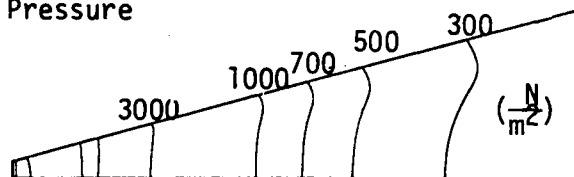
| C15 | 1 | 0.06 in (1.5 mm) |

Fig. 23. Mach number contours and pressure contours for maximum and minimum thrust sizes in Case Group C1 (Conical nozzle, area ratio 100:1, P_0=50 psia, T_0=5000 R)

Mach Number		Case No.	Thrust Level (lbf)	Throat Radius (R*)
		C31	500	1.34 in (34 mm)
Pressure		C31	500	1.34 in (34 mm)
Mach Number		C35	1	0.06 in (1.5 mm)
Pressure		C35	1	0.06 in (1.5 mm)
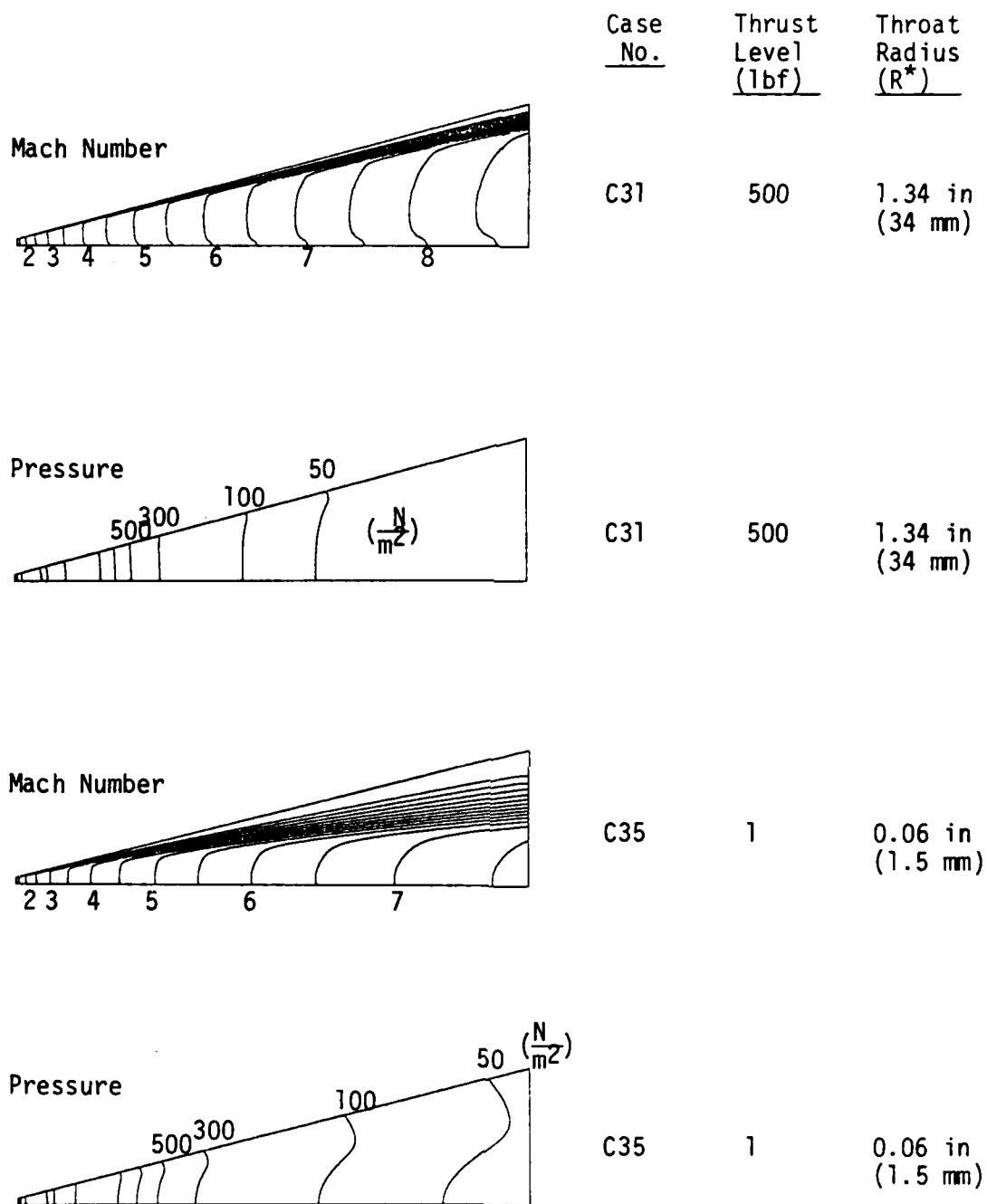
Fig. 24. <u>Mach number contours and pressure contours for maximum and minimum thrust sizes in Case Group C3 (Conical nozzle, area ratio 500:1, P_o=50 psia, T_o=5000 R)</u>
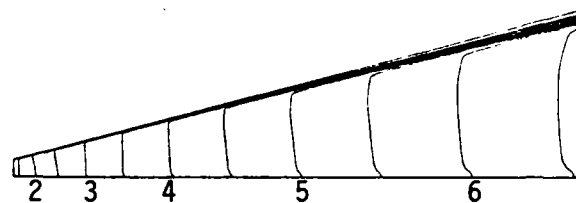
Case No.	Thrust Level (lbf)	Throat Radius (R*)
C41	500	0.95 in (24 mm)
C41	500	0.95 in (24 mm)
C45	1	0.04 in (1.1 mm)
C45	1	0.04 in (1.1 mm)
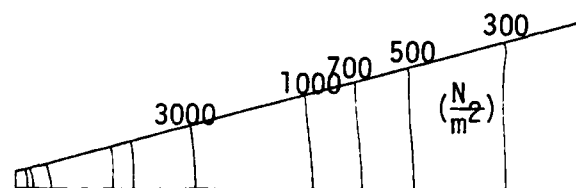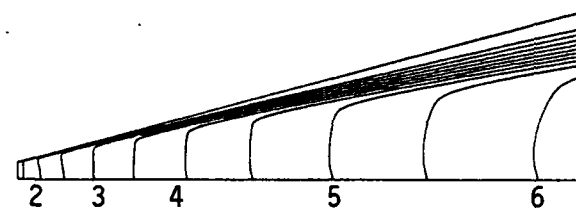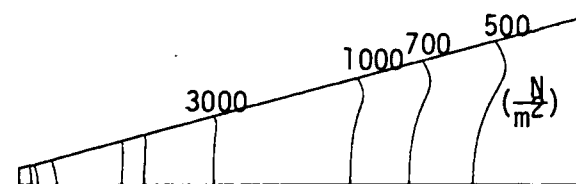
Fig. 25. Mach number contours and pressure contours for maximum and minimum thrust sizes in Case Group C4 (Conical nozzle, area ratio 100:1, P_o=100 psia, T_o=5000 R)
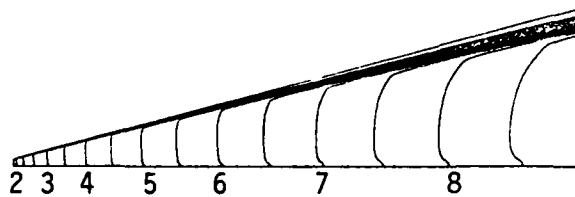
Case No.	Thrust Level (lbf)	Throat Radius (R*)
C61	500	0.95 in (24 mm)
C61	500	0.95 in (24 mm)
C65	1	0.04 in (1.1 mm)
C65	1	0.04 in (1.1 mm)
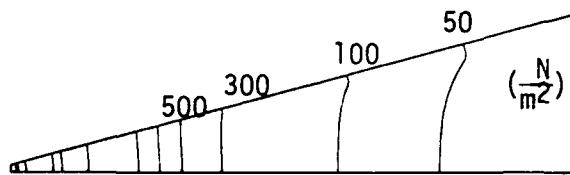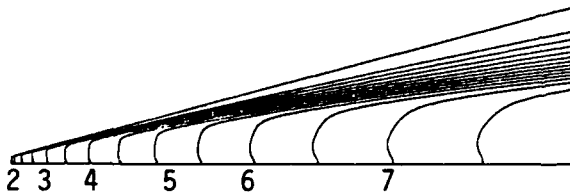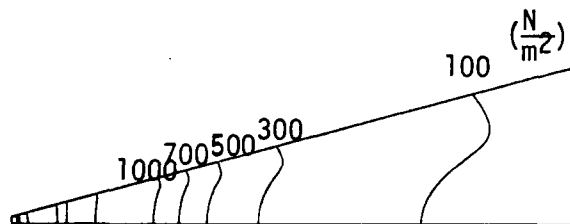
Fig. 26. Mach number contours and pressure contours for maximum and minimum thrust sizes in Case Group C6 (Conical nozzle, area ratio 500:1, P_o=100 psia, T_o=5000 R)
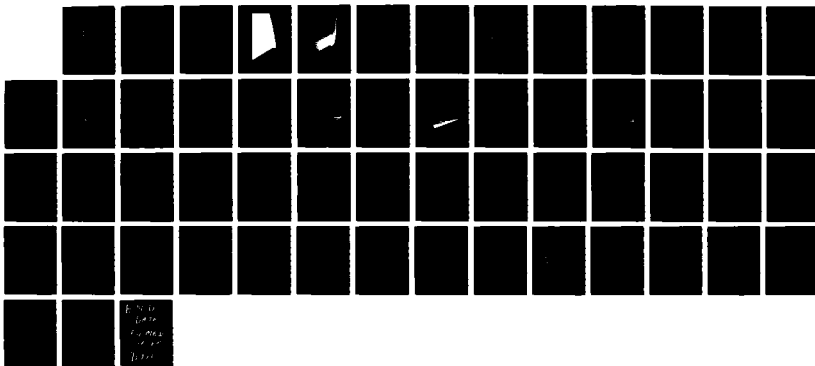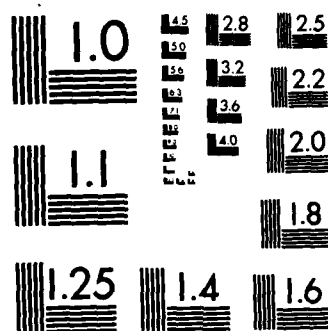
MICROCOPY RESOLUTION TEST CHART

NATIONAL BUREAU OF STANDARDS-1963-A

small (1 lbf) nozzles. Both the Mach number and pressure contours are given on the same figure. Corresponding results for the 500:1 area ratio nozzle are on Fig. 24. Figures 25 and 26 show results for the 100 psia chamber pressure. Again, the first of these two, Fig. 25, is for the 100:1 nozzle while the second, Fig. 26, is for the 500:1 nozzle. The relative effects of expansion ratio and thrust size are about the same for the conical nozzle as for the bell-shaped nozzle. The important comparison here is between the conical and bell-shaped geometries. The change in the nozzle geometry is, however, not a very significant effect. For example, comparison of the results on Fig. 23 with those on Fig. 16 show the bell-shaped nozzle consistently produces higher flow expansion than does the conical nozzle. This is because of the smaller viscous effects in the shorter bell-shaped nozzle. Another advantage of the bell-shaped nozzle is that it provides smaller divergence losses and so should produce more thrust both because of its shape and its reduced viscous losses. Finally, we note that the bell-shaped nozzle is not a highly optimized geometry for these very viscous flows, and that an improved nozzle design that takes into account the viscous effects should be undertaken to provide optimum performance. The present computer tools should be useful for this purpose.

Nearfield Plume Characteristics

The nozzle flowfield solutions presented in the previous Subsection were used as initial data for the plume calculations. These calculations were performed with the TD2P method of

84

characteristics procedure in CONTAM, and the SLINES geometrical expansion module of CONTAM. The near-field results are presented in the present Section.

A characteristics net for representative plume conditions is shown in Fig. 27. The flow conditions for the case shown are those for Case B11 (a bell-shaped nozzle with an area ratio of 100:1, chamber conditions of 50 psia and 5000R, and a thrust level of 500 lb$_f$). The complete characteristics net for this case is shown in Fig. 27a. The outer boundaries of the near-field calculation are nominally taken as 50 throat radii from the centerline in the radial direction and 100 throat radii in the axial direction. A local view of conditions near the nozzle lip that gives more detail of this initial expansion region is shown in Fig. 27b. Characteristic nets like the ones shown in Fig. 27 were obtained for all cases in the test matrix and were used to generate the contour plots discussed below.

Mach number contour plots for all cases in the calculation matrix are shown in Figs. 28 to 37. These plots show constant Mach number contours for the nearfield plume starting from the nozzle exit plane and extending to a region where all streamline curvature is gone and the streamlines are completely straight. The general shape of the constant Mach number contours is about the same at all conditions and the basic characteristics of the near plume flowfields can be described by referring to Fig. 28. In general, each constant Mach number contour extends far downstream in regions near the axis, but the contours first return closer to the nozzle as we move away from the axis before again extending radially
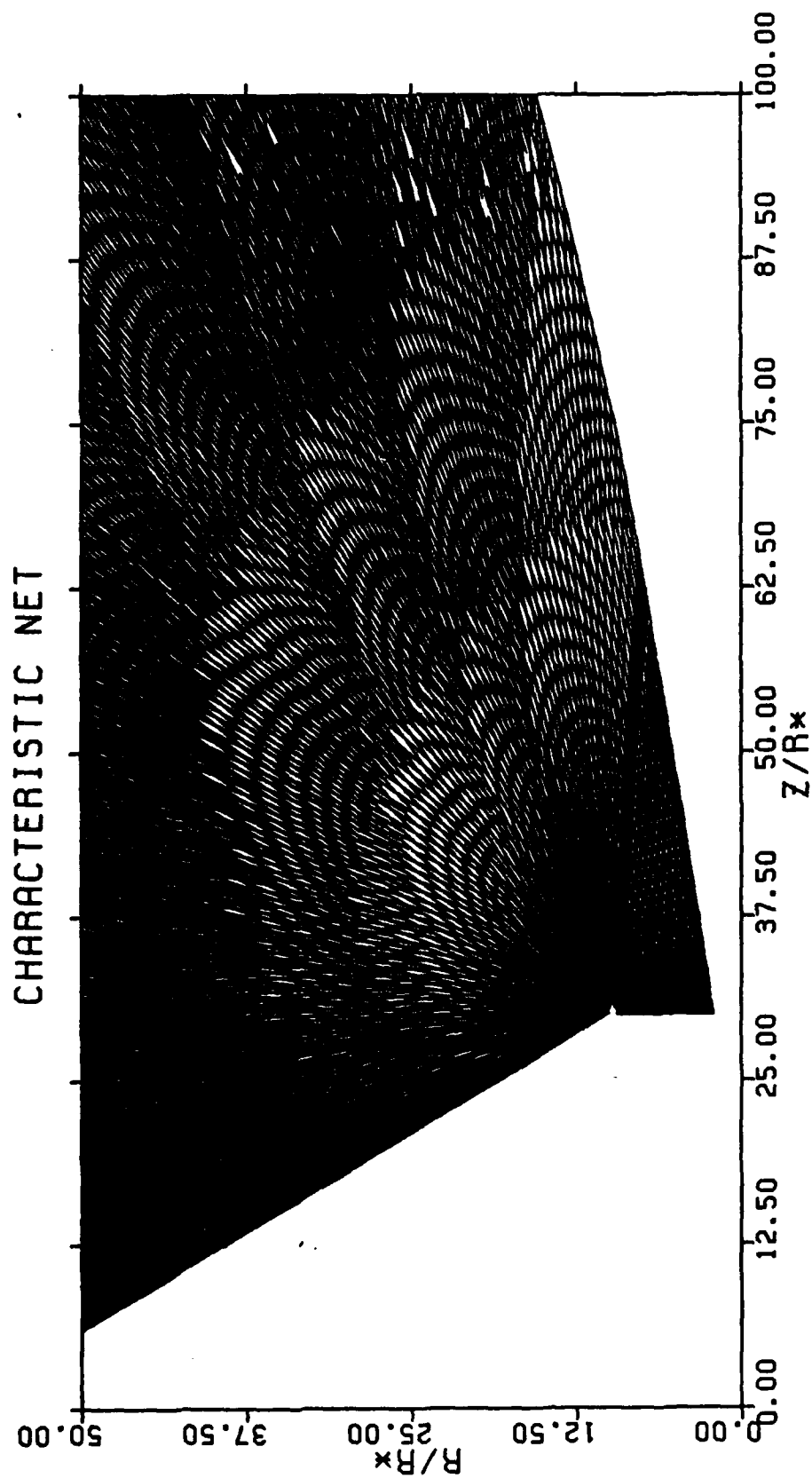
Fig. 27a. Characteristic net of the near-field plume of Case B11. (Bell-shaped nozzle, area ratio 100:1, P_0=50 psia, T_0=5000 R, thrust level=500 lbf)
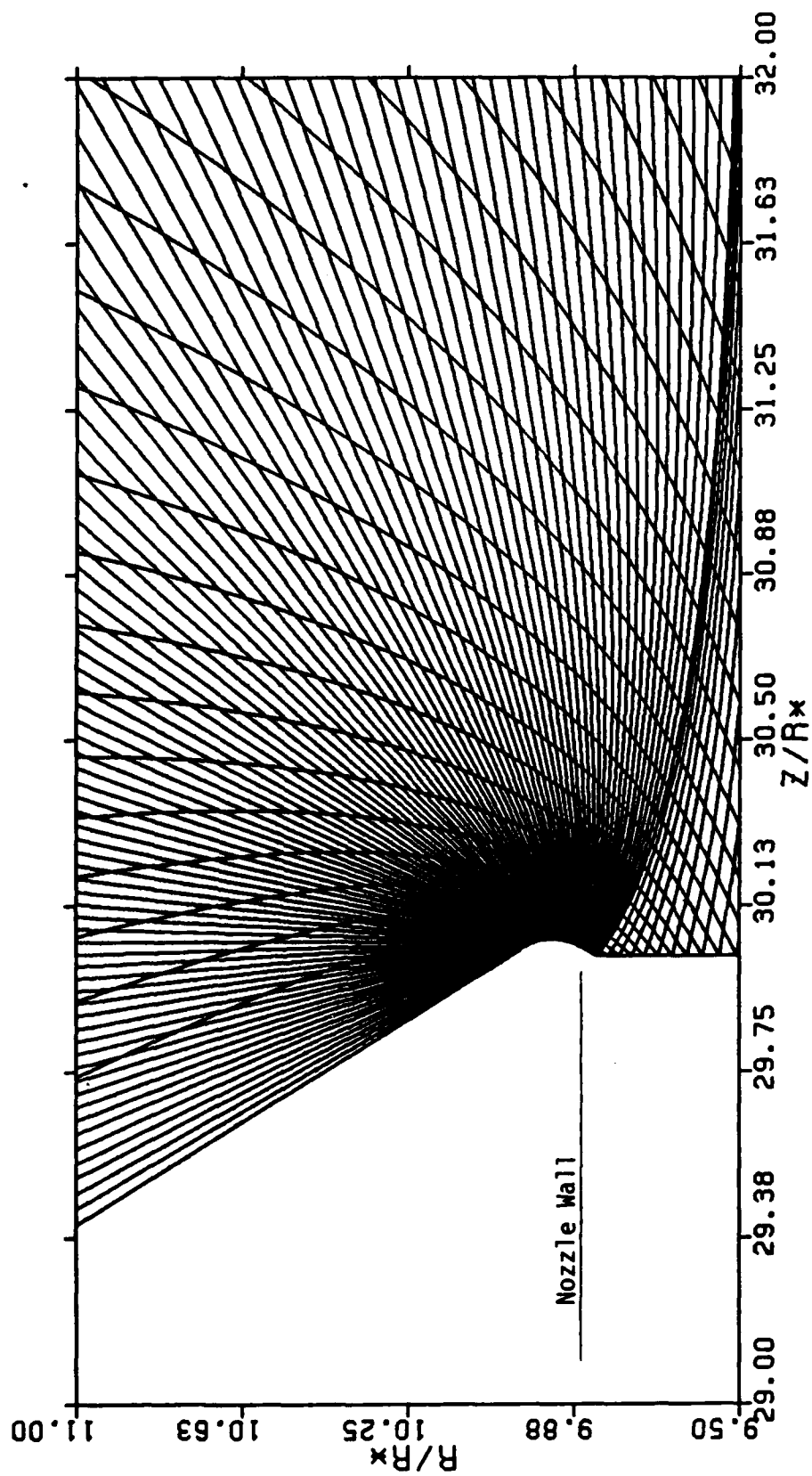
Fig. 27b. Magnified view of the characteristic net near the nozzle lip for the Case shown in Fig. 27a.
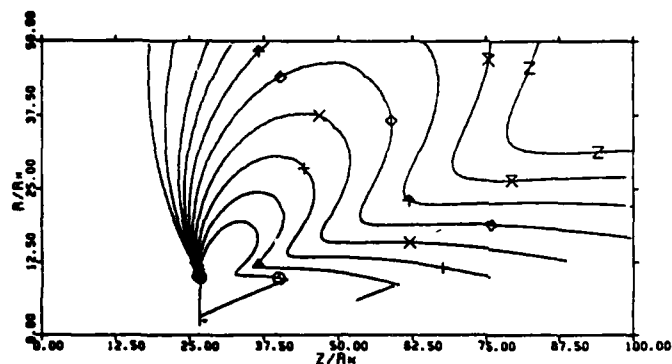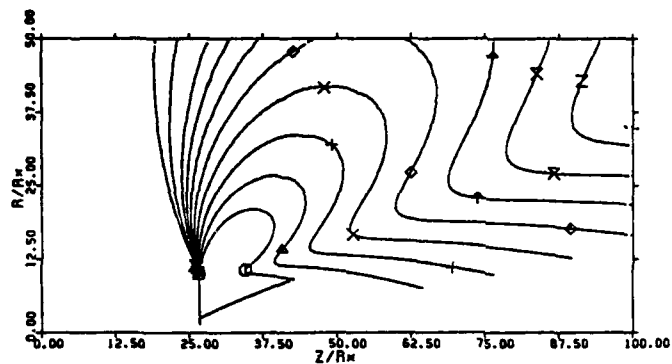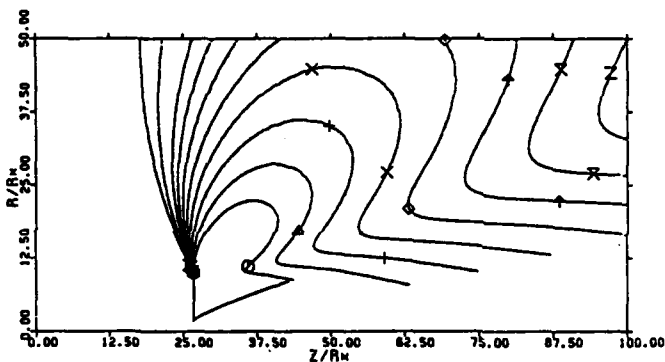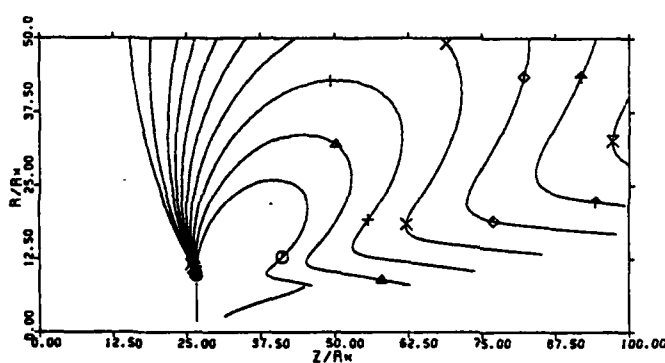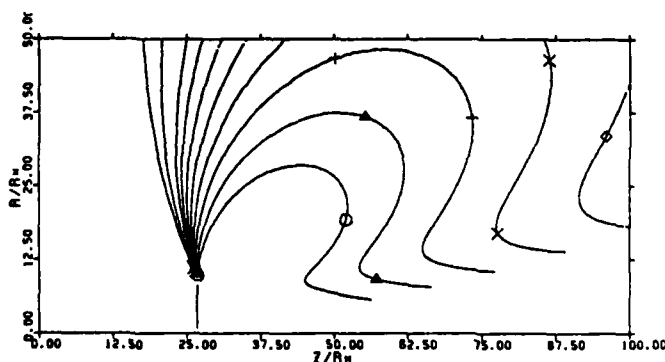
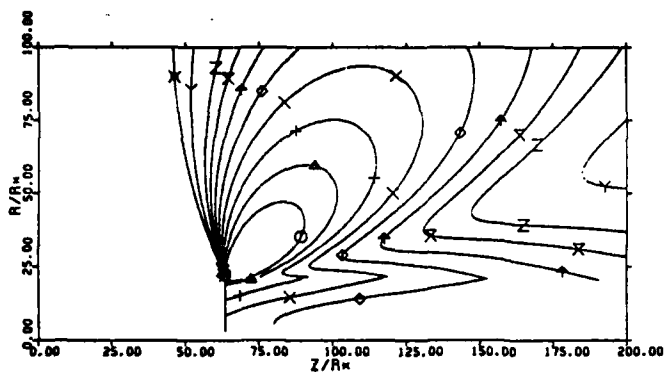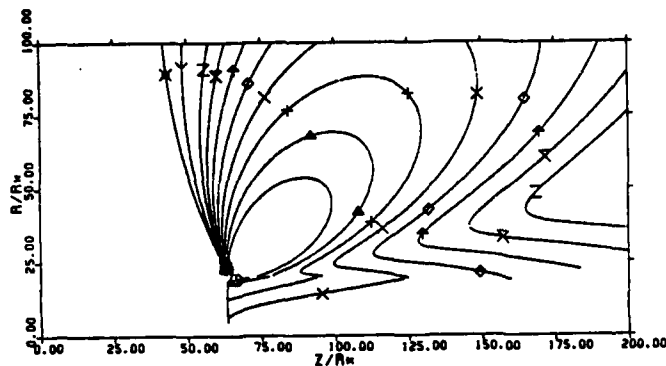Fig. 28. Mach number contours of nearfield plume for Case Group B1 (Bell-shaped nozzle, area ratio 100:1, P_o=50 psia, T_o=5000 R)
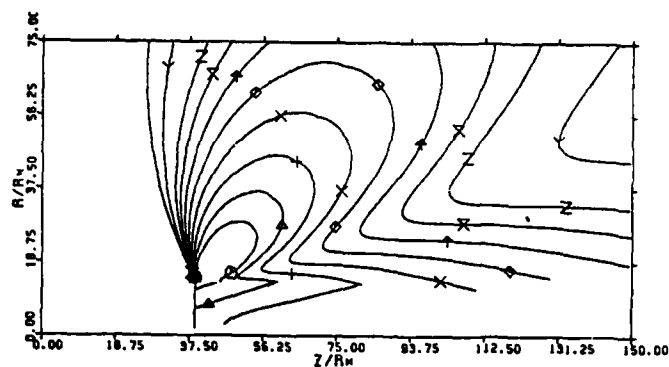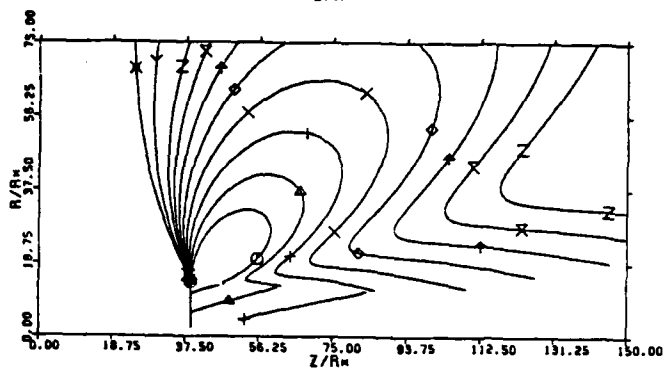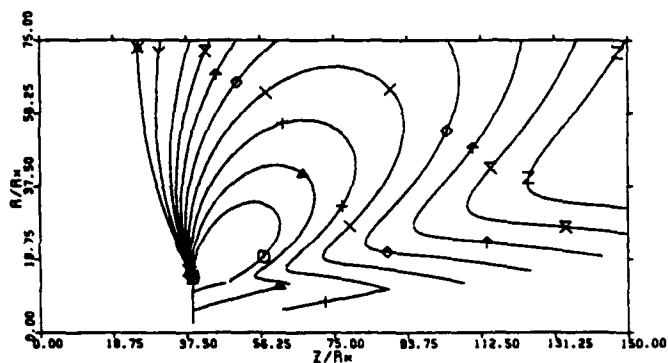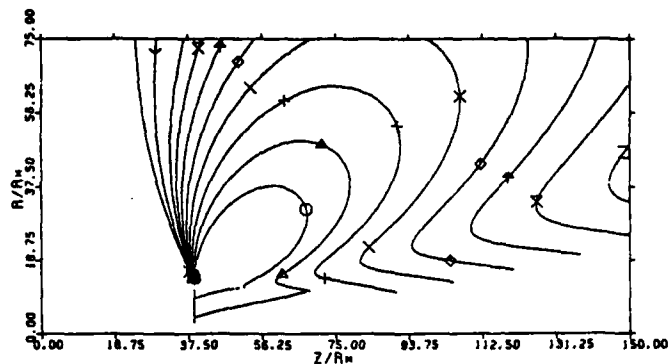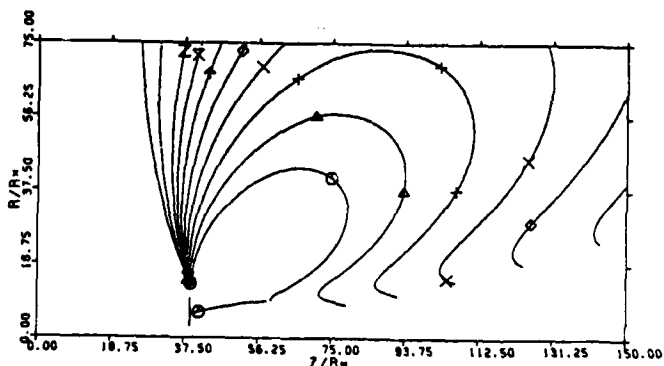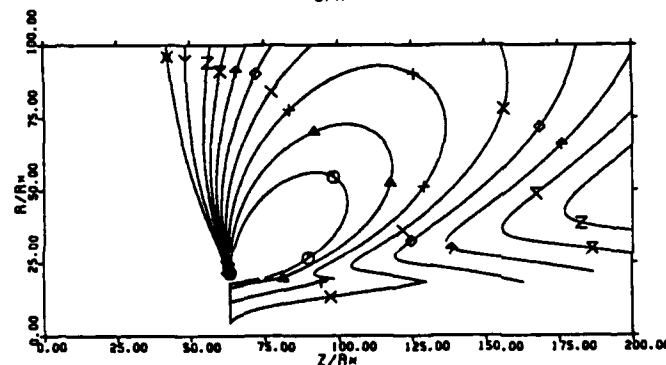
Fig. 29. Mach number contours of nearfield plume of Case Group B2 (Bell-shaped nozzle, area ratio 200:1, P_0=50 psia, T_0=5000 R)
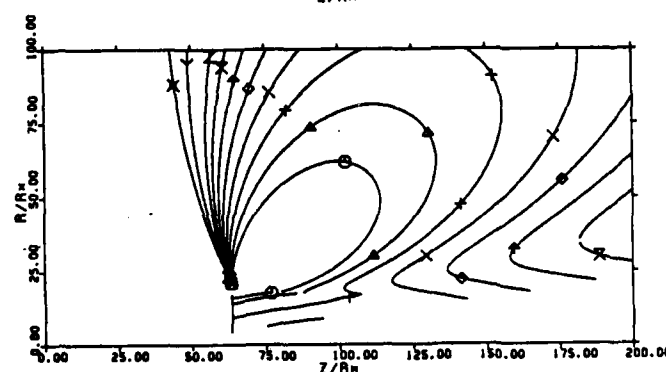
Fig. 30. Mach number contours of nearfield plume of Case Group B3
(Bell-shaped nozzle, area ratio 500:1, P_0=50 psia, T_0=5000 R)
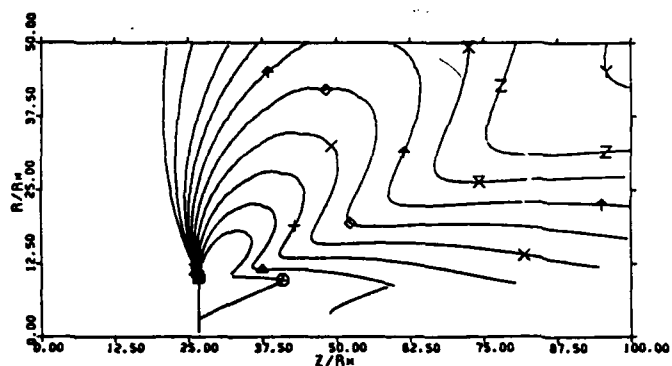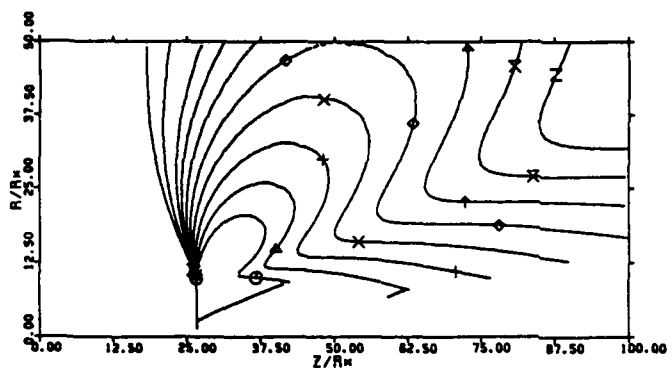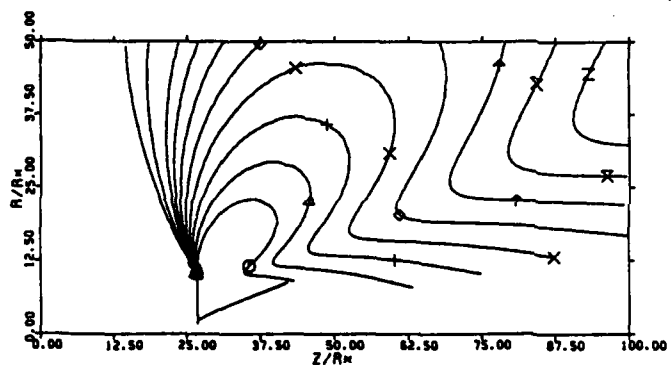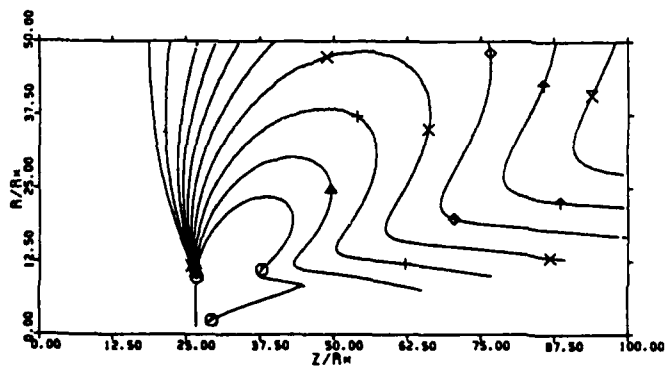
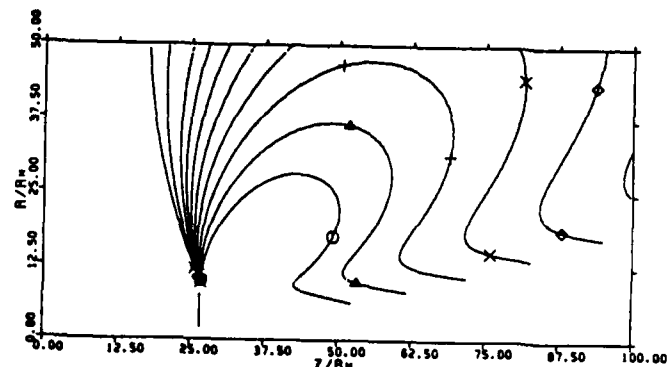| Case No.	Thrust Level (lbf)	Throat Radius (R*)
B41	500	0.95 in (24 mm)
B42	100	0.43 in (11 mm)
B43	50	0.30 in (7.7 mm)
B44	10	0.13 in (3.4 mm)
B45	1	0.04 in (1.1 mm)

Fig. 31. Mach number contours of nearfield plume of Case Group B4 (Bell-shaped nozzle, area ratio 100:1, P_0=100 psia, T_0=5000 R)

91

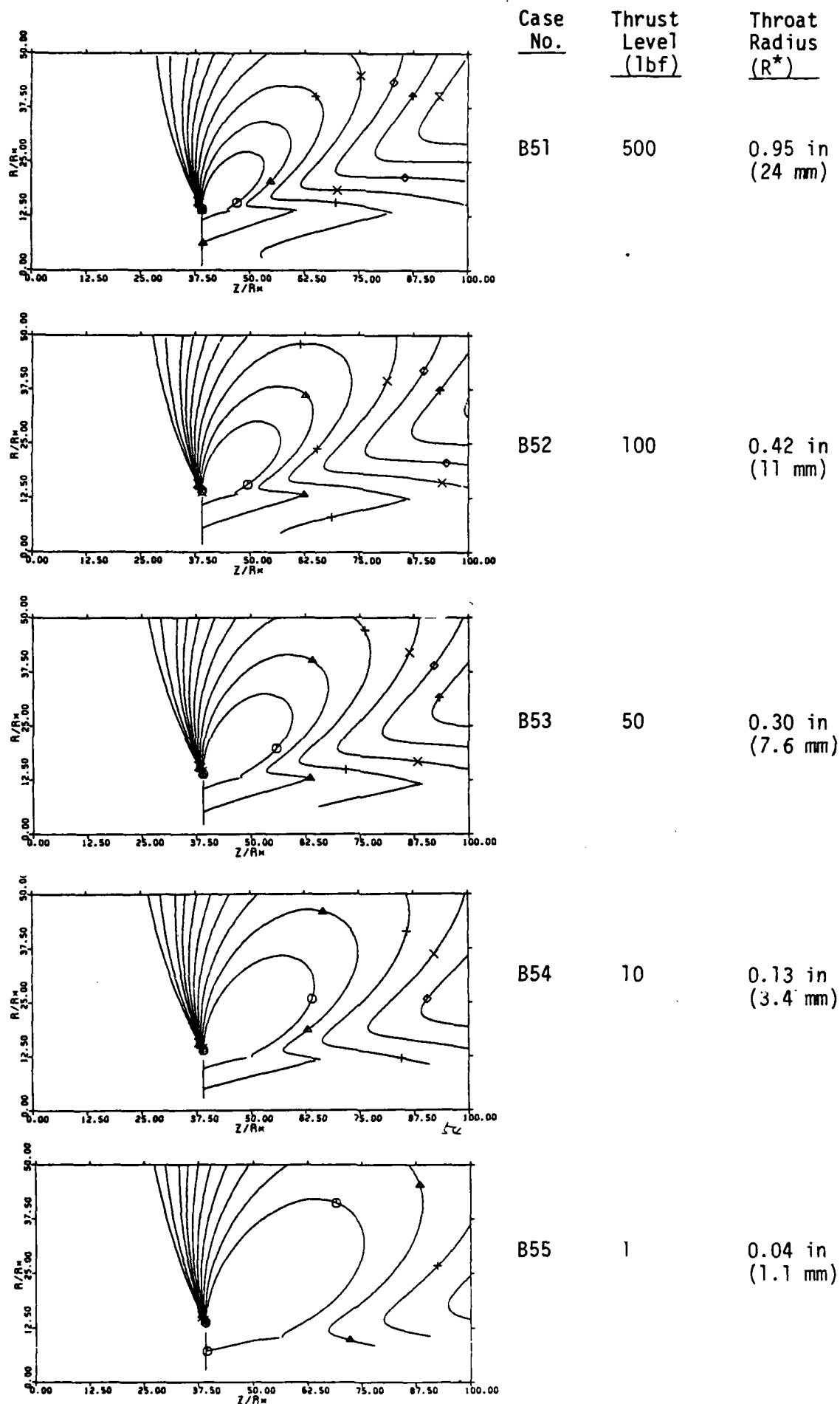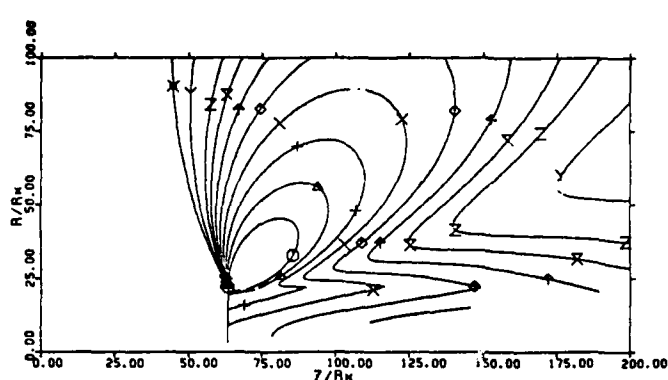| Case No.	Thrust Level (lbf)	Throat Radius (R*)
B51	500	0.95 in (24 mm)
B52	100	0.42 in (11 mm)
B53	50	0.30 in (7.6 mm)
B54	10	0.13 in (3.4 mm)
B55	1	0.04 in (1.1 mm)

Fig. 32. Mach number contours of nearfield plume of Case Group B5 (Bell-shaped nozzle, area ratio 200:1, P_0=100 psia, T_0=5000 R)
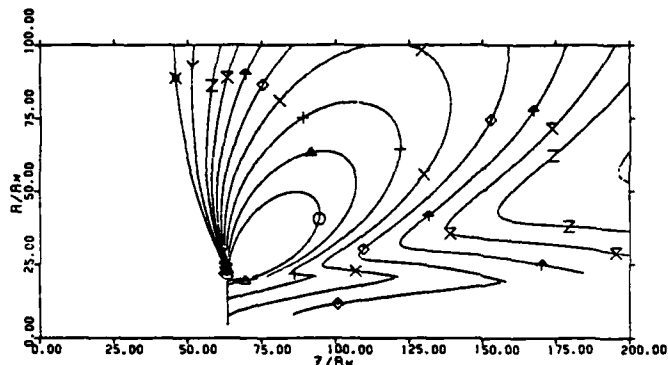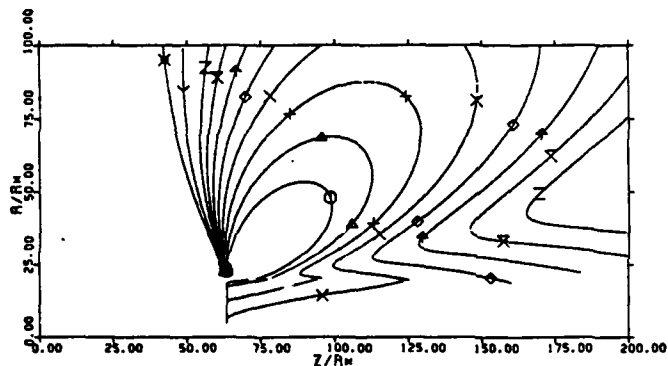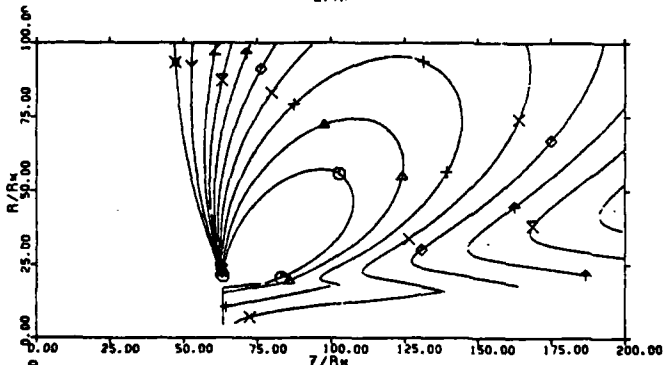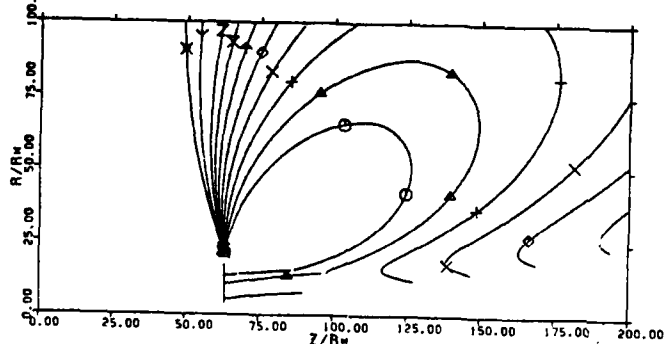
Fig. 33.   Mach number contours of nearfield plume of Case Group B6
            (Bell-shaped nozzle, area ratio 500:1, P_0=100 psia, T_0=5000 R)

93

Case C11, Thrust level = 500 lbf
Throat Radius = 1.34 in (34 mm)

Case C15, Thrust Level = 1 lbf
Throat Radius = 0.06 in (1.5 mm)

⊙	7.
△	8.
+	9.
X	10.
◇	11.
⬙	12.
⊠	13.
Z	14.
Y	16.
⋈	18.

Fig. 34.   Mach number contours of nearfield plume of Case Group C1
(Conical nozzle, area ratio 100:1, P_0=50 psia, T_0=5000 R)

94
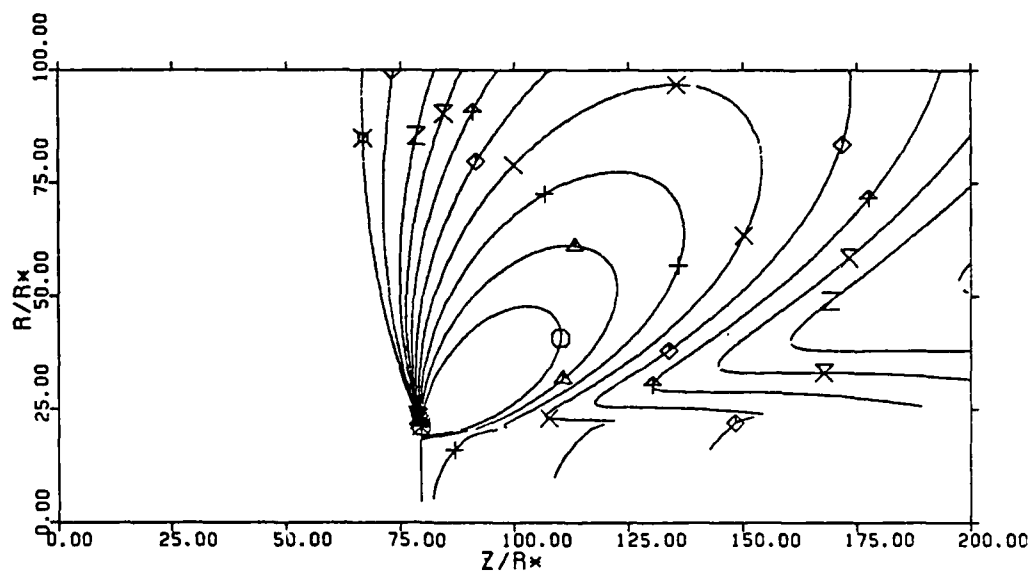
Case C31   Thrust Level = 500 lbf
            Throat Radius = 1.34 in (34 mm)

⊕	7.
△	8.
+	9.
X	10.
◇	11.
⊕	12.
⋈	13.
Z	14.
Y	16.
⋈	18.

Case C35   Thrust Level = 1 lbf
            Throat Radius = 0.06 in (1.5 mm)

Fig. 35.   Mach number of nearfield plume of Case Group C3
            (Conical nozzle, area ratio 500:1, P_o=50 psia,
            T_o=5000 R)

95

Case C41   Thrust Level = 500 lbf
Throat Radius = 0.95 in (24 mm)

Case C45   Thrust Level = 1 lbf
Throat Radius = 0.04 in (1.1 mm)

7.
8.
9.
10.
11.
12.
13.
14.
16.
18.

Fig. 36.   Mach number contours of nearfield plume of Case Group C4
(Conical nozzle, area ratio 200:1, P_0=100 psia, T_0=5000 R)

Case C61   Thrust Level = 500 lbf
            Throat Radius = 0.95 in (24 mm)

Case C65   Thrust Level = 1 lbf
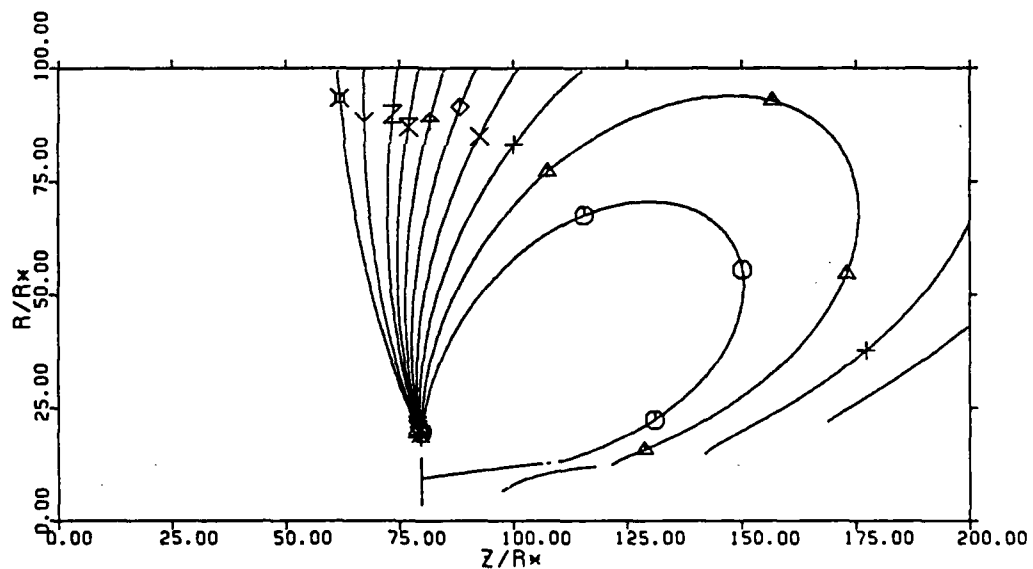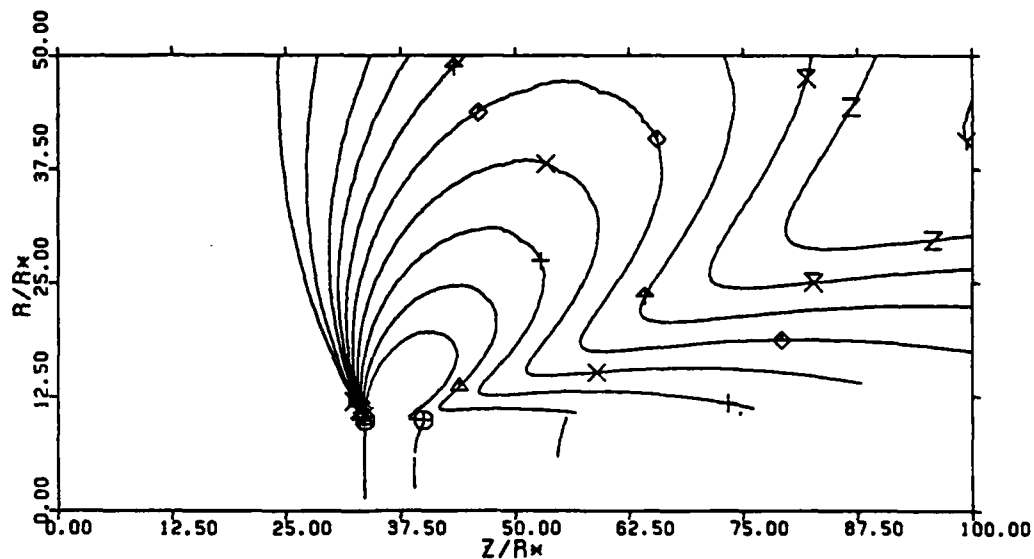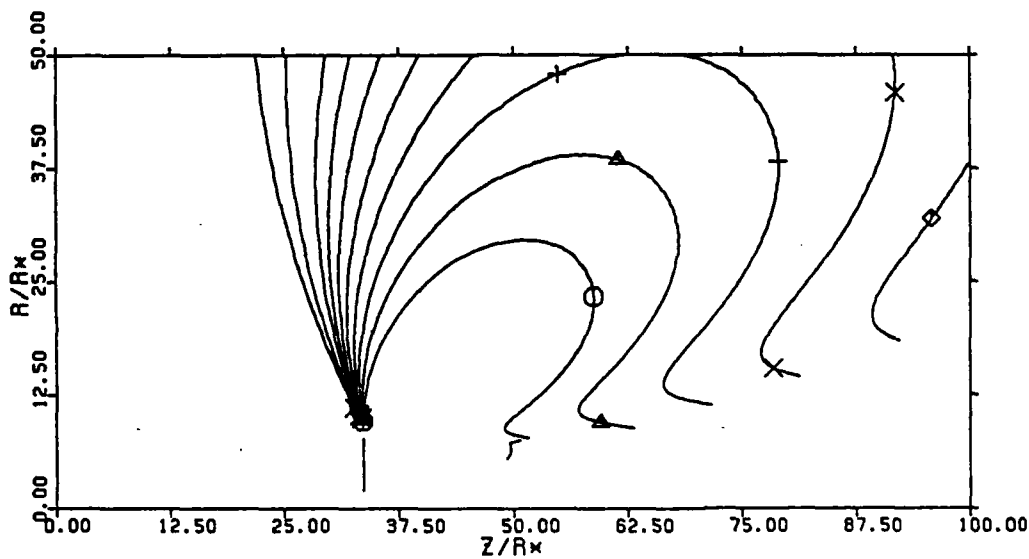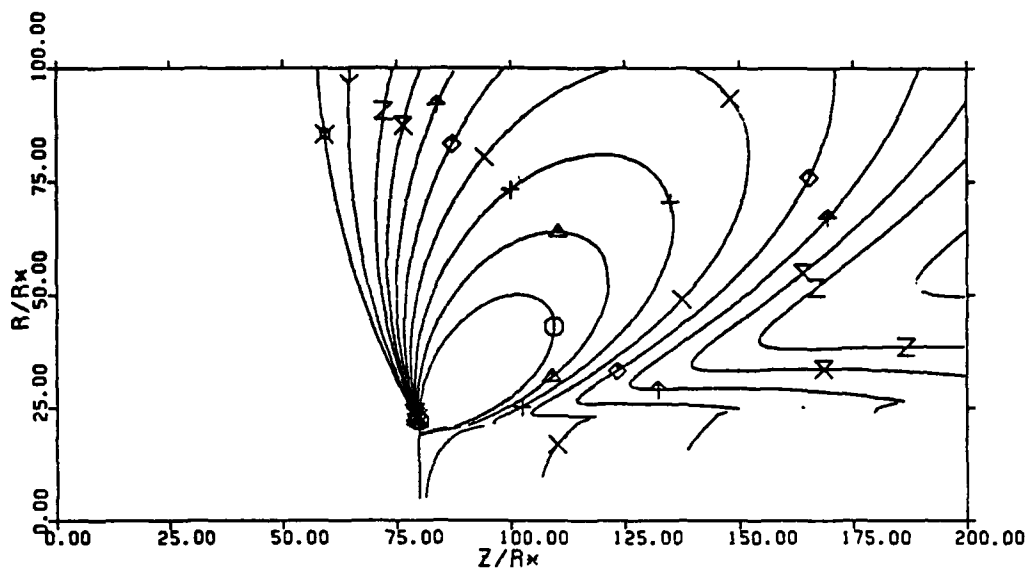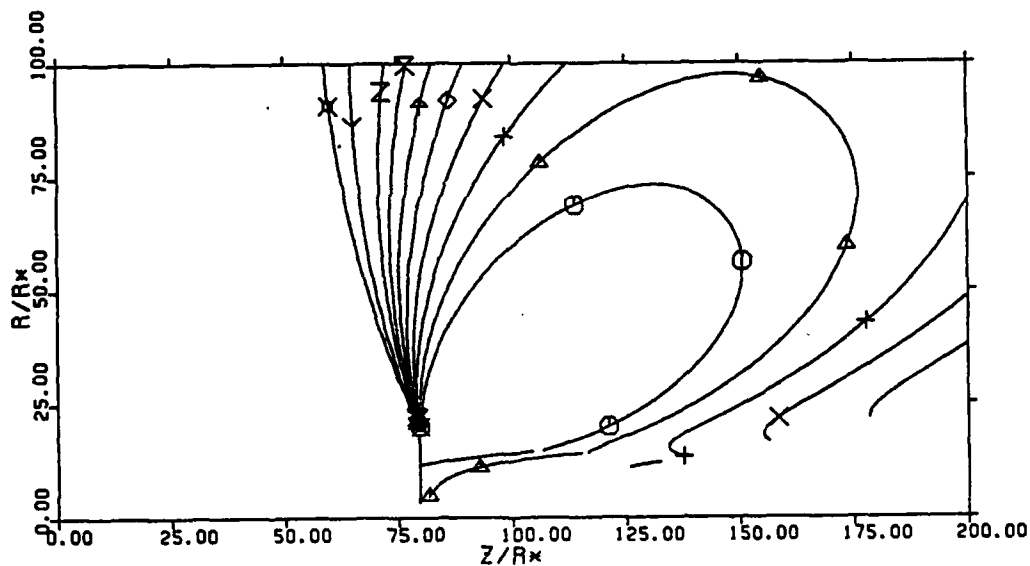   Throat Radius = 0.04 in (1.1 mm)

Fig. 37.   Mach number contours of nearfield plume of Case
            Group C6
            (Conical nozzle, area ratio 500:1, P_0=100 psia, T_0=5000 R)

97

outward in the rotational flow region to form the lobe mentioned

earlier. On the upstream edge of the plume the Mach number

contours all return to the nozzle lip at a common location. These

regions of near-approach correspond to local regions of high

acceleration. The one on the plume edge occurs because of the

local vacuum conditions and, as discussed earlier, accurate details

of this region require that transitional effects be included. The

strong acceleration region at about 30° and the lobe of slower

acceleration at about 45 degrees are induced by the total pressure

gradient in the boundary layer. It is this lobe with which we are

particularly interested in the present analysis because it is this

portion of the plume that eventually impinges on the collector.

The results presented in Fig. 28 are for the bell-shaped

nozzle at an area ratio of 100:1 and a chamber pressure of 50 psia.

Contour plots are given for all five thrust levels. In general, we

see less expansion as we move from the 500 lb_f nozzle to the 1 lb_f

nozzle. The plot for the larger nozzle contains Mach number

contours up to M = 14 (see key at the upper left of the Figure)

whereas the plot for the smallest nozzle only expands up to M = 11

in this same region. The reason is because of the thicker boundary

layer in the 1 lb_f nozzle. Also, the low acceleration lobe caused

by the boundary layer is observed to increase in size as the thrust

level is reduced until at the smallest nozzle size, this lobe

nearly dominates the entire flowfield.

The same qualitative comparisons remain true for the 200:1

nozzle and the 500:1 nozzle results that are given in Figs. 29 and

30, respectively. These results again are for the 50 psi case and

show the effect of changing the area ratio. Note, however, that the scales are different for the three area ratio nozzles. For the 100:1 nozzle, the scales run to $r/r^* = 50$ and $x/r^* = 100$. For the 200:1 case, the extremes are $r/r^* = 75$ and $x/r^* = 150$, while for the 500:1 case, they are $r/r^* = 100$ and $x/r^* = 200$.

Comparisons of the results on Figs. 29 and 30 with those on Fig. 28 show the effects of both expansion ratio and nozzle size. In general, the higher expansion ratio nozzles provide lower Mach number plumes than do the smaller expansion ratio nozzles. This is particularly true for the smaller thrust sizes where the offsetting growth of the boundary layer in the longer nozzles counters the effects of the higher expansion ratios. The increases in nozzle expansion ratio always serve to increase the size of the low-acceleration lobe because of the increased thickness of the boundary layer. This effect can likewise be seen by comparing these three Figures.

Corresponding Mach number contours for the 100 psia chamber pressure cases are given in Figs. 31, 32 and 33. As observed for the nozzle calculations, this factor of two change in Reynolds number (as compared with the 50 psia case) has a very minor effect on the expansion characteristics of the exhaust jet and similarly small changes can be seen in the plume results. Again, the primary effect of chamber pressure on plume impingement is expected to arise because of the counter-acting effects of the increased level of pressure and the smaller throat radius, not because of the change in the flowfield structure.

The Mach number contours for the conical nozzle calculations
are given on Figs. 34 to 37. The trends within the conical nozzle
calculations are analogous to those observed for the bell-shaped
nozzle calculations. Comparing the bell-shaped nozzles to the
corresponding conical nozzles shows little difference. The
expansions obtained from the bell-shaped nozzles are always
slightly higher than those obtained from the conical nozzles, but
the effect is small.

Farfield Plume Characteristics

The nearfield plume calculations described in the previous
Subsection have been used to compute the farfield plume
characteristics by the geometrically based SLINES method described
in Computational Procedures. These farfield expansion calculations
extend the results out to the collector. The collector lies
approximately between 1000 and 5000 nozzle throat radii away from
the exit plane as indicated in Fig. 9. A schematic of the
collector along with streamlines for Case B11 is shown on Fig. 38.
On this scale, the nozzle is little more than a point and is
located at the origin. As indicated earlier, the collector size
was scaled directly with the thrust size for the present
calculations. Consequently, in the normalized variables of Fig.
38, the collector size and location will be independent of thrust
size, and will change only with chamber pressure.

The straight lines on Fig. 38 represent streamlines as
extrapolated from the outer regions of the MOC solutions given
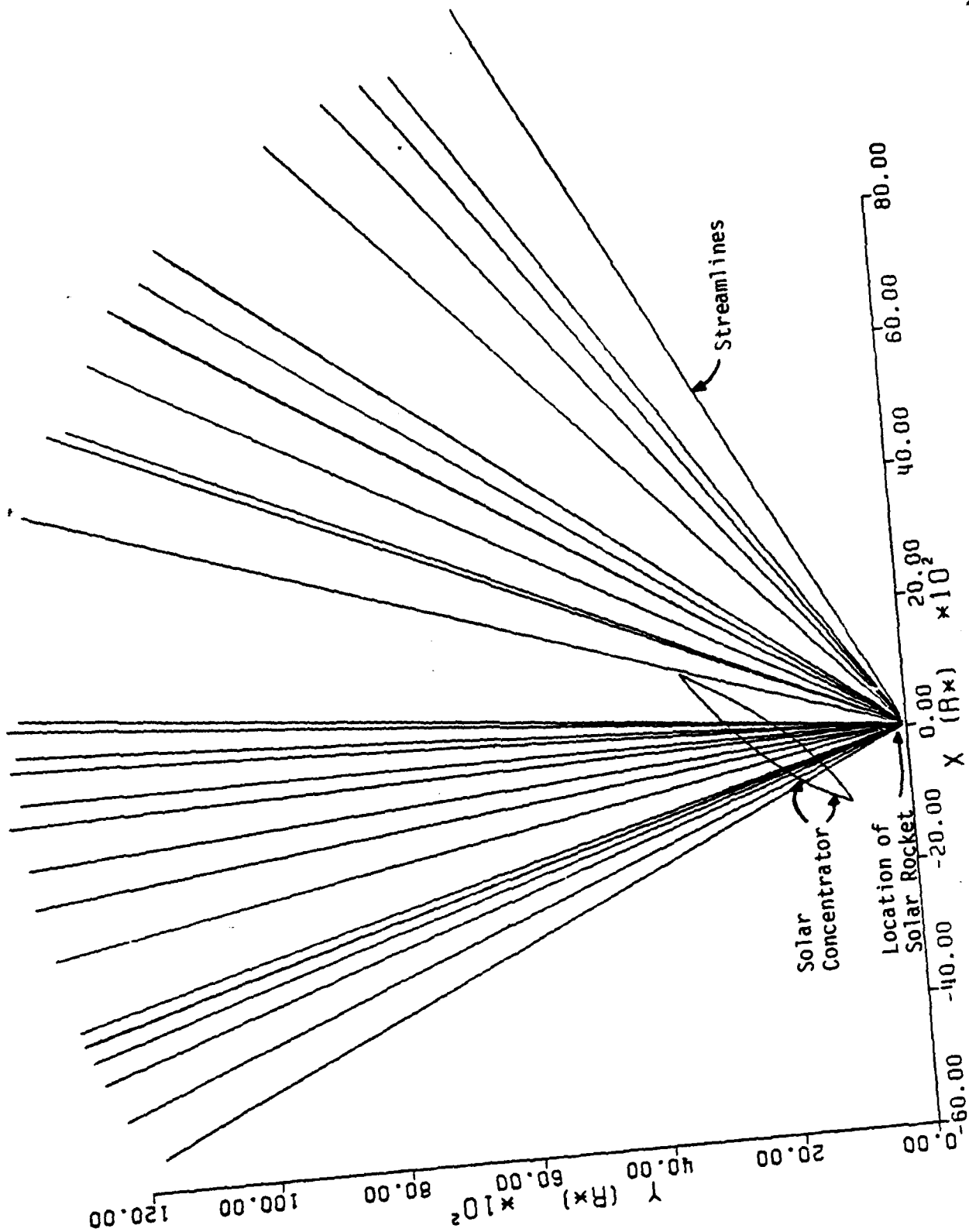earlier. Those streamlines that intersect the front surface of the

Fig. 38. Streamlines of farfield plume of Case B11 (Bell-shaped nozzle, area ratio =100:1, P_0=50 psia, T_0=5000 R, Thrust=500 lbf)

mirror are the ones that give rise to the plume-mirror impingement. These results are for the bell-shaped nozzle with a 100:1 area ratio, 50 psia chamber pressure, and 500 lb$_f$ of thrust. Corresponding Mach number and pressure .contours for this case are given in Figs. 39 and 40, while the heat flux per unit area is shown on Fig. 41.

The effect of chamber pressure on these farfield quantities is given in Figs. 42 to 44. These results are for identical conditions as those in Figs. 38 to 41 except that here the chamber pressure is 100 psia. The higher chamber pressure leads to a smaller throat radius and, hence, even though the physical size of the collector for this 500 lb$_f$ nozzle is the same as that in Fig. 38, its size in nondimensional variables is increased. This increased nondimensional size of the collector partially offsets the higher pressure levels in the plume because it effectively lies farther away from the nozzle.

Pressure and Heat Transfer Signatures on the Collector Surface

The pressure loadings and heat transfer to the front surface of the collector were determined by interpolating farfield solutions like those presented in the previous Subsection. The results are presented in the present Subsection as plots of the pressure and heat transfer as a function of the arc-length distance along the front surface of the collector. The arc-length distance is measured from the front, innermost point on the collector as shown in Fig. 45.
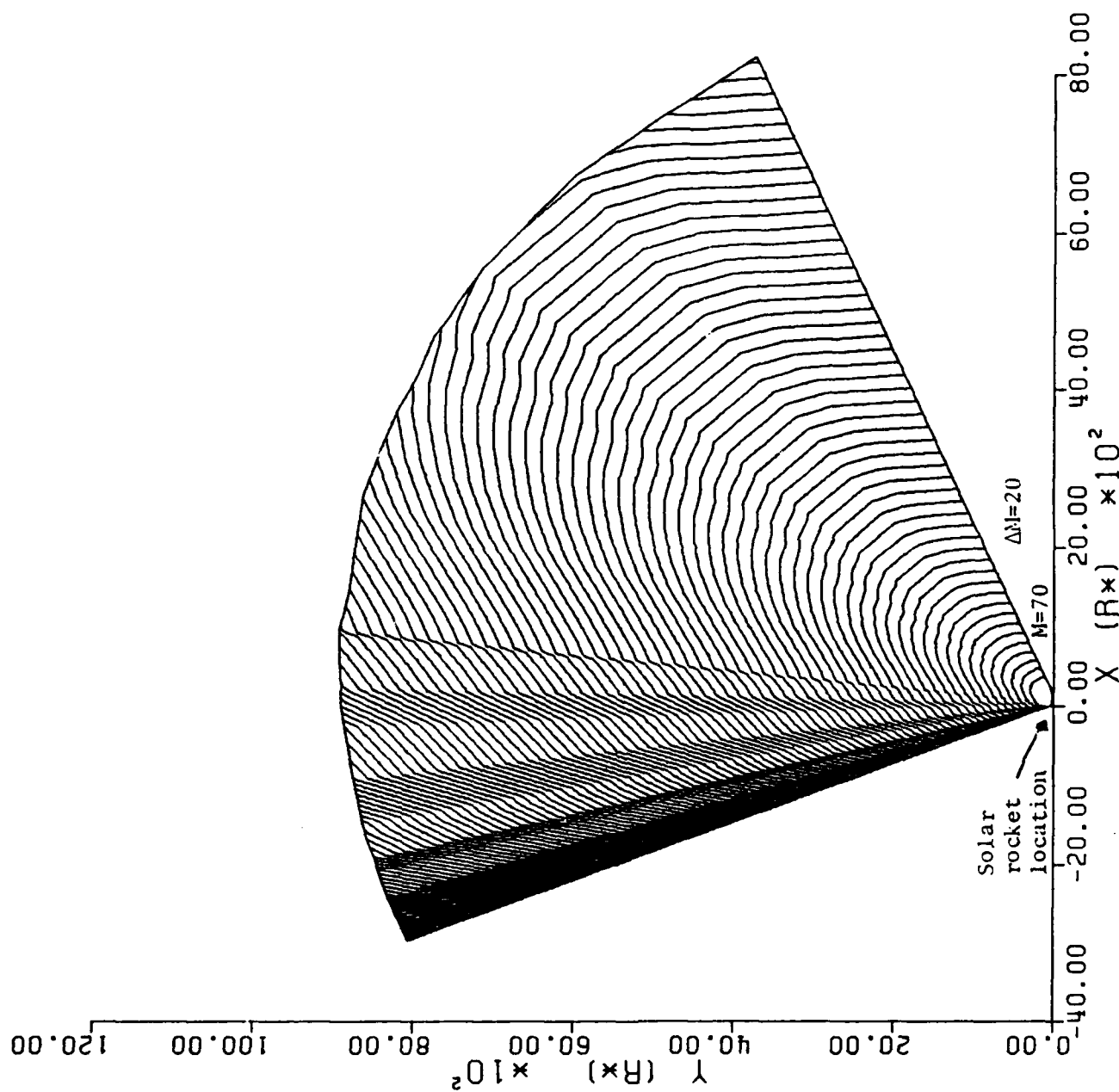
102

Fig. 39.   Mach number contours of farfield plume of Case B11
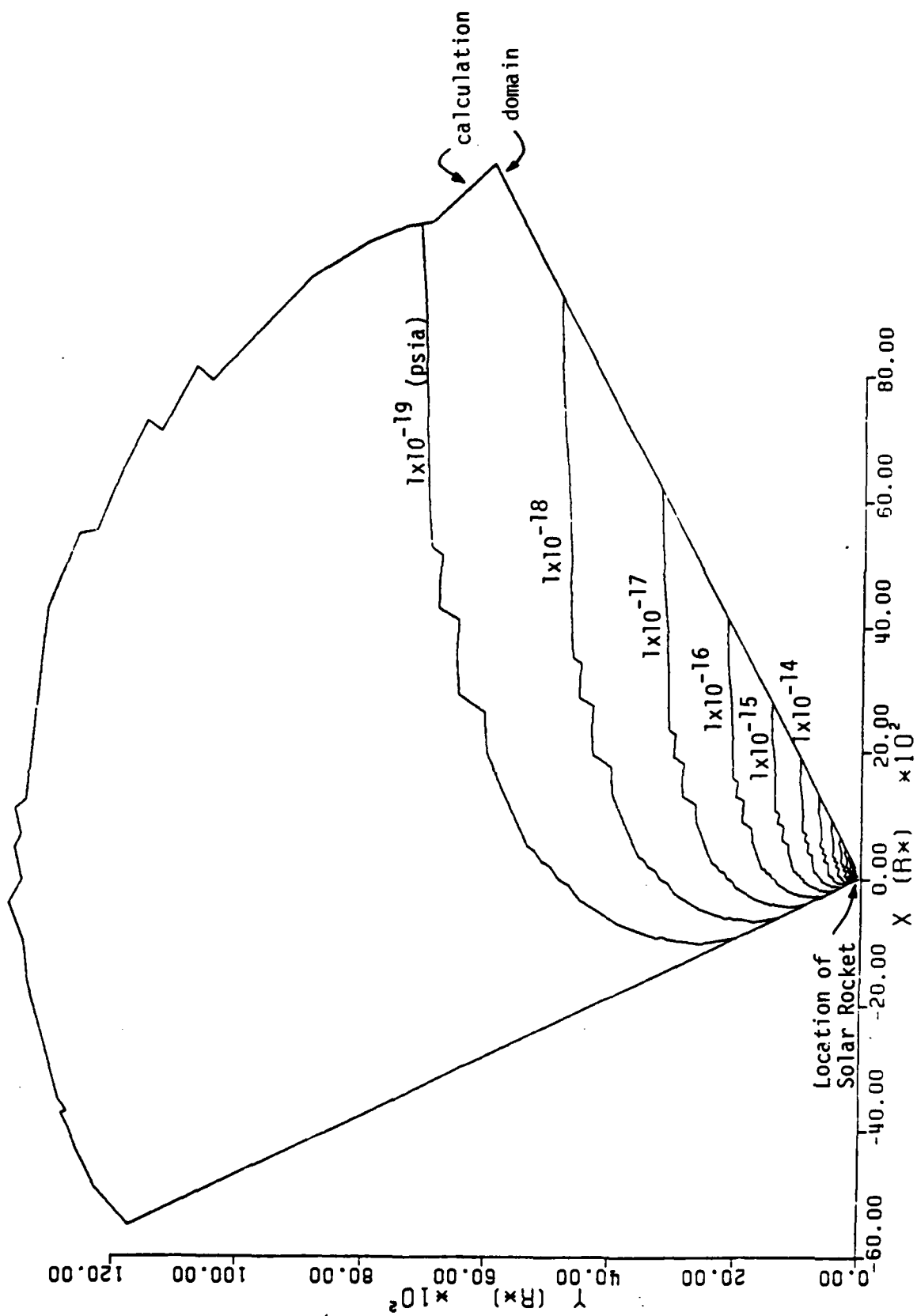(Bell-shaped nozzle, area ratio=100:1, P_0=50 psia, T_0=5000R, Thrust=500 lbf)

103

Fig. 40.   Pressure contours of farfield plume of Case B1

104

Fig. 41. Heat transfer effect contours of farfield plume of Case B11

Fig. 42. Streamlines of farfield plume of Case B41
(Bell-shaped nozzle, area ratio=100:1, P_0=100 psia, T_0=5000R, Thrust=500 lbf)
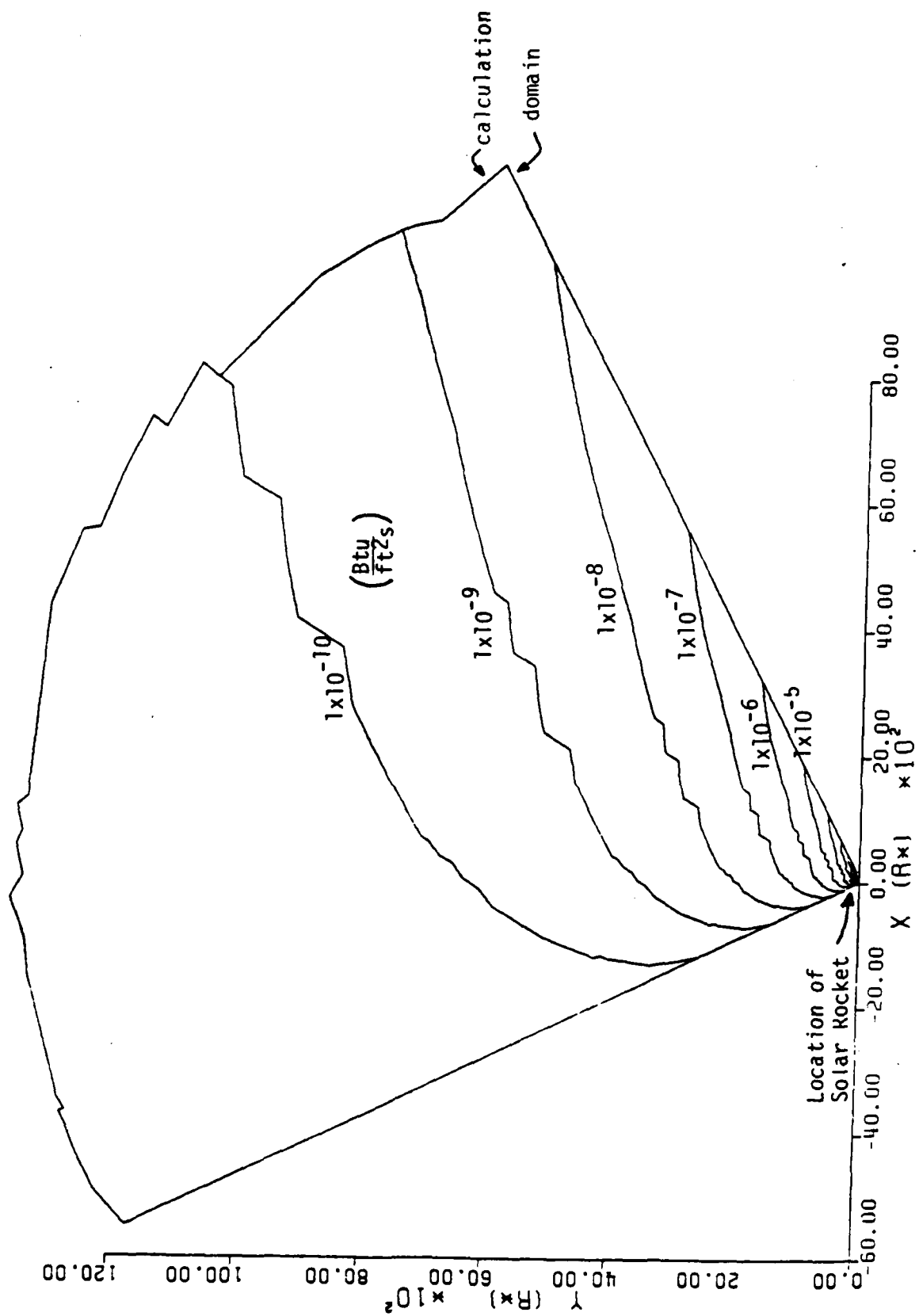
106

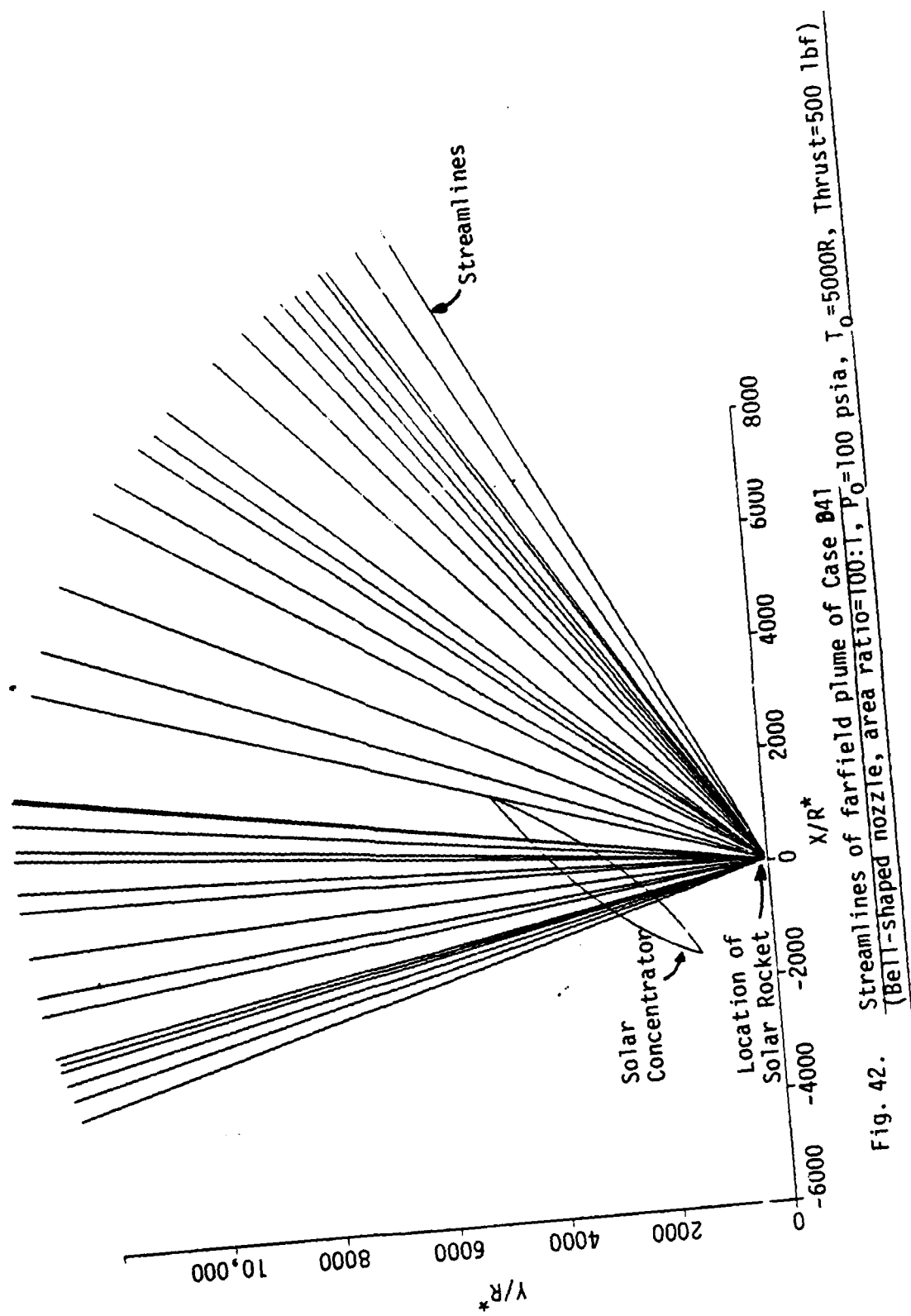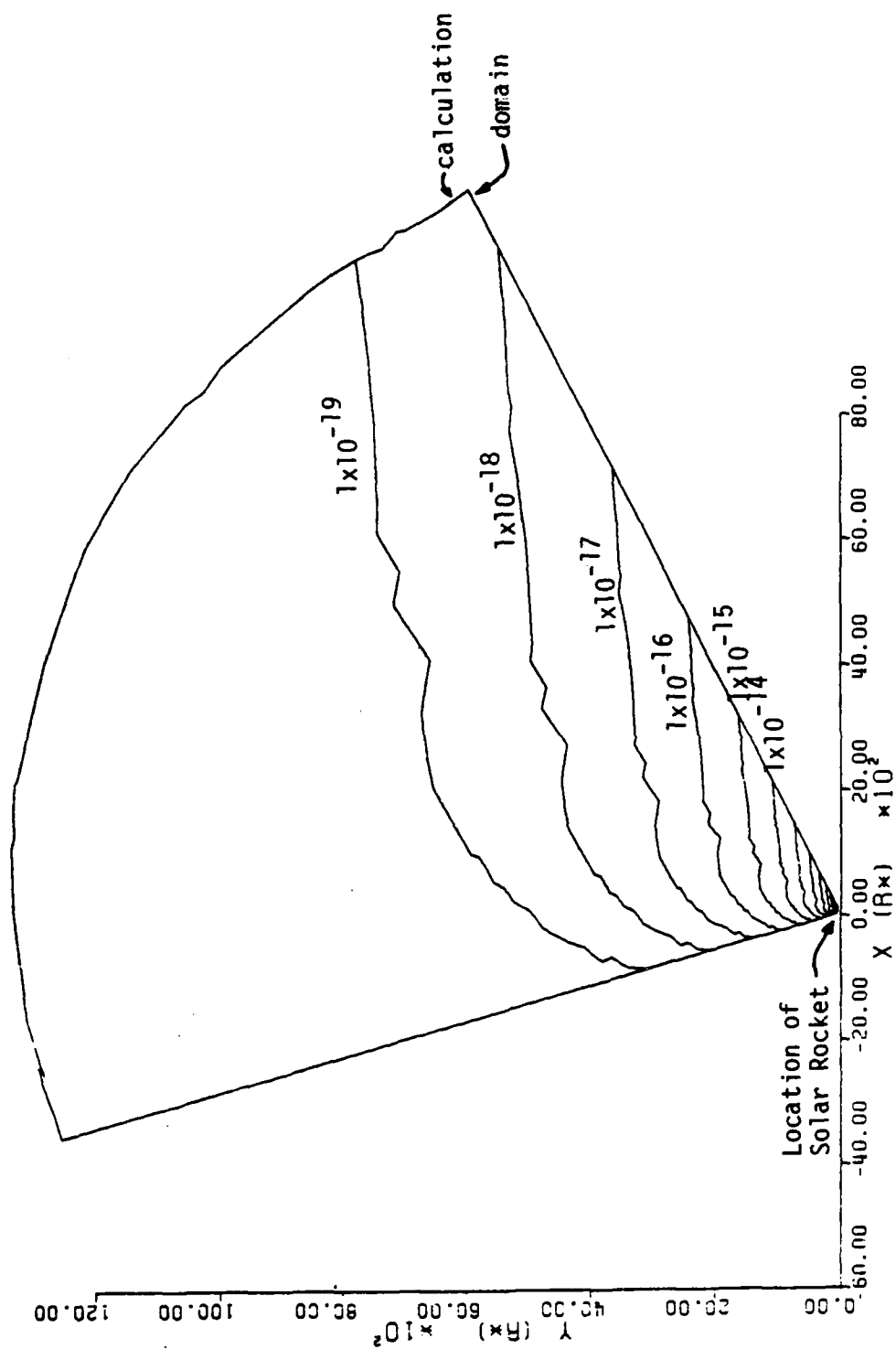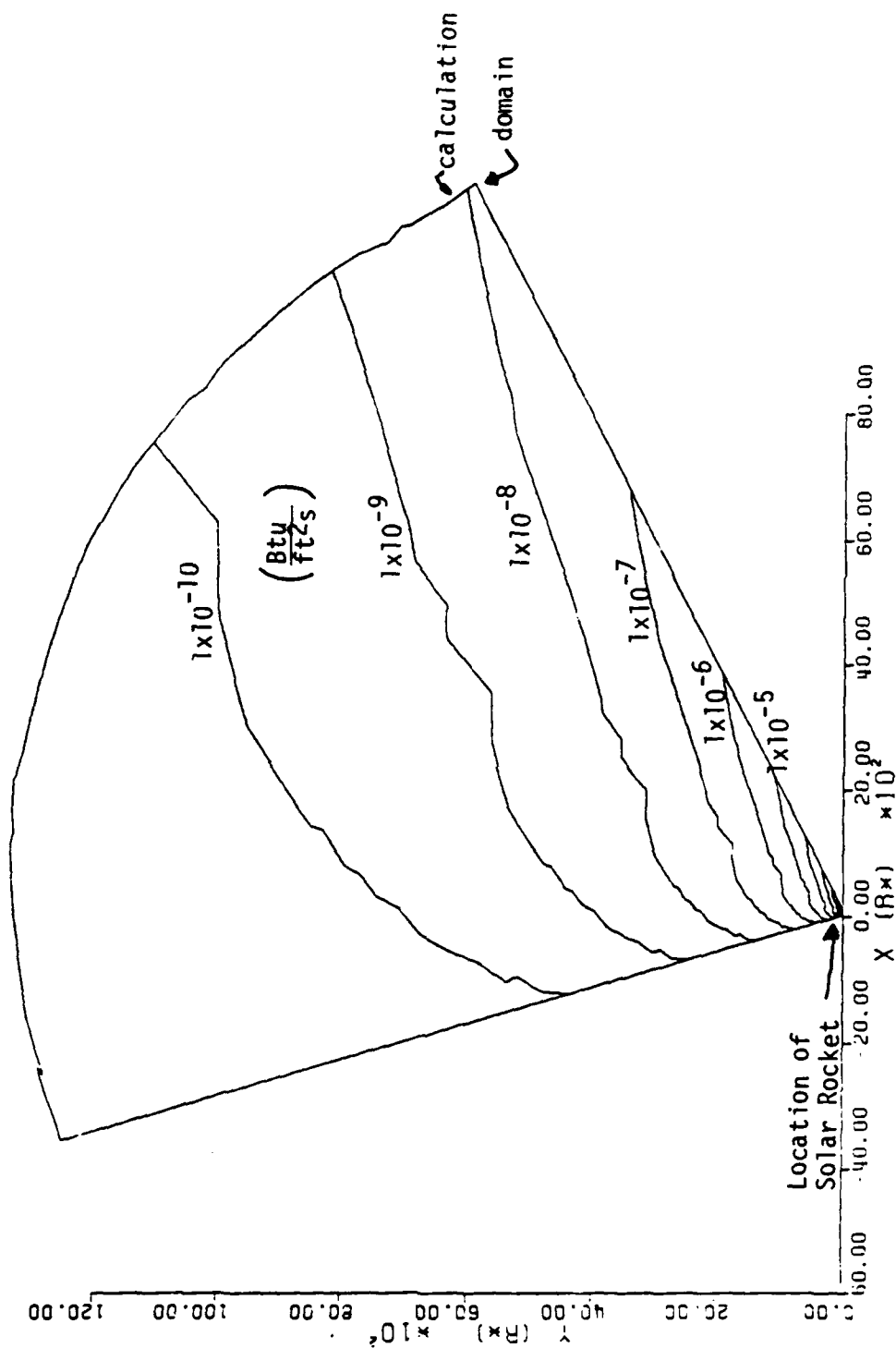Fig. 43. Pressure contours of farfield plume of Case R41

107

Fig. 44. Heat transfer effect contours of farfield plume of Case B41

108

Figures 46a, b and c give the pressure distribution on the collector for the bell-shaped nozzle with a 50 psia chamber pressure. Results for the 100:1 area ratio nozzle are on Fig. 46a while those for the 200:1 and 500:1 cases are on Figs. 46b and c, respectively. Results for all five thrust levels are shown on each figure. All three of these figures show that the pressure loading on the nozzle gets higher as the thrust level is reduced. This shows the effect of the thicker boundary layer in the lower thrust nozzles on collector impingement. Comparison between the three parts of Fig. 46 shows that higher expansion ratio nozzles also lead to increased pressure loading on the collector. This effect is most noticeable for the lower thrust nozzles where the increased nozzle length has the most effect on boundary layer growth.

Corresponding heat flux results for this 50 psia case are presented on Fig. 47a, b, and c. Similar effects of nozzle Reynolds number are seen for the heat flux as were noted for the pressure.

Results for a chamber pressure of 100 psia are shown on Figs. 48 and 49. Figure 48 shows the pressure loading while Fig. 49 shows the heat transfer. Here, the effect of Reynolds number is even smaller than it was for the 50 psia case. Comparison between Figs. 46 and 48 shows the pressure loading on the mirror is considerably lower with the 100 psia chamber pressure than the 50 psia chamber pressure. The reason for this is primarily because of size scaling. Because the thrust levels (and the energy requirements) of the two different chamber pressure nozzles are the same, the collectors are both the same physical size in dimensional

solar
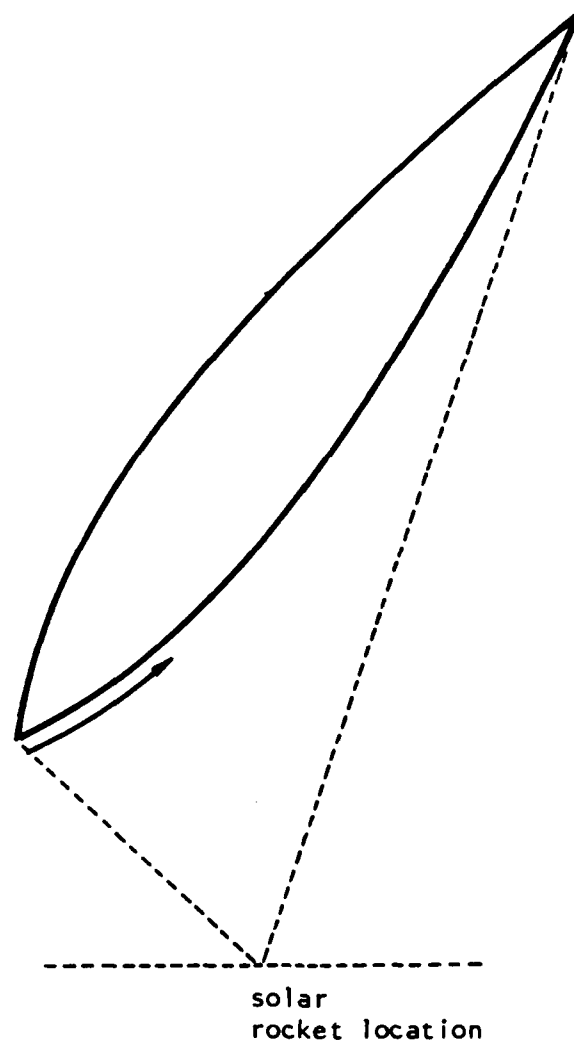rocket location

Fig. 45.   The arc-length distance measured from
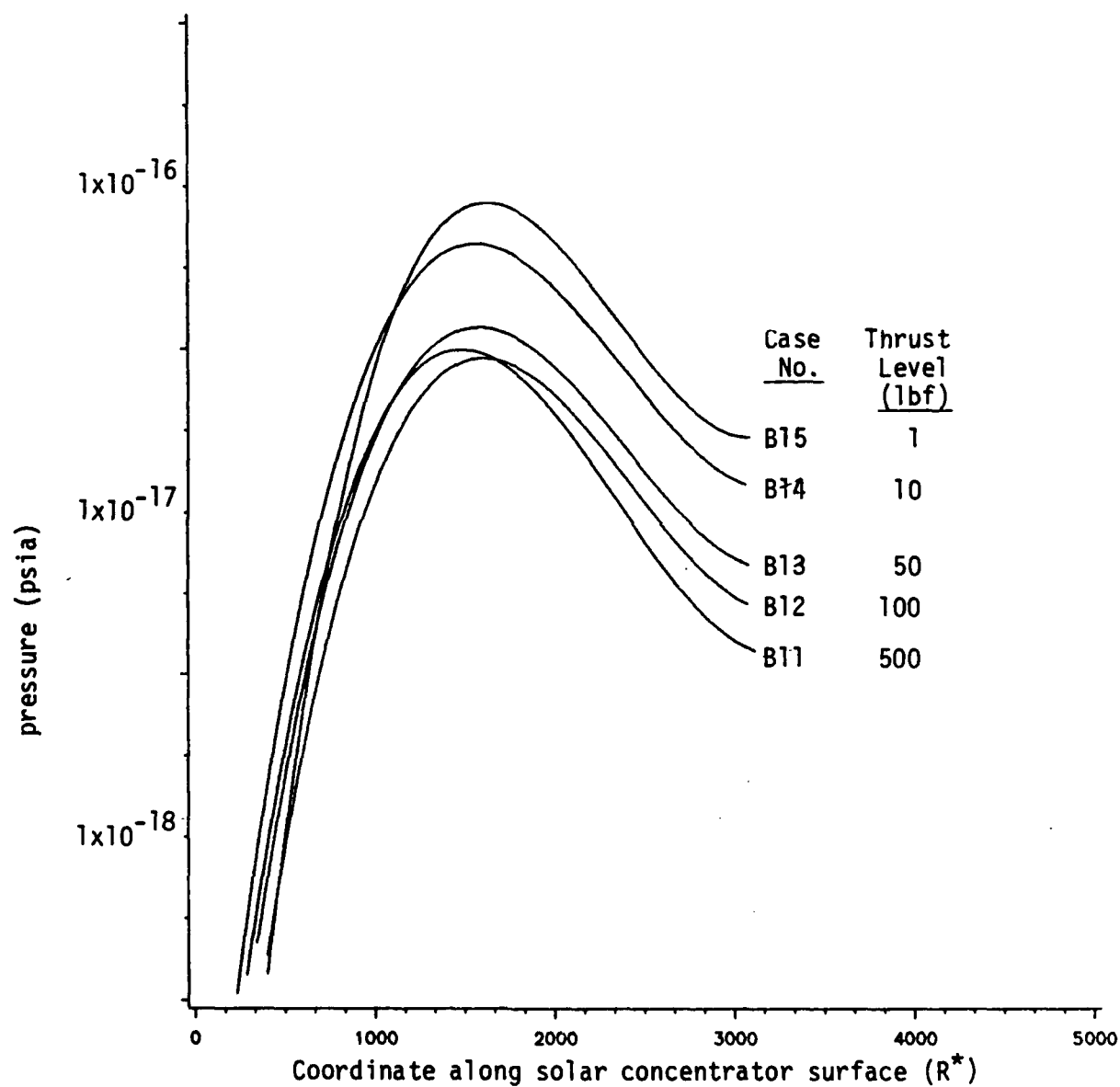the front, inner point on the collector

Fig. 46a.   Pressure distribution on solar concentrator of
            Case Group B1. (Bell-shaped nozzle, area ratio 100:1,
            P_o=50 psia, T_o=5000R)

111

Fig. 46b. Pressure distribution on solar concentrator of Case Group B2 (Bell-shaped nozzle, area ratio 200:1, P_0=50 psia, T_0=5000R)

112

Fig. 46c. Pressure distribution on the solar concentrator of Case Group B3 (Bell-shaped nozzle, area ratio 500:1, P_o=50 psia, T_o=5000R)
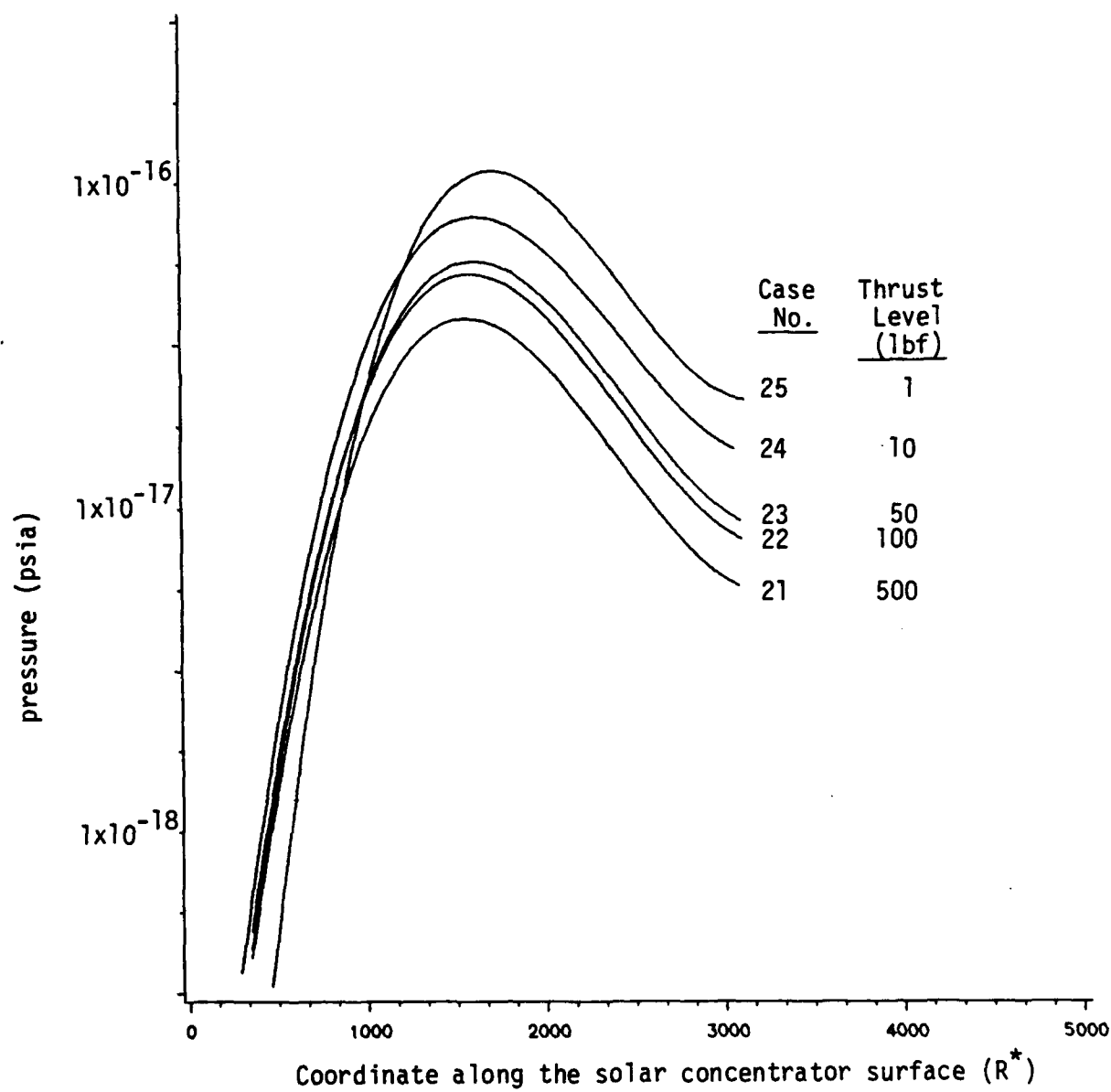
113

Fig. 47a. Heat transfer effect on solar concentrator for Case Group B1 (Bell-shaped nozzle, area ratio 100:1, P_o=50 psia, T_o=5000 R)

114

Fig. 47b. Heat transfer effect on the solar concentrator of
Case Group B2 (Bell-shaped nozzle, area ratio 200:1,
P_o=50 psia, T_o=5000 R)

115

Fig. 47c. Heat transfer effect on the solar concentrator surface of Case Group B3 (Bell-shaped nozzle area ratio 500:1, P_0=50 psia, T_0=5000 R)

The y-axis is labeled "heat transfer (Btu/ft²s)" with values 1×10^{-7}, 1×10^{-8}, and 1×10^{-9}.

The x-axis is labeled "Coordinate along the solar concentrator surface (R*)" with values 0, 1000, 2000, 3000, 4000, 5000.

Legend:

Case No.	Thrust Level (lbf)
B35	1
B34	10
B33	50
B32	100
B31	500

Fig. 48a. Pressure distribution on the solar concentrator surface of Case Group B4 (Bell-shaped nozzle, area ratio 100:1, P_o=100 psia, T_o=5000 R)
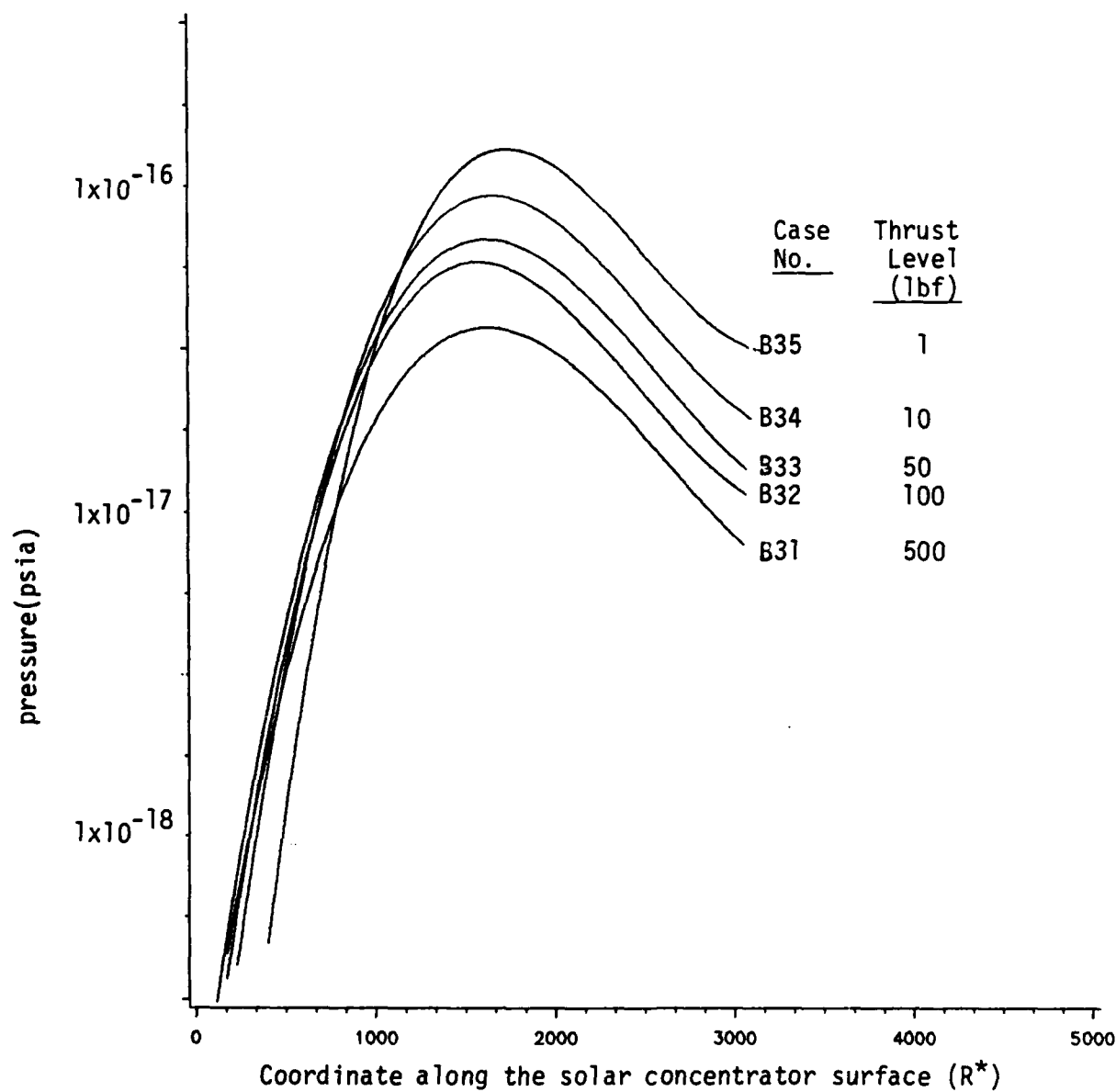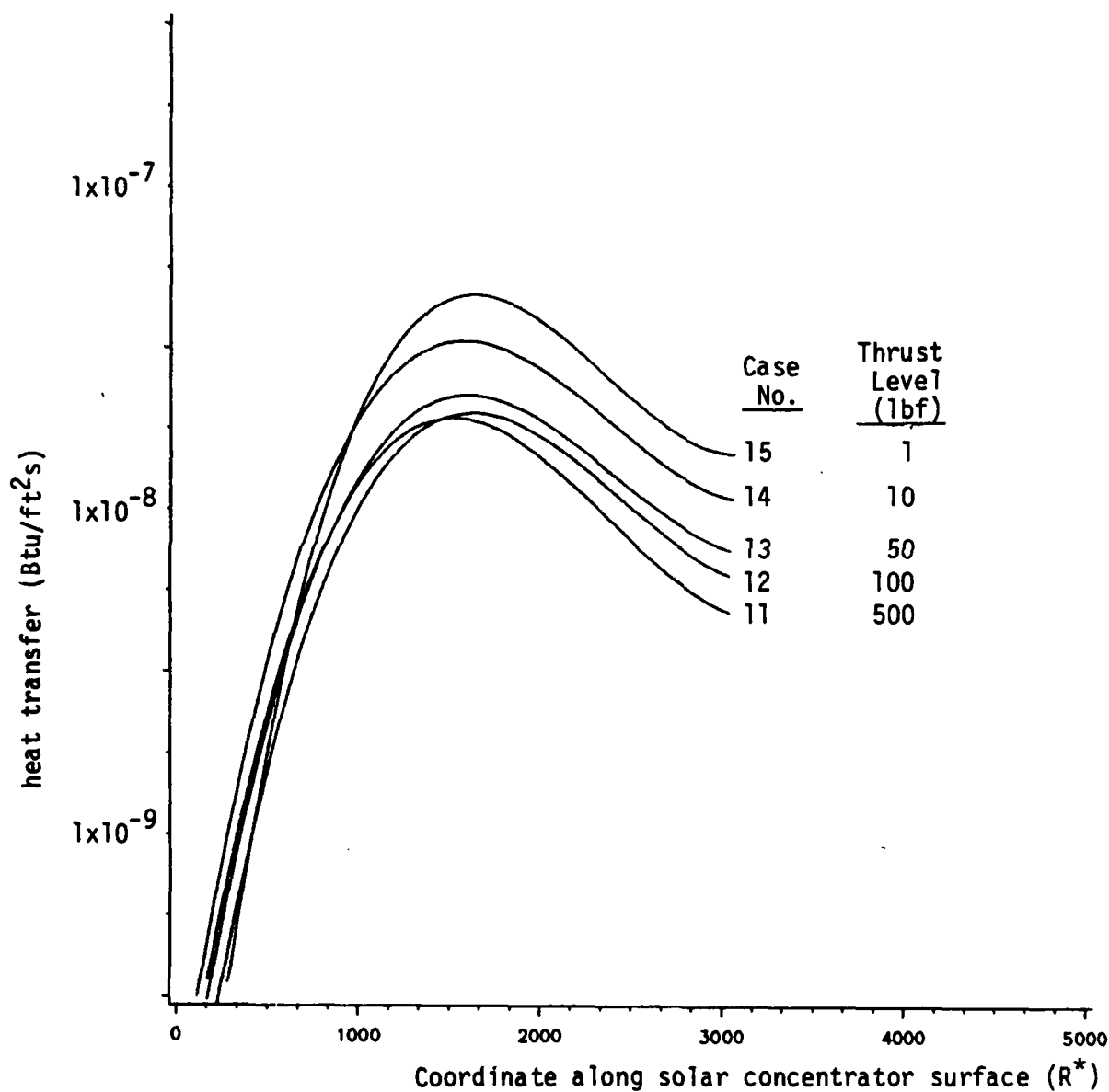
117

Fig. 48b. Pressure distribution on the solar concentrator surface of Case Group B5 (Bell-shaped nozzle, area ratio 200:1, P_0=100 psia, T_0=5000 R)

118

Fig. 48c. Pressure distribution on the solar concentrator surface of Case Group B6 (Bell-shaped nozzle, area ratio 500:1, $P_0=100$ psia, $T_0=5000$ R)

Fig. 49a. Heat transfer effect on the solar concentrator surface of Case Group B4 (bell-shaped nozzle, area ratio 100:1, P_o=100 psia, T_o=5000 R)
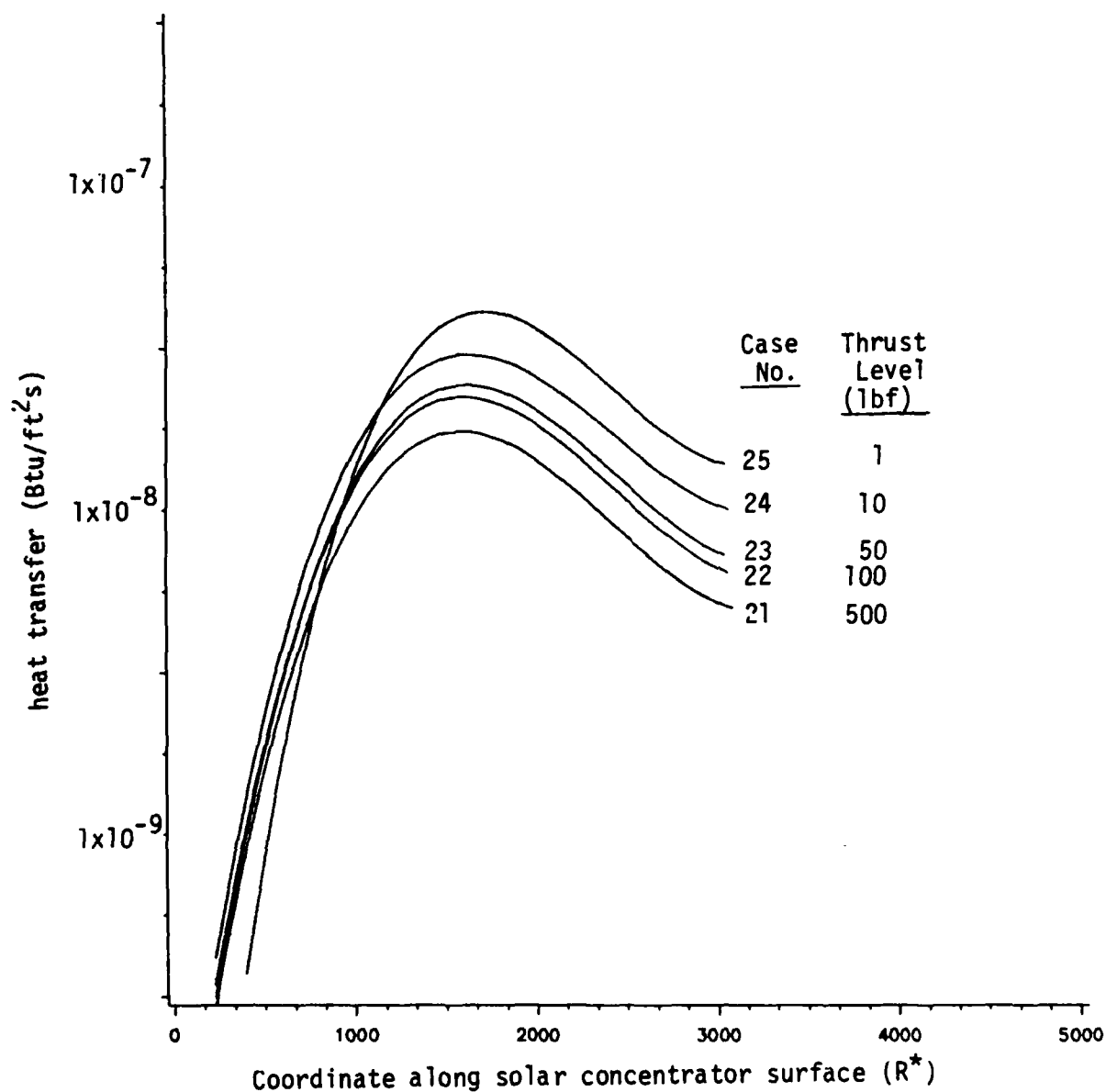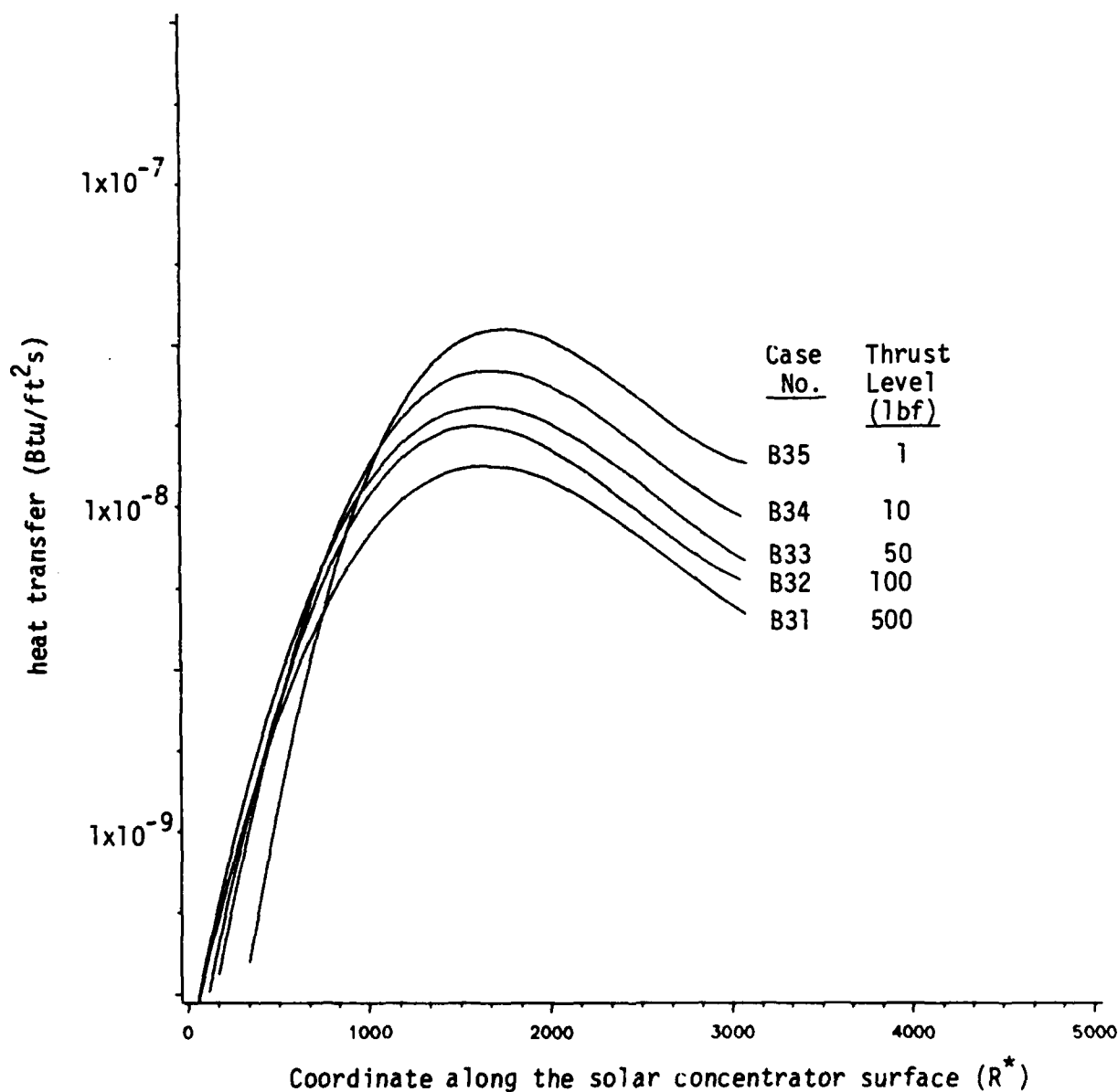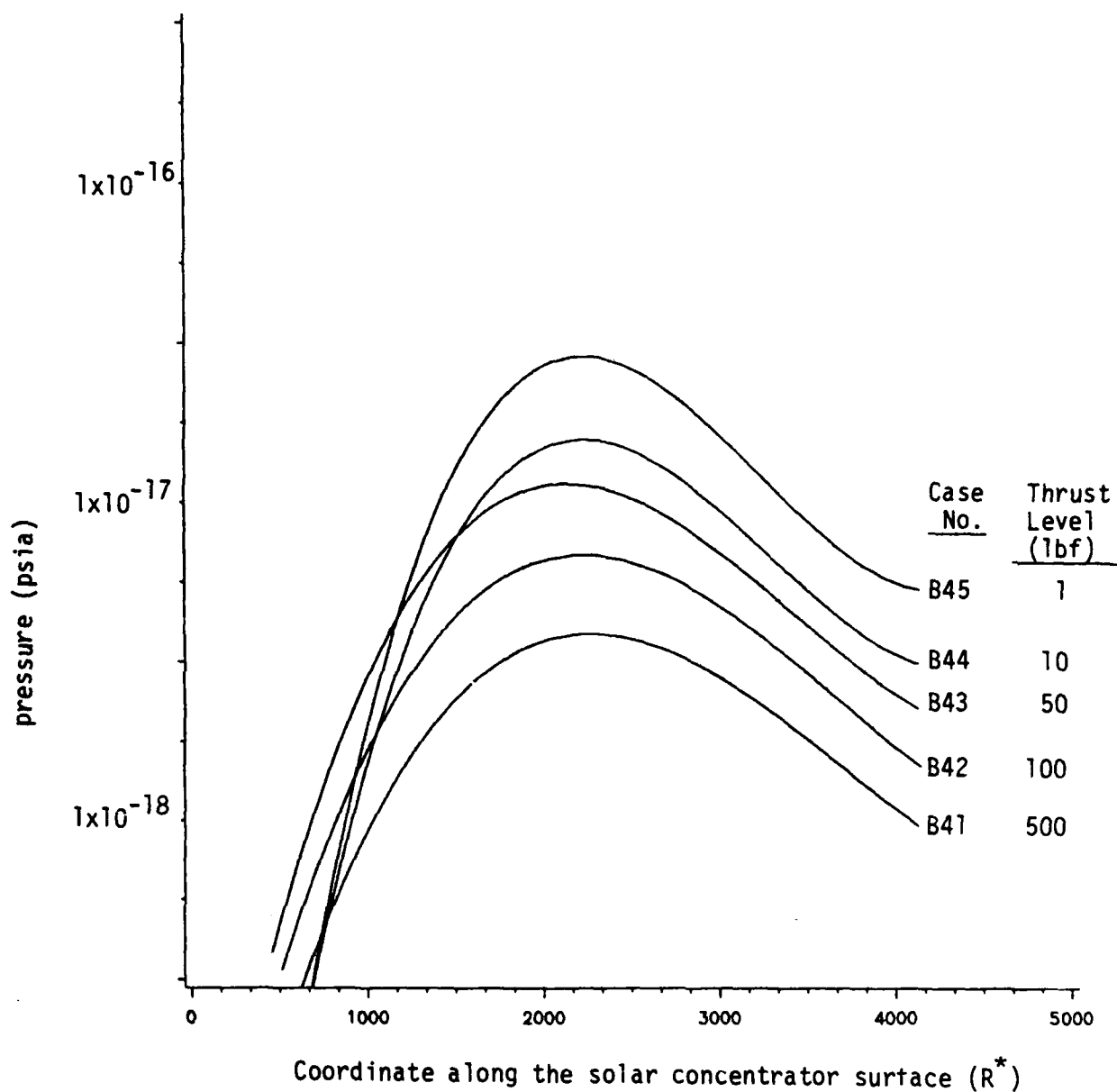
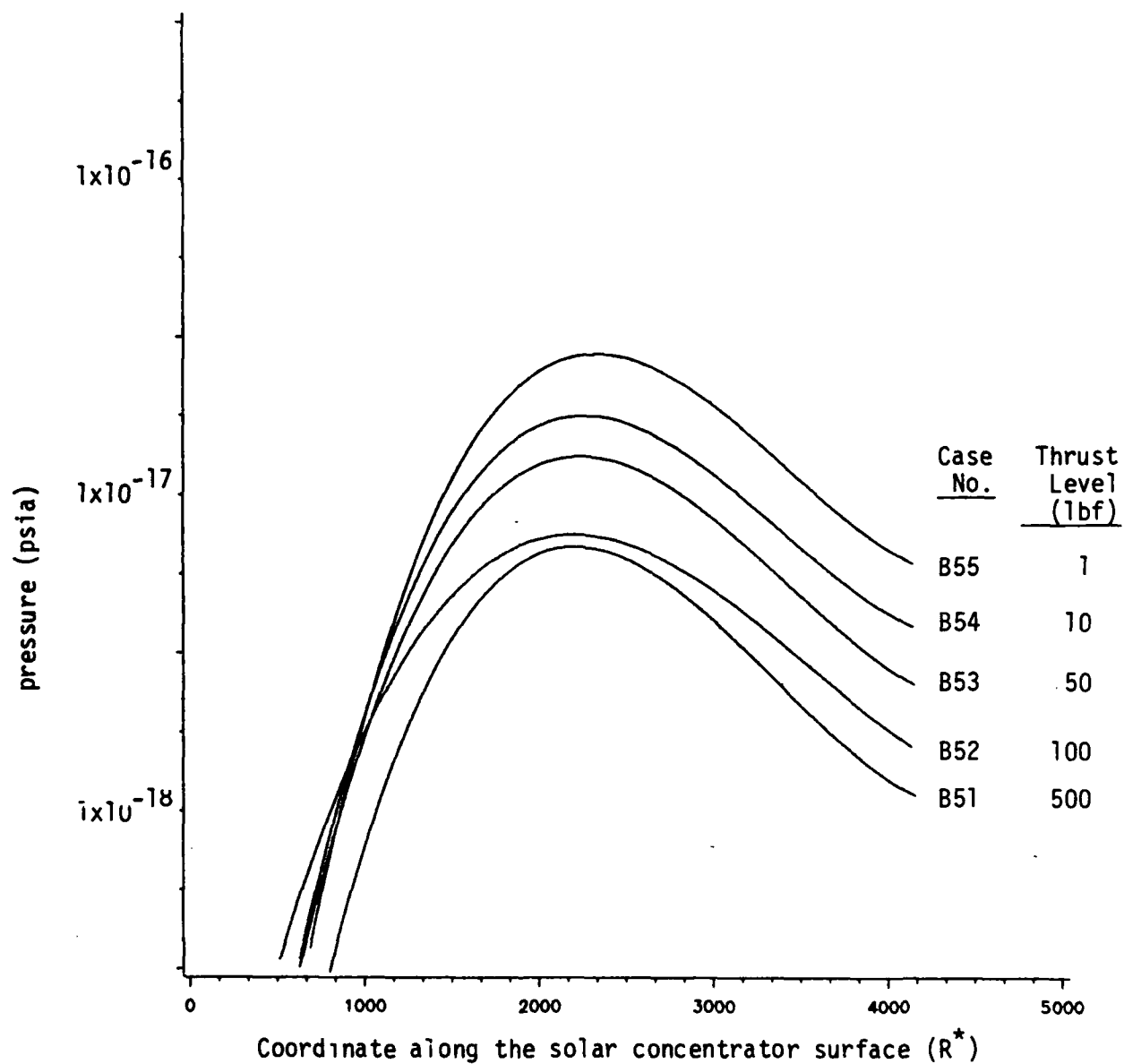Fig. 49b. Heat transfer effect on the solar concentrator surface
of Case Group B5 (bell-shaped nozzle, area ratio 200:1,
P_0=100 psia, T_0=5000 R)

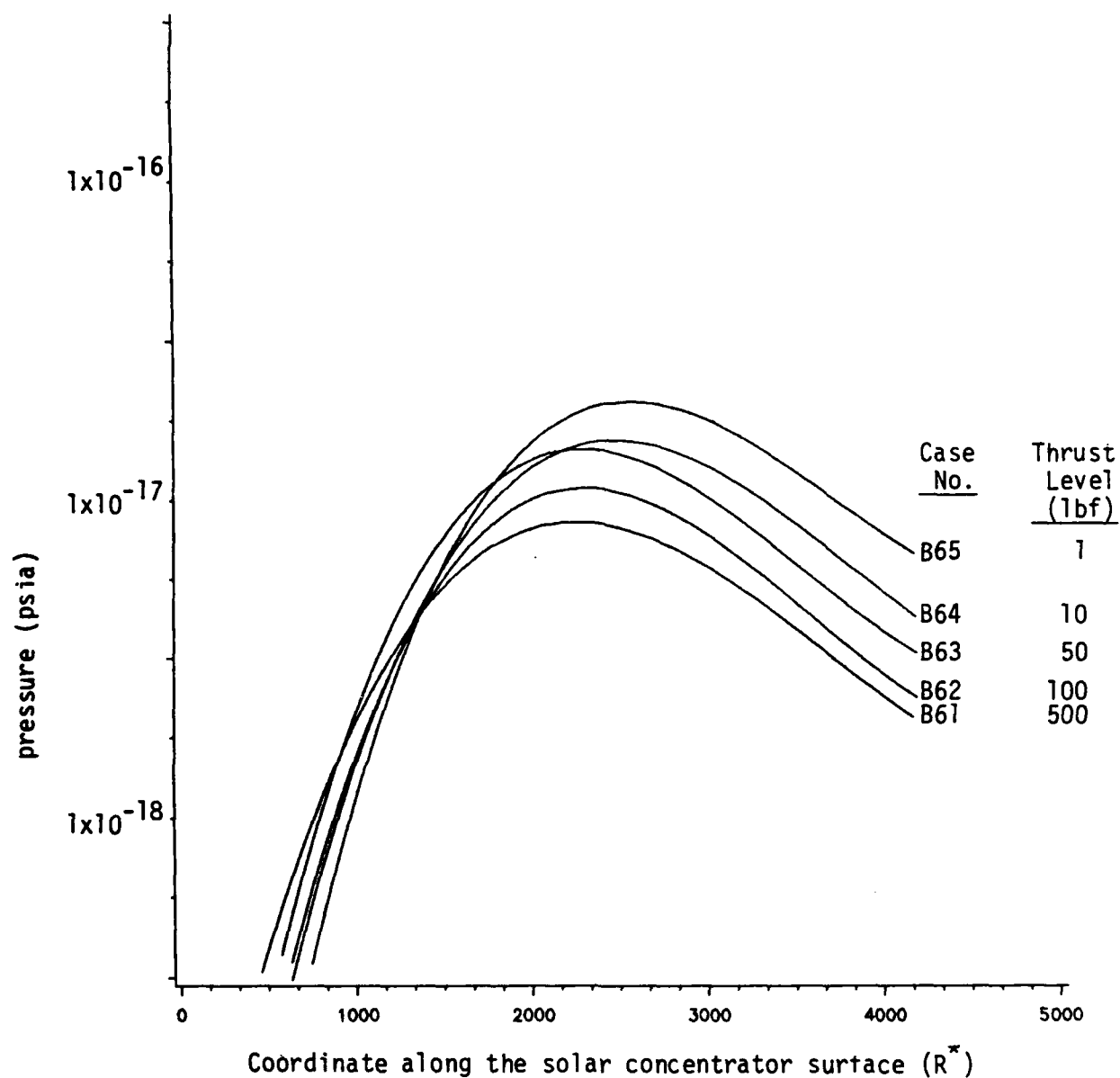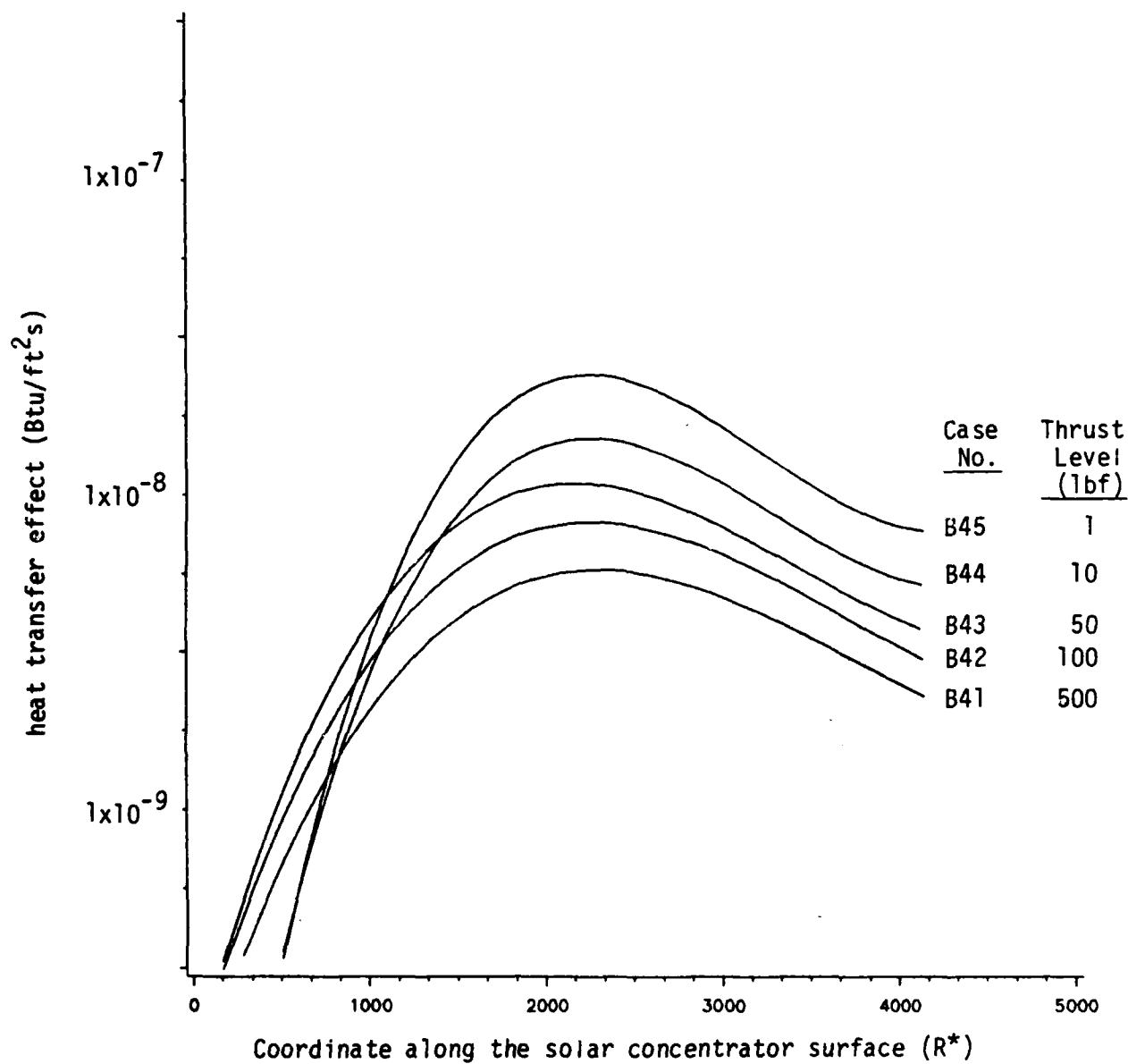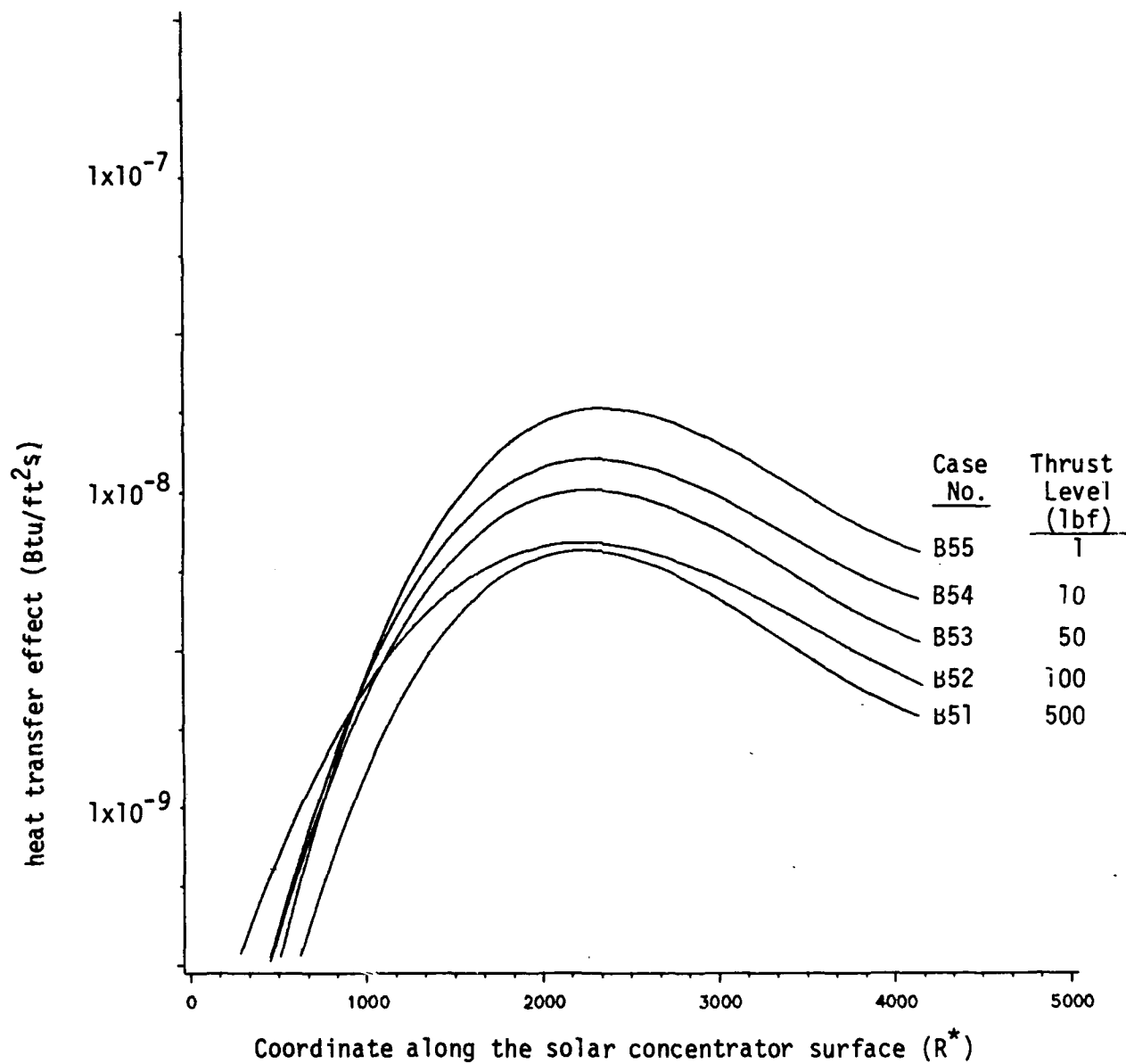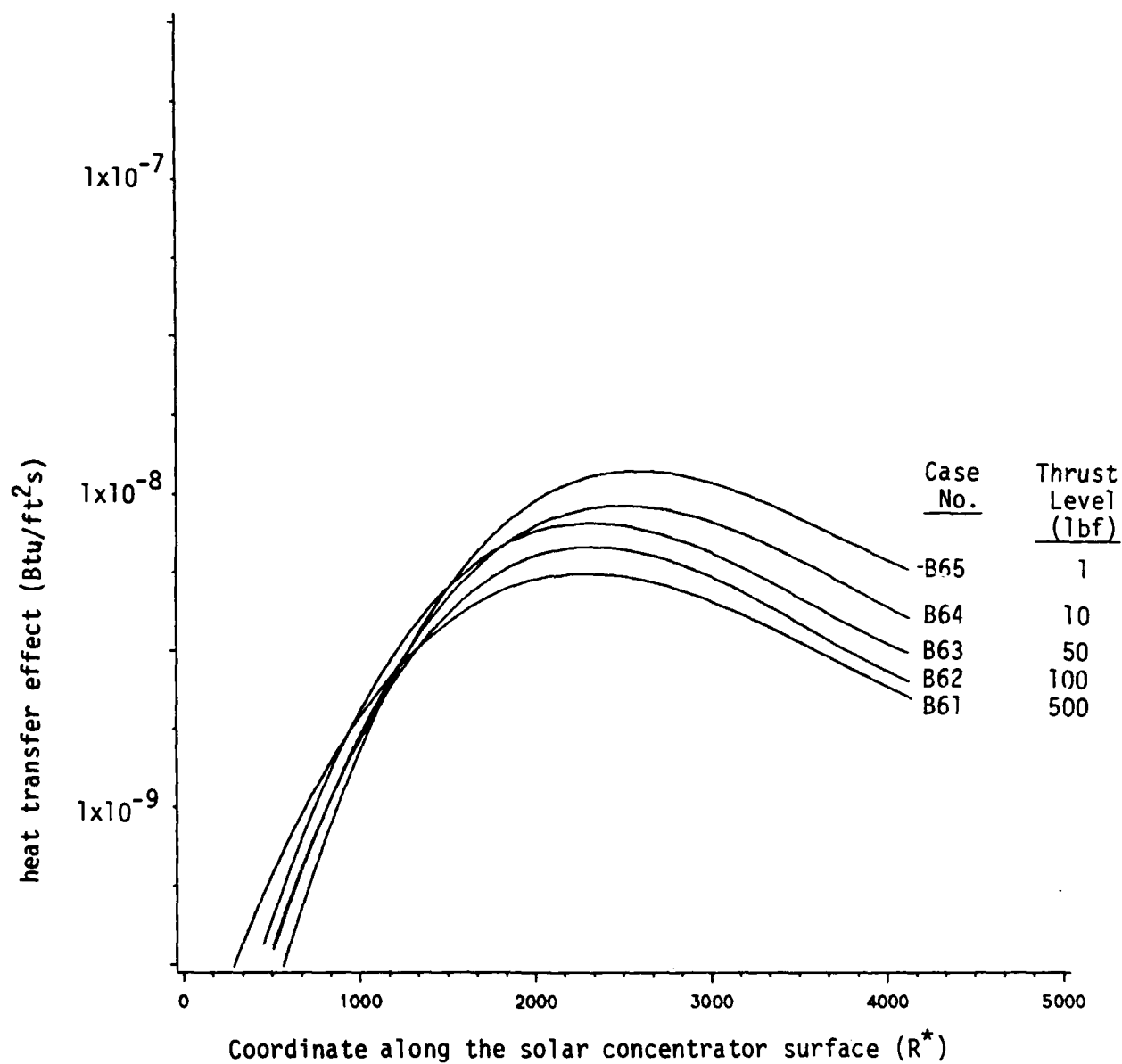Fig. 49c. Heat transfer effect on the solar concentrator surface of Case Group B6 (bell-shaped nozzle, area ratio 500:1, P_o=100 psia, T_o=5000 R)

122

coordinates. In nondimensional coordinates, the collector for the 100 psia nozzle is larger because its throat radius is $1/\sqrt{2}$ times the throat radius of the 50 psia case. To a first approximation, the pressure fields decay at the same rate in nondimensional coordinates in the two flowfields, although the pressure level is a factor of two higher for the 100 psia nozzle. The only difference in nondimensional decay rates is because of the difference in boundary layer characteristics of the two nozzles (which is small). Thus, because the collector is farther away in nondimensional coordinates for the high pressure nozzle, and because the collector is placed in the fringe of the plume where the pressure is falling off very steeply, the high pressure nozzle has considerably smaller pressure loadings. Comparisons of the heat flux rates for the two nozzles (Fig. 47 and 49) show analogous conclusions.

The corresponding plume impingement calculations for the conical nozzle are shown on Fig. 50 to 53. Figures 50a and b show the pressure distribution for the 50 psia conical nozzle case and for the 500 and 1 lb_f thrust levels, while Fig. 51 shows the corresponding heat transfer results. Figure 52 shows pressure loadings for the 100 psia case while Fig. 53 shows heat flux levels for the higher chamber pressure case. Again, there is a noticeable effect of thrust level and chamber pressure level on the plume/mirror impingement levels. Comparisons with the earlier figures show the nozzle geometry has almost no effect on plume-mirror impingement. Consequently, it appears the nozzle can be designed almost solely on the basis of its thrust-specific impulse performance, and without regard to the impingement problem.

Fig. 50a. Pressure distribution on the solar concentrator surface of Case Group C1 (conical nozzle, area ratio 100:1, P_0=50 psia, T_0=5000 R)
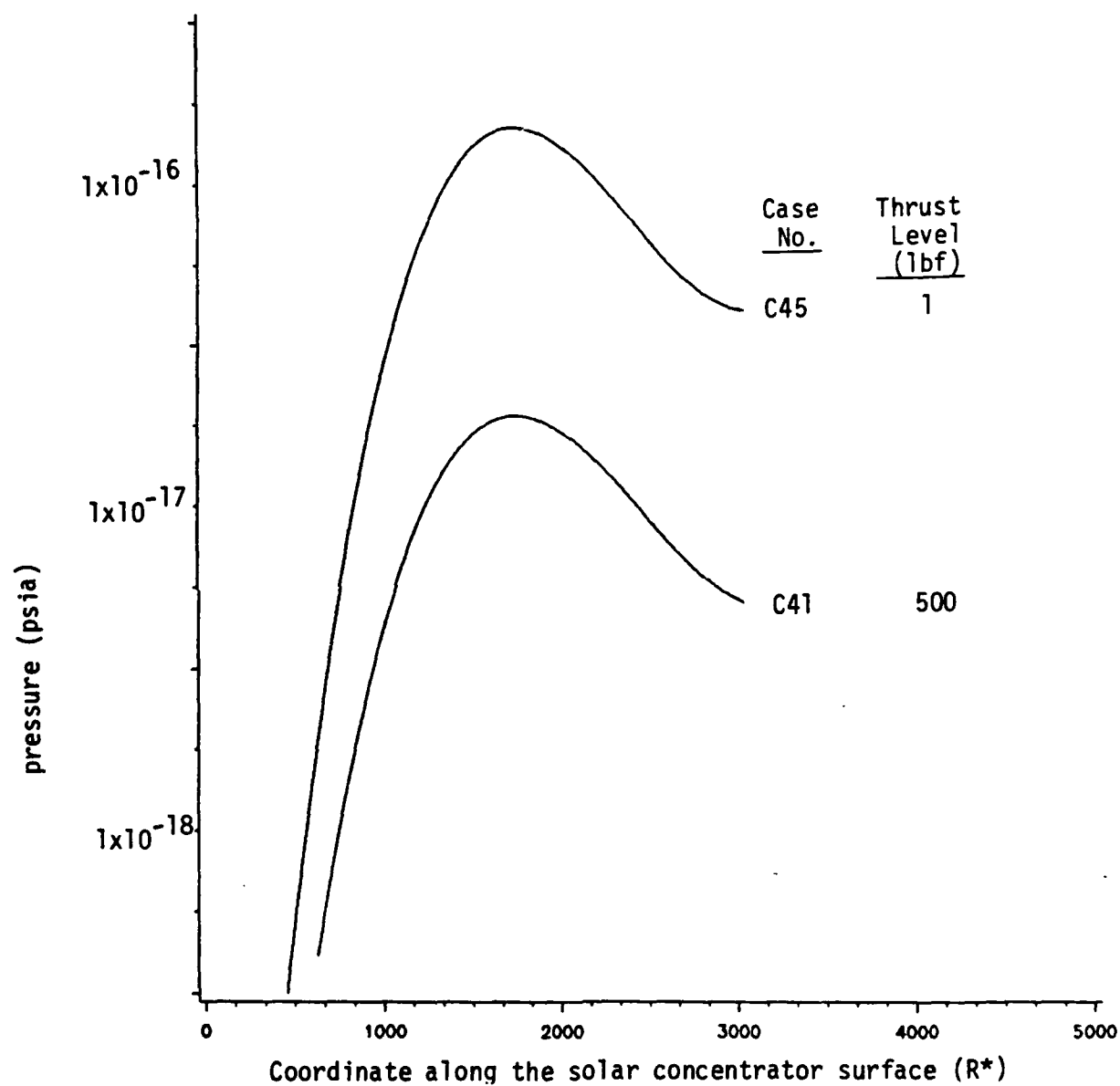
Fig. 50b. Pressure distribution on the solar concentrator surface of Case Group C4 (conical nozzle, area ratio=500:1, P_0=100 psia, T_0=5000 R)

Fig. 51a. Heat transfer effect on the solar concentrator surface of Case Group C3 (conical nozzle, area ratio=100:1, P_0=50 psia, T_0=5000 R)

126

Fig. 51b. <u>Heat transfer effect on the solar concentrator surface of Case Group C3 (conical nozzle, area ratio 500:1, P_o=50 psia, T_o=5000 R)</u>
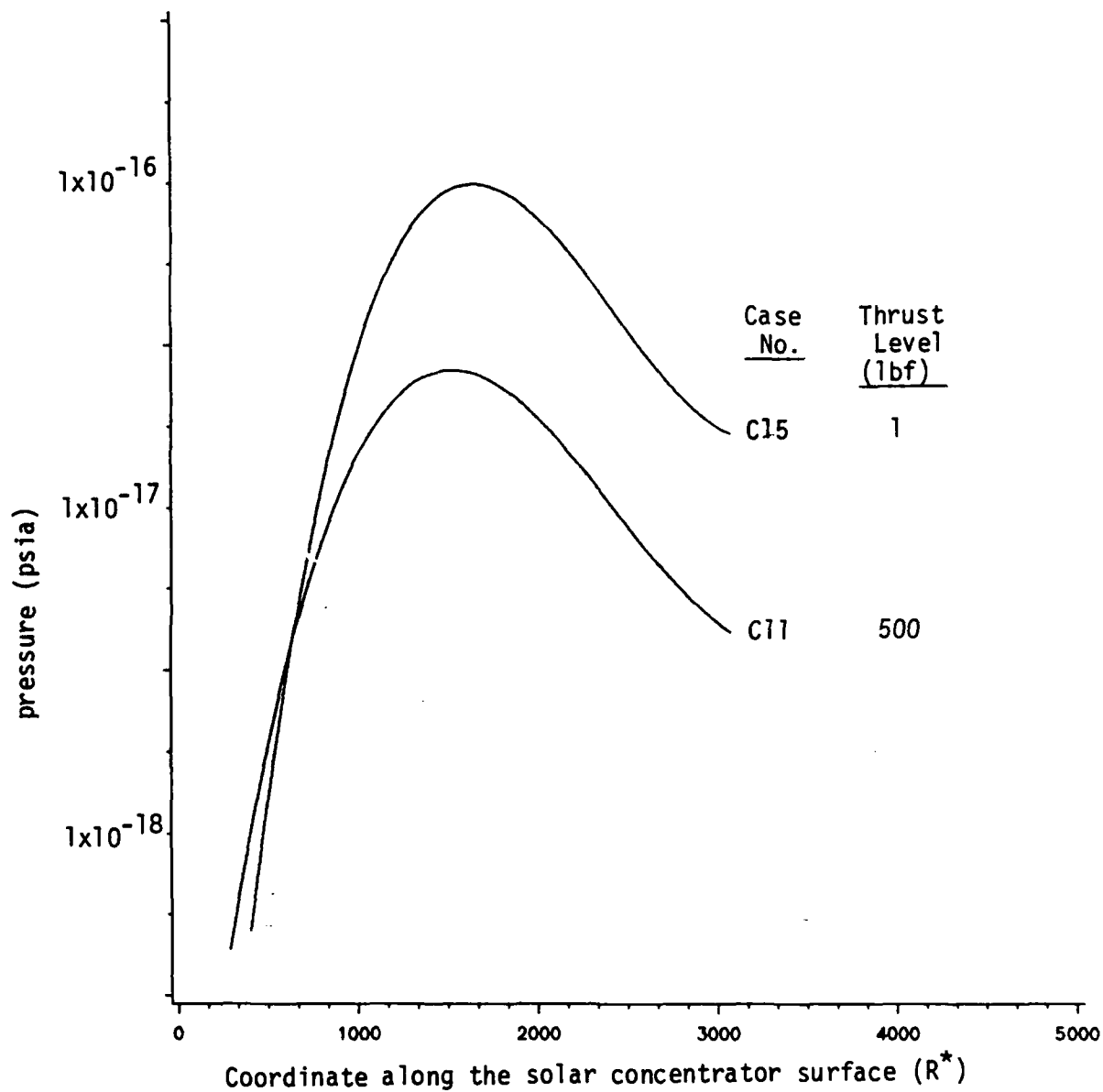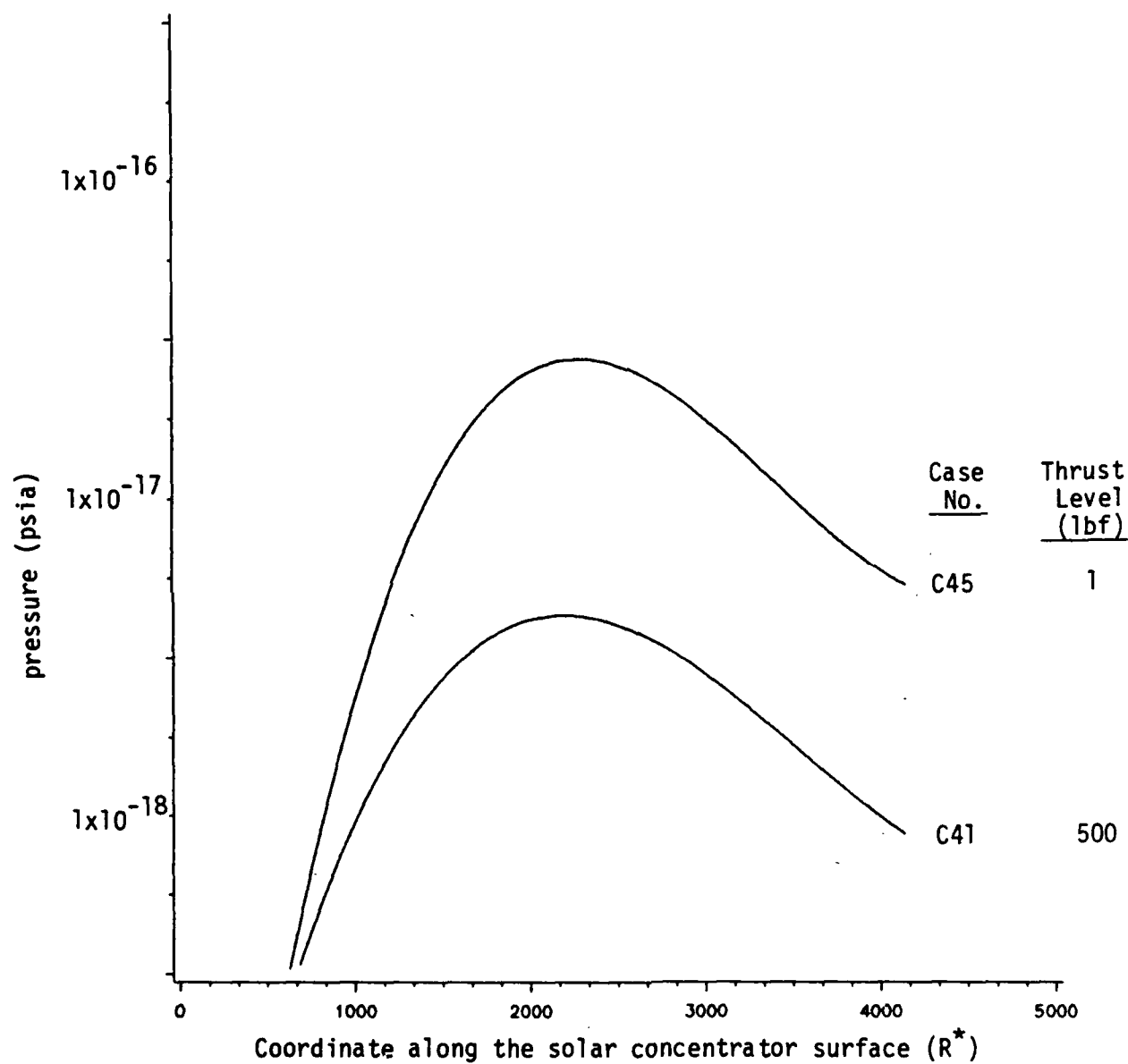
Fig. 52a. Pressure distribution on the solar concentrator surface of Case Group C4 (conical nozzle, area ratio 100:1, P_o=100 psia, T_o=5000 R)
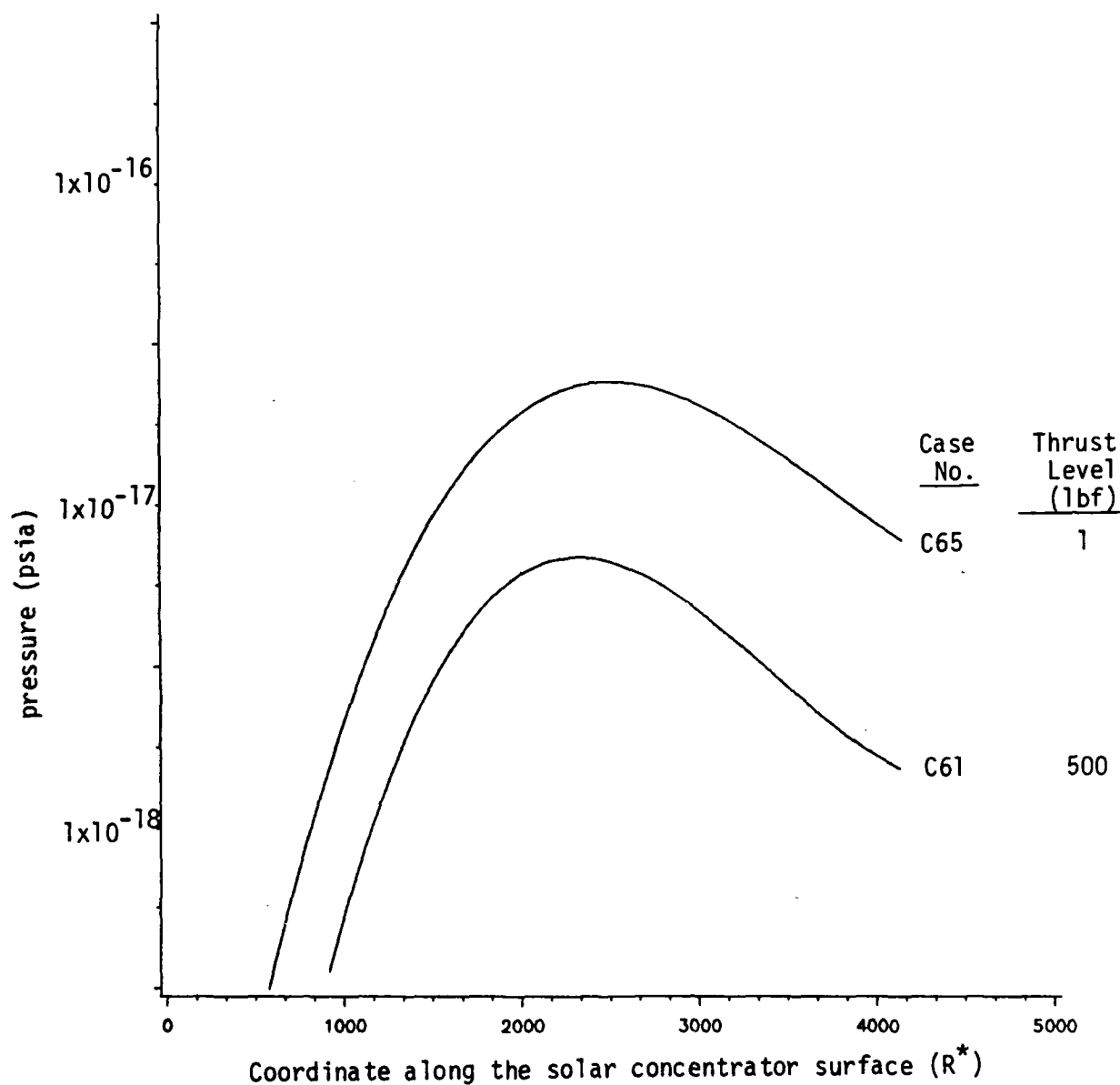
Fig. 52b. Pressure distribution on the solar concentrator surface of Case Group C6 (conical nozzle, area ratio=500:1, P_0=100 psia, T_0=5000 R)
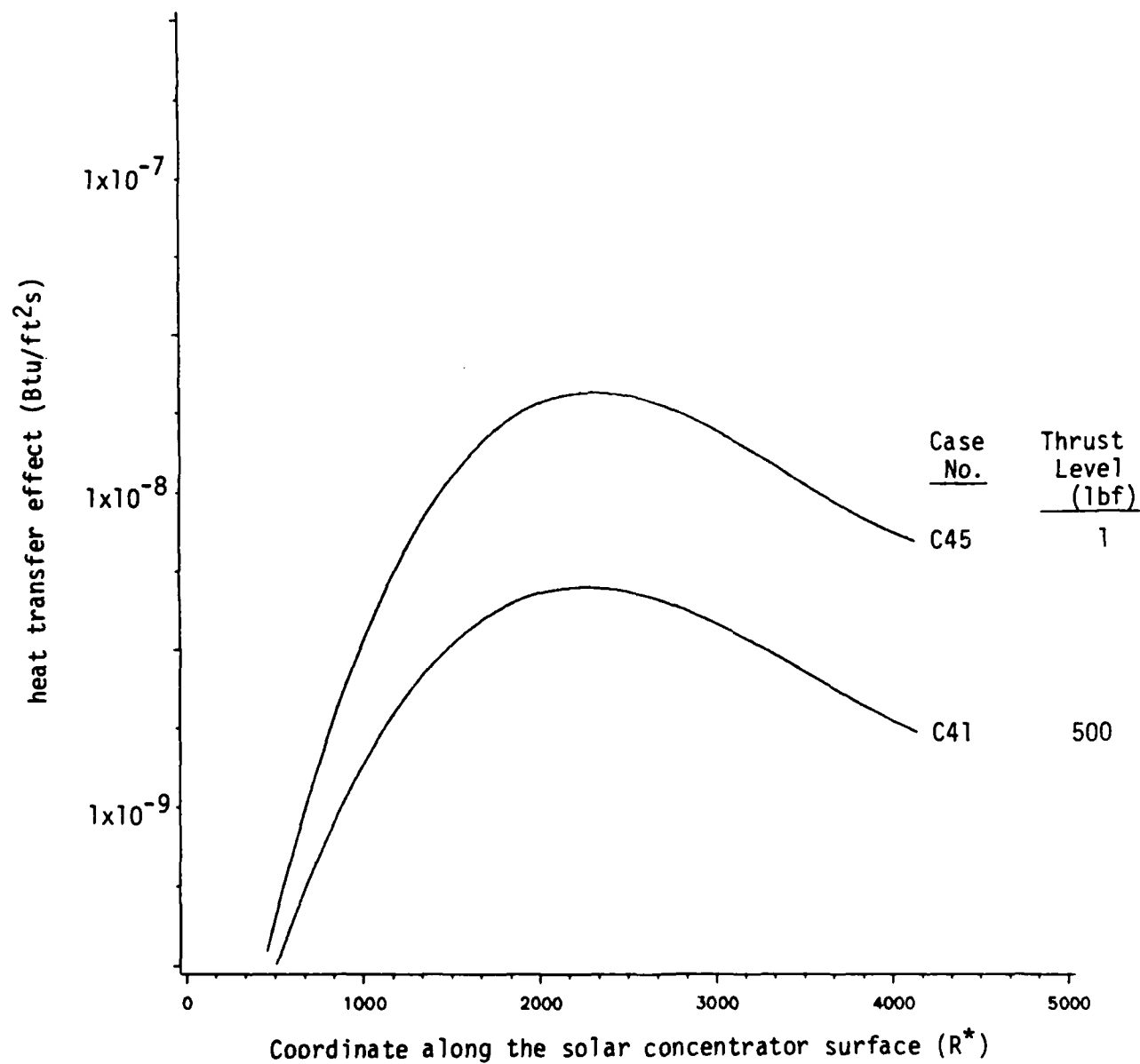
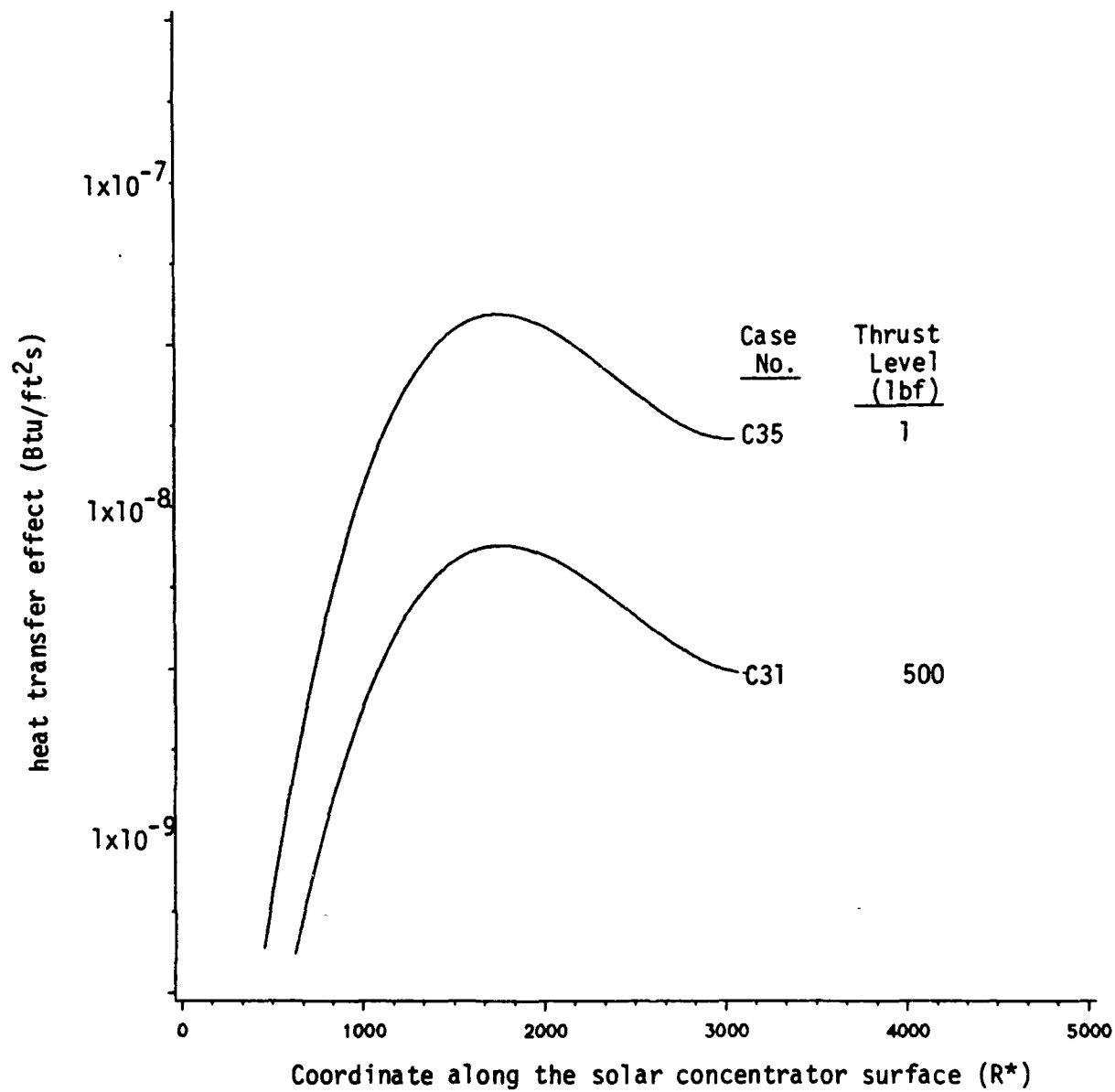Fig. 53a. Heat transfer effect on the solar concentrator surface of Case Group C4 (conical nozzle, area ratio-100:1, P_o=100 psia, T_o=5000 R)
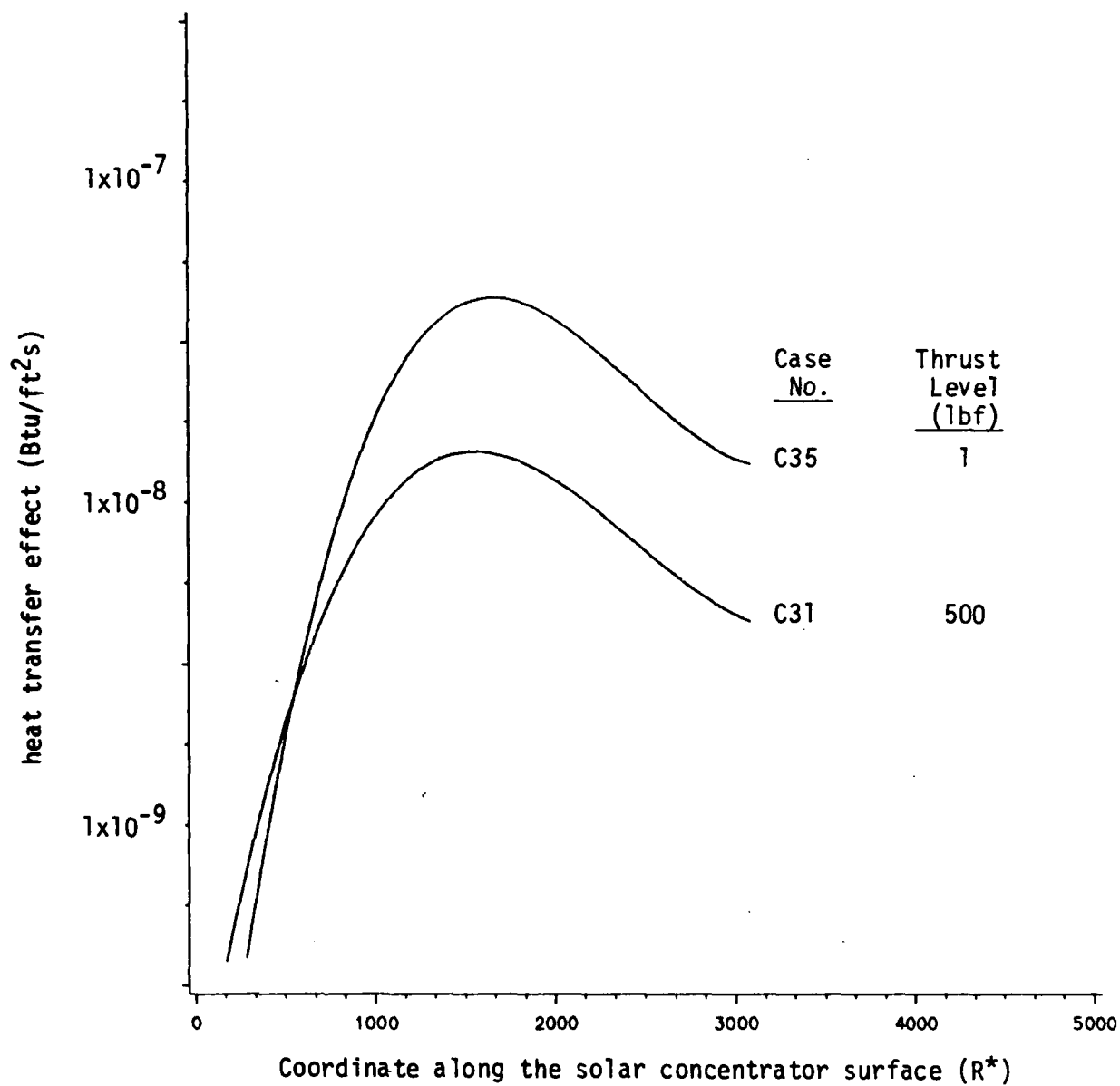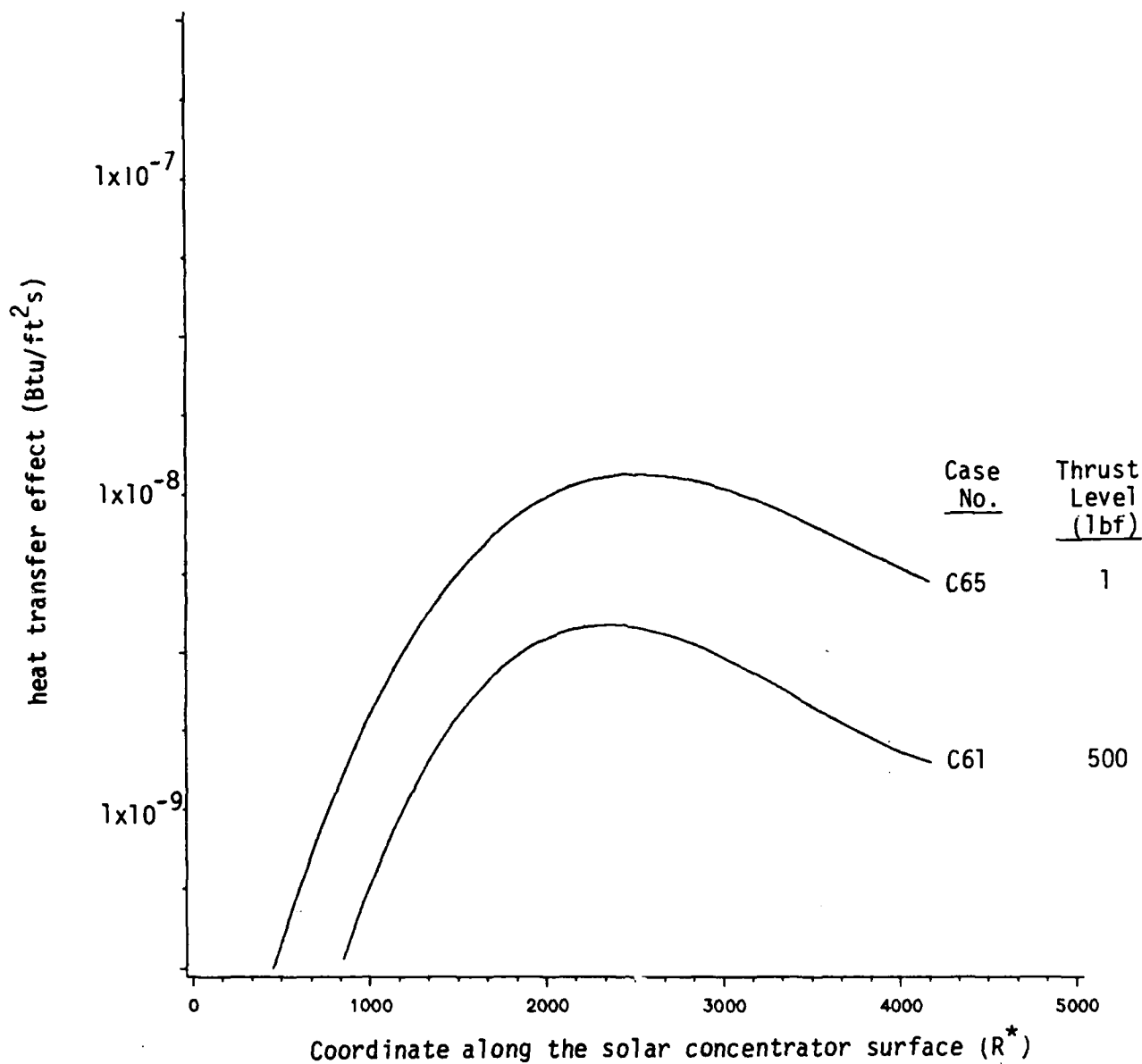
Fig. 53b. <u>Heat transfer effect on the solar concentrator surface of Case Group C6 (conical nozzle, area ratio=500:1, P_o=100 psia, T_o=5000 R)</u>

The level of impingement will be affected primarily by the distance away from the nozzle and the nozzle Reynolds number characteristics.

Finally, we note that the level of the indicated plume-mirror interactions is quite small. Reference to Figures like 40 and 41 and 43 and 44, however, show that the pressure and heat flux contour plots are very steep in the vicinity of the collector and that relocation of the collectors could raise those interactions significantly. Consequently, the design and placement of the collectors must be done with care.

REFERENCES

1. Shoji, J. M., "Potential of Advanced Solar Thermal Propulsion", <u>Orbit-Raising and Maneuvering Propulsion: Research Status and Needs</u>, <u>Progress in Astronautics and Aeronautics</u>, Vol. 89, pp. 30-47.

2. Etheridge, F. G., <u>Solar Rocket System Concept Analysis</u>, Final Technical Report AFRPL-TR-79-79, Nov. 1979.

3. Mattick, A. T., "Absorption of Solar Radiation by Alkali Vapors", <u>Radiation Energy Conversion in Space</u>, <u>Progress in Astronautics and Aeronautics</u>, Vol. 61, pp. 159-171.

4. Perry, F. J., <u>Solar Thermal Propulsion: An Investigation of Solar Radiation Absorption in a Working Fluid</u>, Final Technical Report AFRPL-TR-84-032, June 1984.

5. Selph, C. C. and Naujokas, G. J., <u>The AFRPL Solar-Thermal Rocket Activities</u>, Paper presented at JANNAF Conference, New Orleans, LA, March 1984.

6. Patch, R. W., <u>Thermodynamic Properties and Theoretical Rocket Performance of Hydrogen to 100,000K and 0.01325 x 10^8 N/m^2</u>, NASA-SP-3069, NASA/Lewis Research Center, 1971.

7. Hoffman, R. J., Hetrick, M. A. Jr., Nickerson, G. R., and Jarossy, F. J., <u>Plume Contamination Effects Prediction: CONTAM III Computer Program - Volume I, Contaminant Production and Combustion Processes</u>, Science Applications, Inc., AFRPL-TR-82-033, December 1982.

8. Hoffman, R. J., Hetrick, M. A. Jr., Nickerson, G. R. and Jarossy, F. J., <u>Plume Contamination Effects Prediction: CONTAM III Computer Program - Volume II, Contaminant Transport and Chemical Kinetics</u>, Science Applications, Inc., AFRPL-TR-82-033, December 1982.

9. Hoffman, R. J., Hetrick, M. A. Jr., Nickerson, G. R., and Jarossy, F. J., <u>Plume Contamination Effects Prediction: CONTAM III Computer Program - Volume III, Contaminant Deposition and Surface Effects</u>, Science Applications, Inc., AFRPL-TR-82-033, December 1982.

10. Back, L. H., Massier, P. F., and Cuffel, R. F., "Flow Phenomena and Convective Heat Transfer in a Conical Supersonic Nozzle", <u>J. Spacecraft</u>, Vol. 4, No. 8, pp. 1040-1047, 1967.

11. Back, L. H., Massier, P. F., and Gier, H. L., "Convective Heat Transfer in a Convergent-Divergent Nozzle", <u>Int. J. Heat Mass Transfer</u>, Vol. 7, pp. 549-568, 1964.

12. Back, L. H., Cuffel, R. F., and Massier, P. F., "Laminarization of a Turbulent Boundary Layer in Nozzle Flow-Boundary Layer and Heat Transfer Measurements with Wall Cooling", _J. of Heat Transfer_, p. 333, August 1970.

13. Moretti, P. M., and Kays, W. M., "Heat Transfer to a Turbulent Boundary Layer with Varying Free-Stream Velocity and Varying Surface Temperature-An Experimental Study", _Int. J. of Heat Mass Transfer_, Vol. 8, pp. 1187-1202, 1965.

14. Bird, G. A., "Breakdown of Continuum Flow in Freejets and Rocket Plumes", _Rarefied Gas Dynamics, Progress in Astronautics and Aeronautics_, Vol. 74: Part II, pp. 681-694.

15. Bird, G. A., _Prandtl-Meyer Flow of a Finite Knudsen Number Gas_, Presented at the 7th Australian Hydraulics and Fluid Mechanics Conference, Brisbane, August 18-22, 1980.

16. Bird, G. A., "Breakdown of Translational and Rotational Equilibrium in Gaseous Expansion", _AIAA Journal_, Vol. 88, No. 11, p. 1998, 1970.

17. Merkle, C. L., _Stability and Transition in Boundary Layers_, Flow Research Report 71, Flow Research, Inc., Kent, WA, 1976.

18. Price, J. M. and Harris, J. E., "Computer Program for Solving Compressible Boundary Layer Equations of a Perfect Gas", NASA TM X-2458, Langley Research Center, Hampton, VA, 1972.

19. Lubard, S. C. and Helliwell, W. S., "Calculation of the Flow on a Cone at High Angle of Attack", _AIAA Journal_, Vol. 12, pp. 965-974, December 1974.

20. Rubin, S. G. and Lin, T. C., "A Numerical Method for Three-Dimensional Viscous Flow: Application to the Hypersonic Leading Edge", _J. Comp. Physics_, Vol. 9, pp. 339-364, 1972.

21. Shiff, L. B., and Steger, J. L., _Numerical Simulation of Steady Supersonic Viscous Flow_, AIAA Paper 79-0130, January 1979.

22. Vigneron, Y. C., Rakich, J. V., and Tannehill, J. C., _Calculation of Supersonic Viscous Flow Over Delta Wings with Sharp Subsonic Leading Edges_, AIAA Paper 78-1137, July 1978.

23. Anderson, D. A., Tannehill, J. C., and Pletcher, R. H., _Computational Fluid Mechanics and Heat Transfer_, McGraw-Hill Book Company, 1984.

APPENDIX

BOUNDARY LAYER PROCEDURE

This Appendix presents the governing equations used in the numerical boundary layer code. This code solves the compressible boundary layer equations for either laminar, transitional, or turbulent conditions. The system of equations can be found in numerous references; however, for completeness, the equation set is given. The algebraic turbulence closure, coordinate transformation, and finite difference method are also briefly presented and discussed.

The mean turbulent boundary layer equations can be written as follows:

$$\frac{\partial}{\partial s}(r^j \rho u) + \frac{\partial}{\partial y}(r^j \rho v^*) = u \tag{A-1}$$

$$\rho u \frac{\partial u}{\partial s} + \rho v^* \frac{\partial u}{\partial y} = -\frac{dP}{ds} + \frac{1}{rj}\frac{\partial}{\partial y}(r^j \varepsilon^* \frac{\partial u}{\partial y}) \tag{A-2}$$

$$\rho u \frac{\partial}{\partial s}(C_p T) + \rho v^* \frac{\partial}{\partial y}(C_p \bar{T}) = u\frac{dp}{ds} + \varepsilon^*(\frac{\partial u}{\partial y})^2 + \frac{1}{rj}\frac{\partial}{\partial y}[r^j \varepsilon^* \frac{\partial}{\partial y}(C_p T)] \tag{A-3}$$

The coordinates s, y, and r are illustrated in Fig. A-1. As in conventional notation, here j=1 for axisymmetric flows and j=0 for two-dimensional flows. In addition, the following quantities have been defined.

$$v^* = v + \frac{\overline{\rho' v'}}{\rho}$$

$$\varepsilon^* = -\rho^* \frac{\overline{u'v'}}{\partial u/\partial y}$$

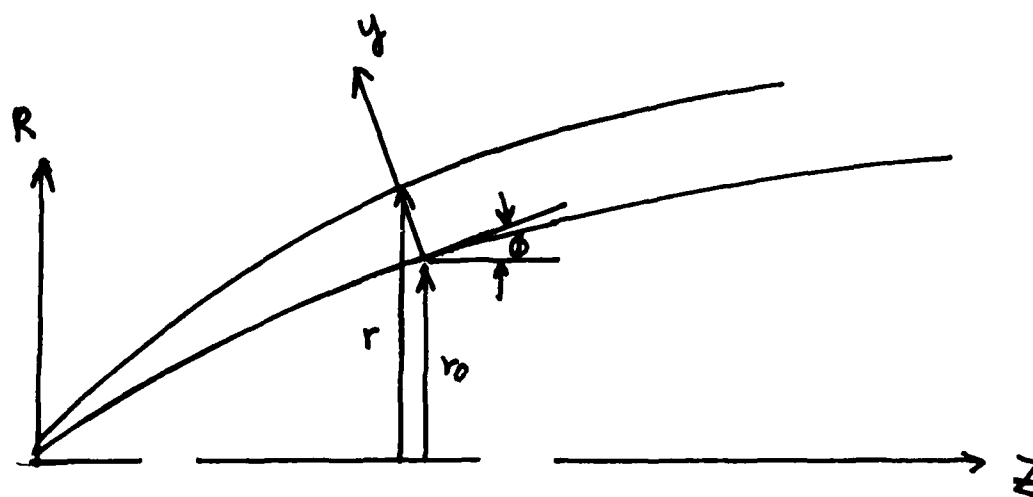$$K_T^* = -C_p \rho \frac{\overline{v'T'}}{\partial T/\partial y} \tag{A-4}$$

Fig. A-1 Coordinate system and notation

The system of equations is closed by the addition of the perfect gas law, a viscosity-temperature relation, and an appropriate turbulence model. The former two relations are,

$$p = \rho RT \quad \text{(perfect gas law)} \tag{A-5}$$

$$\mu = \frac{a_1 T^{3/2}}{1 + a_2} \quad \text{(Sutherland Law)} \tag{A-6}$$

The specific turbulence model used for the present calculations was a two-layer eddy viscosity model that provides both the effective viscosity and effective thermal diffusivity. The equations describing the two-layer model are as follows:

$$\left(\frac{\varepsilon}{\mu}\right)_i = \frac{\rho}{\mu} (K_1 y D)^2 \left(\frac{\partial u}{\partial y}\right) \tag{A-7}$$

$$\left(\frac{\varepsilon}{\mu}\right)_o = \frac{\rho}{\mu} K_2 u_e S_{inc} \bar{\gamma} \tag{A-8}$$

where,

$$D = 1 - \exp(-y/A) \tag{A-9}$$

$$\delta_{inc} = \int_0^\infty \left(1 - \frac{u}{u_e}\right) dy \tag{A-10}$$

$$\bar{\gamma} = \frac{1}{2} \left\{1 - \mathrm{erf}\left[K_3 \left(\frac{y}{\delta} - K_4\right)\right]\right\} \tag{A-11}$$

The empirical constants k_1 to k_4 are assigned values of 0.4, 0.0168, 5.0, and 0.78, respectively. The matching location, y_m^*, for the two layers is determined by requiring the eddy viscosity to be continuous. Thus, y_m^* occurs where,

$$\left(\frac{\varepsilon}{\mu}\right)_i = \left(\frac{\varepsilon}{\mu}\right) \tag{A-12}$$

The eddy conductivity is modeled by a constant turbulent Prandtl number, $PR_t = 0.95$.

The system of equations is singular at $S=0$. The Levy-Lees transformation is used to remove this singularity as well as to reduce the growth of the boundary layer as the solution proceeds downstream. This transformation can be written as,

$$\xi(s) = \int_o^s \rho_e u_e \mu_e \gamma_o^{2j} ds \tag{A-13}$$

$$\eta(s,y) = \frac{\rho_u u_e \gamma_o^j}{\sqrt{2\xi}} \int_o^y t^j (\frac{\rho}{\rho_e}) \, dy \tag{A-14}$$

where t is the transverse-curvature term defined as,

$$t = \frac{\gamma}{\gamma_o} \tag{A-15}$$

The parameters F, θ, and V are introduced and defined as,

$$F = \frac{u}{u_e} \tag{A-16}$$

$$\theta = \frac{T}{T_e} \tag{A-17}$$

$$V = \frac{2\xi}{\rho_e u_e \mu_e \gamma_o^{2j}} \left[F(\frac{\partial \eta}{\partial s} + \frac{\rho v^* \gamma_o^j t^j}{\sqrt{2\xi}} \right] \tag{A-18}$$

The governing equations in the transformed plane then become,

$$\frac{\partial V}{\partial \eta} + 2\xi \frac{\partial F}{\partial \xi} + F = 0 \tag{A-19}$$

$$2\xi F \frac{\partial F}{\partial \xi} + V \frac{\partial F}{\partial \eta} - \frac{\partial}{\partial \eta} (t^{2j} Z \bar{\epsilon} \frac{\partial F}{\partial \eta}) + \beta(F^2 - \theta) = 0 \tag{A-20}$$

$$2\xi F \frac{\partial \theta}{\partial \xi} + V \frac{\partial \theta}{\partial \eta} - \frac{\partial}{\partial \eta} (t^{2j} Z \epsilon \frac{\partial \theta}{\partial \eta}) - \alpha Z t^{2j} \bar{\epsilon} (\frac{\partial F}{\partial \eta})^2 = 0 \tag{A-21}$$

where,

$$Z = \frac{\rho\mu}{(\rho\mu)_e} \qquad (A-22)$$

$$\alpha = (\gamma-1) \, M_e^2 \qquad (A-23)$$

$$\beta = \frac{2\xi}{u_e} \left(\frac{du_e}{d\xi}\right) \qquad (A-24)$$

The wall boundary conditions in the transformed plane are:

$$F(\xi,0) = 0$$

$$V(\xi,0) = V_\omega(\xi)$$

$$\theta(\xi,0) = \theta_\omega(\xi), \text{ or } \left(\frac{\partial\theta}{\partial\xi}\right)_{\xi,0} = \left(\frac{\partial\theta}{\partial\eta}\right)_\omega \qquad (A-25)$$

while at the outer edge we have:

$$F(\xi, \eta_e) = 1$$

$$\theta(\xi, \eta_e) = 1 \qquad (A-26)$$

The pressure gradient is obtained from the MOC procedure.

The system of governing equations is parabolic and can be numerically integrated by marching in the streamwise direction. This marchine procedure is implemented by means of a three-point implicit scheme. A Newton-Raphson type of linearization is used to ensure quadratic convergence in each marching step.

END

DATE

FILMED

9-88

DTIC